NBSIR 80-2169

Molecular Chemistry of Inhibited Combustion Systems

J. W. Hastie and D. W. Bonnell

High Temperatures Processes Group
Chemical Stability and Corrosion Division
Center for Materials Science
National Bureau of Standards
U.S. Department of Commerce
Washington, DC 20234

October 1980

Final Report

Issued December 1980

Prepared for

U.S. Army Research Office
Research Triangle Park, NC 27709

Under Contract IL 161102 BH 57-08

NBSIR 80-2169

MOLECULAR CHEMISTRY OF INHIBITED COMBUSTION SYSTEMS

J. W. Hastie and D. W. Bonnell

High Temperatures Processes Group
Chemical Stability and Corrosion Division
Center for Materials Science
National Bureau of Standards
U.S. Department of Commerce
Washington, DC 20234

October 1980

Final Report

Issued December 1980

Prepared for
U.S. Army Research Office
Research Triangle Park, NC 27709

Under Contract IL 161102 BH 57-08

U.S. DEPARTMENT OF COMMERCE, Philip M. Klutznick, *Secretary*
Jordan J. Baruch, *Assistant Secretary for Productivity, Technology, and Innovation*
NATIONAL BUREAU OF STANDARDS, Ernest Ambler, *Director*

TABLE OF CONTENTS

1. Introduction

1.1 Background and Objective

Empirically, it is well-known that chemical additives can be used to control ignition and flame spread phenomena for a wide variety of combustion systems (Hastie, 1975; Gann, 1975). Common examples include: use of antimony-halogen and organo phosphorus formulations to render fabrics less flammable, use of alkali metal containing powders as fire extinguishants and, similarly, the application of halocarbons to suppress accidental fuel fires (Hastie, 1975; Dehn, 1975; Finnerty, 1975). The safety and economic benefits to be gained from the use of such flame inhibitors often tends to be offset by competing side effects such as, the production of toxic or corrosive combustion products, and the undesirable modification of fabric or fuel properties. In order to optimize inhibitor performance and minimize such undesirable side effects, an improved fundamental understanding of the underlying flame inhibition mechanisms is necessary.

The state of knowledge regarding flame inhibition or fire suppression mechanisms has been summarized in symposia proceedings (Gann, 1975) and reviews (Hastie, 1975, p. 332). From these sources, and the more recent specialized literature cited throughout this report, we can summarize the consensus opinion as follows.

- For most systems considered, the key action of flame inhibitors is chemical kinetic, though physical effects are also present.
- The rate controlling processes most likely involve cyclic reactions between hydrogen halide or metal oxide and hydroxide intermediates and the flame propagating radicals H and OH.
- An unambiguous demonstration of the identity of the key chemical steps, and the reactions rates involved, has not yet been made.

The present study particularly addresses this last viewpoint through a detailed molecular level determination of flame inhibition mechanisms for halogenated and phosphated flame inhibitors.

1.2 Approach

At the present time, completely ab initio determinations of inhibition mechanisms can only be made for very simple premixed flame systems, e.g., see Galant and Appleton (1975); Creighton and Lund (1979); and Dixon Lewis (1979). These examples include flames fueled by H_2 or, with greater kinetic uncertainty, CH_4 with O_2 as oxidant and N_2 as a relatively inert coolant. The only inhibitor species where the elementary rate processes and coefficients are reasonably well understood is HBr. Even in this case, there are serious uncertainties in the rate constants, particularly for OH or O-atom reactions and for chaperone efficiencies in recombination processes. Diffusion flames are even less amenable to either a rigorous experimental or theoretical analysis. However, chemically-based inhibition mechanisms, obtained under both fuel-rich and fuel-lean premixed flame conditions, should be applicable to a diffusion flame system, provided additional gas dynamic factors are included in the latter case.

A primary objective of the present study was to experimentally determine temperature and species concentration profiles for both the stable and radical intermediate species in inhibited premixed flames. In order to carry out this objective, new or improved measurement techniques were developed for monitoring intermediate species and temperature profiles in stationary flames. If all the pertinent species are monitored, such measurements serve to define, and, in principal, in an unambiguous manner, the elementary reactions and rates present, e.g., see Peeters and Mahnen (1973) and Biordi et al. (1978).

Chemical components were selected to be representative of the chemical conditions present in proven fuel-fire inhibition systems. For this phase of the study, the commercial extinguishant CF_3Br and its principal flame decomposition product, HBr, were used as inhibitor additives. Atmospheric premixed flames of H_2-O_2-N_2 and CH_4-O_2-N_2 were selected as flame hosts for these inhibitors. These mixtures should adequately simulate the gas phase chemical kinetic processes occurring in "real-fire" fuel-halocarbon systems, for instance, since the elemental makeup, temperature and pressure is similar in each case. The limited availability of reaction rate data for more complex hydrocarbons dictates the present need for chemical simplicity in the selection of experimental flame systems.

Field tests have demonstrated the feasibility of preventing fuel fires by incorporating halocarbons (e.g., CH_2ClBr) into the fuel (Dehn, 1976). However, the high corrosivity of halogen acid combustion products, together with the high cost of halocarbons, warrant consideration of alternative inhibitor fuel additives. From previous studies on relative inhibitor effectiveness, we can expect additives containing phosphorus or metals such as Fe, Cr, Mo and Sb to be one to two orders of magnitude more effective than halocarbons on a molar additive basis. Experimental evidence for this claim has previously been summarized by Hastie (1975, p. 347). This early evidence for metal based flame inhibition has been further verified and extended by the recent study of Vanpee and Shirodhar (1978). The potential effectiveness of such halocarbon substitutes assumes, however, that they are sufficiently volatile in practical fuel-additive mixtures to enter the vapor phase during an accidental ignition or flame spread process. The most reasonable form for the phosphorus or metal-containing additive is likely to be an organocompound, of the type represented by the phosphine oxides, phosphates and metal acetylacetonates.

In fact, many patents are in existence for the application of such additives in reducing polymer flammability. In view of the potential benefits to be gained from a reduced inhibitor fuel-loading-level, by factors of about 10 to 100, a flame inhibition feasibility study was made on representative organophosphorus compounds.

2. Experimental Methods

2.1 Temperature Measurement

Temperature and species concentration profiles are interrelated parameters in flame systems. In the presence of flame inhibitors, the modified concentration profiles of flame propagating radicals (H, OH, O) can also be reflected in the temperature profiles due to changing heat fluxes and rates for exothermic processes. Aside from the intrinsic significance of temperature in inhibited flames, it is also a necessary parameter in the optical spectroscopic determination of species concentrations where thermal partition functions are used (see Appendix A). Determination of reliable temperature profiles is, therefore, an essential prerequisite to the measurement of molecular species concentrations in normal and inhibited flames. A detailed account of the methods adopted for this purpose is contained in Appendices A and B of this report. Also included are representative temperature profile data and an assessment of the reliability of the various methods used.

2.2 Species Concentration Profiles

The problems associated with measurement of radical species and flame inhibitor intermediates have been discussed elsewhere (Hastie, 1975, p. 254). At the present time no single quantitative experimental approach is suitable for all species present. We have used a combined approach based on optical spectroscopic and mass spectrometric methods. The latter method utilized a High Pressure Sampling Mass Spectrometer (HPMS) system described previously

(Hastie, 1973). A second more versatile mass spectrometric apparatus was also developed for this project. Appendix C contains a description of this new system. Owing to construction delays, this apparatus was completed too late for application to flame sampling measurements. In principle, the mass spectrometric technique can detect all the significant species in inhibited flames. However, in practice it is not always possible to monitor radical species due to mass spectral interferences of fragment ions (Hastie, 1975-76). Also, some of the weaker flames may be perturbed by the insertion of a relatively cool mass spectral flame sampling probe. The use of independent optical spectroscopic methods, therefore, serves both to supplement and validate data obtained by the probe-sampling mass spectrometric approach.

Several relatively well established optical spectroscopic methods exist for measurement of OH and H radical concentrations in flames, although in the former case only optically thin low pressure or weakly absorbing flame systems have been studied previously (Kaskan, 1958). The method used for the optically thick condition of high temperature atmospheric flames is described in detail in Appendix A. Determination of H-atom concentrations was made using the established Li/Na method (see Hastie, 1975, p. 263 for summary and primary literature citations). Basically this method utilizes the spectroscopic resonance emission line intensities of Na and Li for monitoring the balanced (partial thermodynamic equilibrium) reaction:

$$Li + H_2O = LiOH + H \ .$$

The H-atom concentration is then calculated from the known reaction equilibrium constant and H_2O concentration. Of particular significance to the present study is the assumption that Na and Li are present as free atoms, with the exception of LiOH formation and, in some instances, NaOH formation. Further discussion of the validity of this assumption will be given in Section 3.3.

3. Results and Discussion

3.1 Clean Flames

The H_2-O_2-N_2 flames selected as reference systems for evaluating flame inhibitors and determining reaction mechanisms are relatively well understood (Hastie, 1975, p. 259). However, the exact properties of these flames depend on the burner type and construction. As discussed in Appendix A, our burners were intentionally of similar design to those used by earlier workers. Our flame temperatures, obtained by Na D-line reversal with Padley-Sugden type burners were also in agreement with those established earlier, as discussed in Appendix A.

Another useful aspect to these flames is the rapid attainment of partial thermodynamic equilibrium between the radical species H, OH, and O and, in many cases, of general thermodynamic equilibrium in the post flame region corresponding to a few millisecond delay time relative to the primary reaction zone (see Hastie, 1975, p. 268). These intrinsic properties allow us to use multicomponent thermodynamic equilibrium calculations (see Appendix E) to establish post flame radical absolute concentrations, reaction zone relative concentrations, and adiabatic flame temperatures. The typical results of figures 1 and 2 were obtained by such a method using the JANAF Tables as a thermodynamic data base (JANAF, 1971).

From burning velocity determinations made by us and others (summarized by Hastie, 1975, p. 337), we know that the effectiveness of P- and Br-containing additives is much more pronounced in fuel rich flames, and in relatively cool flames. From figure 1, the species H and, to a lesser extent, OH predominate over O under these flame conditions[1]. Figure 2 shows the effect of temperature

[1]From the known balanced condition in these flames, these relative species concentrations are valid even in the kinetically controlled flame regions.

on the equilibrium H concentration and a similar trend occurs for OH and O. These calculations also indicate that for H_2/O_2 ratios in the range 2 to 4 and temperatures in the range 1900 to 2300 K, H-atom concentrations will be in excess of 10^{-4} mole fraction, even under equilibrium conditions. This is a convenient concentration range for the methods available and most of the inhibition studies were made on flames within this range of composition and temperature.

3.2 Bromine Containing Flames

3.2.1 Background

During this phase of the experimental work it became clear, from engine tests carried out elsewhere, that halocarbon fuel additives were much too corrosive to warrant detailed basic studies (Weatherford and Wright, 1976). However, the representative data presented here do provide additional insight into the mechanistic action of halogenated flame inhibitors. Of particular significance is the molecular level confirmation of the very recent theoretically based (Lovachev and Lovachev, 1979) concept of halogen induced flame promotion. A similar halon-induced promotion effect has also been found in the auto-ignition of propane (Finnerty, 1975).

Present understanding of halogenated flame inhibition is based either on empirical macroscopic observations, such as changes in burning velocity or oxygen indices in atmospheric pressure flames, or on molecular level observations of radical species in low pressure flames. Numerous reviews and assessments of possible mechanisms have been made based on such data, e.g., see as representative citations Lovachev and Lovachev, 1979; Fistrom and Van Tiggelen (1978); Hastie (1975, p. 337) and Gann (1975).

The most widely considered reaction, key to the inhibition mechanism, is:

$$H \text{ (or OH)} + HBr = H_2 \text{ (or } H_2O) + Br \ ,$$

where the parenthetical process is competitive only in fuel-lean flame mixtures. Recent spectroscopic results further support HBr as the key intermediate species in Br-containing inhibitors (Petrella, 1979). Regeneration of HBr in the cyclic process is thought to result from reactions such as:

$$H + Br + M = HBr + M \quad ,$$

$$HO_2 + Br = HBr + O_2 \quad .$$

These two reactions reveal several limitations in the experimental methodology previously used to delineate inhibition mechanisms. The first regenerative process is necessarily pressure dependent and low pressure studies may not necessarily reflect the correct behavior under atmospheric conditions. Empirically, halogens are known to be more effective inhibitors at higher pressures. The extent to which the second process will regenerate HBr will be highly temperature dependent owing to the low stability of HO_2 in hotter flames (Hastie, 1974). These considerations alone suggest that the function of flame inhibitors may vary widely with flame type. In fact, during the course of this work it became experimentally evident that inhibitors could also function as promotors for certain flame conditions. Very recent theoretical considerations (Lovachev and Lovachev, 1978, 1979) suggest that this may occur through a reversal of the normally inhibitive process:

$$H + HBr \leftarrow H_2 + Br \quad ,$$

where Br is regenerated by the reaction:

$$HBr + HO_2 \rightarrow H_2O_2 + Br \quad .$$

The $HBr\text{-}H_2\text{-}O_2\text{-}N_2$ flame system is sufficiently well understood in terms of the elementary reactions and their rates that relatively reliable kinetic modeling is now possible. Hence, the few experimental observations of Br-catalyzed flame promotion and the many and sometimes disparate inhibition studies can now be rationalized. Through such a modeling approach, Lovachev

and Lovachev (1979) have recently demonstrated the extreme sensitivity of inhibition/promotion switching to the flame variables of composition, pressure and temperature. Their calculations also show the expected promotion effect at relatively high temperatures, in agreement with our experimental observations (presented in Section 3.2.2).

In the present study, direct observations of the various reaction intermediates were made in atmospheric flames to test these various hypotheses.

Another difficulty with current treatments of flame inhibition is the lack of information concerning temperature distribution in the presence of inhibitors. In fact, some treatments assume temperature changes to be unimportant, e.g., see Fristrom and Van Tiggelen (1978). However, studies with quenched flames, e.g., see Reuther (1979), suggest temperature to be an important variable in flame inhibition. Accordingly, in the present study, considerable effort was given to obtaining precise temperatures in clean and inhibited flames, as described in Appendices A and B, respectively.

3.2.2 Mass Spectrometric Observations

Previous work in this and other laboratories has shown the H-atom peak concentration to correlate very well with burning velocity for various flame stoichiometries without inhibiting additives present (see Hastie and McBee, 1975, and loc. cit.). Observation of H-atom concentration profiles in clean and inhibited/promoted flames should, therefore, provide an unambiguous test of various suggested inhibition/promotion schemes. Lack of sensitivity and, more particularly, mass spectral interferences due to the electron impact fragmentation processes:

$$e + H_2 \rightarrow H^+ + H + 2e$$

$$e + H_2O \rightarrow H^+ + OH + 2e \quad ,$$

prevented measurement of reliable H-atom concentration profiles in relatively cool fuel rich flames where inhibition is greatest. However, in hotter flames where the H-atom concentration is greater relative to H_2 and H_2O reliable data could be obtained.

Figure 3 shows the effect of added CF_3Br to the H-atom concentration profile, expressed as mass spectral ion intensities, in a near-stoichiometric premixed laminar $H_2/O_2/N_2$ flame. Available optical and thermocouple methods could not be applied to temperature measurements in this flame. The maximum flame temperature was, therefore, estimated as 2750 ± 100 K using the calculated adiabatic value and the expected burner heat loss, based on laser Raman temperature measurements made on cooler flames with a similar burner. Note, in figure 3, the early depletion of both CF_3Br and the HBr intermediate upstream from the reaction zone (∿ 0.3 cm distance). Qualitatively, these profiles support the reaction:

$$H_2 + Br \rightarrow HBr + H \quad ,$$

as a dominant flame promoting reaction. Temperature profiles are needed to utilize these concentration profile data for derivation of quantitative kinetic schemes.

3.2.3 Laser Raman Spectroscopic Observations

The effect of a halogenated inhibitor, HBr in this case, on the temperature profile was monitored using recently developed laser Raman spectroscopic methods described in Appendix B. As shown in figure 6 of Appendix B, under inhibition conditions, i.e., observed reduction in burning velocity, addition of a thermodynamically insignificant amount of HBr (0.005 mole fraction) has a marked effect on the temperature profile. In the preflame (3 to 5 mm distance) and reaction zone (5 to 7 mm distance) regions, HBr reduces the temperature and by as much as 900 K at a fixed location relative to the burner.

On the other hand, in the burnt gas region (> 7 mm distance) a small temperature increase occurs. These effects are consistent with removal of H-atoms in the preflame and reaction zone regions, resulting in a delay of the chain branching process:

$$H + O_2 = OH + O \quad ,$$

which, in turn, reduces the conversion of fuel H_2 to H_2O through radical controlled processes, such as:

$$OH + H_2 = H_2O + H \quad .$$

However, once the combustion process is complete, the continuing catalytic removal of H-atoms in the burnt gas region provides additional heat through the overall exothermic process:

$$H + H \rightarrow H_2 \quad .$$

A similar effect is found when the inhibitor SO_2 is present in low pressure fuel-rich $H_2/O_2/Ar$ flames at relatively low temperature (Fenimore and Jones, 1965). Also, the increased rate of heat release was found to be consistent with the heat generated by a catalysed H-atom recombination process.

An additional factor contributing to the slight temperature increase in the post flame region may be the reduced heat loss to the burner due to the delayed flame reactions; i.e., the reaction zone is further removed from the burner face. As shown in Appendix B (fig. 6), the temperature profiles are also consistent with the established burning velocities.

Attempts to use the laser Raman methods in hotter flames containing halogens, such as that described in Section 3.2.2, were unsuccessful due to background luminosity interference effects.

3.3 Phosphorus Containing Flames

3.3.1 Introduction

During the course of this project, it became evident that the use of halogenated additives for in situ suppression of fuel fires was impractical, owing to the corrosive effect of halogen acids on engines (Weatherford and Wright, 1976). Increased attention was, therefore, given to possible alternative inhibitors containing phosphorus. Potentially volatile phosphorus compounds are known inhibitors in commerical formulations for plastics (e.g., see Brauman, 1977), aircraft drops for forest fires, and in premixed flames (e.g., see Hastie and McBee, 1975) Also, the limited burning velocity evidence available suggests that phosphorus compounds may be an order of magnitude more effective than halogens as inhibitors.

In the present study, a combined visual (burning velocity changes), optical spectroscopic, high pressure sampling mass spectrometric, and modeling approach was used to elucidate the mechanistic action of volatile P-compounds as inhibitors. These systematic studies revealed inhibition/promotion effects analogous to those found for Br-containing additives.

3.3.2 Qualitative Visual Observations

While the main emphasis of the present study was to determine the microscopic or molecular level details of flame inhibition, the mechanistic understanding gained must be consistent with macroscopic phenomena such as burning velocity changes. It is also important to establish a correlation between flame inhibition and extinction and for a variety of flame types, e.g., premixed, diffusion, hydrocarbon and non-hydrocarbon fuels.

A laboratory torch was used and visual flame changes recorded photographically. Hydrogen, methane, propane and benzene were used as fuels and air as oxidant. Following representative experiments with each fuel-type, systematic

observations were made with methane and propane fuels. The air was either premixed with the fuel or allowed to enter the flame by diffusion from the atmosphere. Compositions from stoichiometric to fuel-rich were used with both smoking and non-smoking flames produced. Trimethylphosphate, phosphoryl-chloride, and triphenylphosphine oxide vapors were premixed with the fuel to provide phosphorus inhibitor to the flames. Burner total gas flow rates and inlet temperatures were kept essentially constant with and without inhibitor present. Similar results were obtained with each additive, indicating the common P-component to be the main active agent. Earlier work extablished the negligible effect of the hydrocarbon component of the P-additives of flame inhibition (Hastie and McBee, 1975).

For the constant gas flow conditions used, the premixed flame burning velocity is inversely proportional to the area bounded by the luminous reaction zone. Thus, relatively strong flames burn close to the burner face and vice versa for weak flames.

Typical results are shown in figures 4(a)-(n). In figure 4(a), for example, the area under the luminous cone can be used as a measure of the burning velocity for the non-inhibited premixed propane-air flame. In fact, these visual effects are consistent with the known inhibition index[2] ($\phi_v \sim 23$) for TMP in premixed hydrocarbon flames, e.g., see data cited by Hastie (1975, p. 337). As an example, from the flame areas of figures 4(i) and 4(j), we calculate $\phi_v \sim 40 \pm 10$ for the inhibited methane-air flame. For these particular diffusion flames we also considered area changes as an indication of flame inhibition (i.e., enlarged area) or promotion (i.e., reduced area).

[2]Inhibition index is $\phi_v = ([O_2]/[I])(\delta v/v_o)$, as defined by Fristrom and Sawyer (1971); δv is the change in burning velocity due to the presence of inhibitor, v_o is the burning velocity of the clean flame, I is the inhibitor concentration, and $[O_2]$ is the O_2 concentration in the unburnt gas.

Note, in figure 4(a), the onset of smoke formation as evidenced by the highly luminous flame tip. As $POCl_3$ was added to the fuel, both the luminous reaction zone and the area of smoke production enlarged. An enhanced area of flame incandescence was taken to be a measure of smoke production. The luminosity provided by P itself, in the form of PO and HPO emission, was shown, from observations in H_2-O_2-N_2 flames, to be negligible compared to smoke incandescence. Figure 4(b) shows the result of addition of four percent $POCl_3$ immediately prior to flame blow-off and extinction. Evidence of this imminent condition may be noted by the absence of flame near the burner face [see fig. 4(b)]. When the fuel-air mixing was maintained through diffusion of ambient air to the flame, the effects of P-additives were virtually reversed from the premixed case, as shown in figures 4(c)-(d). Here a stronger, reduced smoke content, flame resulted from the introduction of four percent $POCl_3$.

Analogous behavior was noted for propane and methane flames containing 10^{-3} mole fraction trimethylphosphate (TMP), e.g., see figures 4(e)-(n). Qualitatively, TMP was more effective than $POCl_3$ and methane flames were more sensitive than propane to additive effects.

The main results of these observations are summarized in table 1. Note the apparently anomalous behavior of the methane diffusion flame containing TMP [see also fig. 4(n)], where smoke enhancement, and possibly some flame inhibition, occurs. The main phenomenological results are summarized as follows:

- Flame inhibition and smoke formation are apparently interrelated processes (see Hastie, 1975, p. 357, for discussion of the nature of this relationship).
- P-based flame inhibition does correlate with extinction.

- Under certain conditions of fuel-air composition and mixing, P-additives can increase the flame strength.

We should also emphasize that addition of a few percent, or less, of these additives has an insignificant effect on the fuel value or combustion thermodynamics and their effect can only be interpreted in terms of catalytic phenomena. The molecular level observations summarized in the following sections will provide a kinetic scheme consistent with these macroscopic phenomena.

Table 1

Visual Effects of Phosphorus Additives on Flame and Smoke Propagation

Fuel	Inhibitor	Premixed	Diffusion
Propane	$POCl_3$	FI, SE(a,b)	FE, SR(c,d)
Propane	TMP	FI, SE(e,f)	FE, SR(g,h)
Methane	TMP	FI, SE(i,j)	SE(m,n)

FI-flame inhibition, FE-flame enhancement, SE-smoke enhancement, SR-smoke reduction, (a) indicates source Figure 4(a), etc.

3.3.3 High Pressure Sampling Mass Spectrometric (HPMS) Observations

Previously we reported for P-containing flames the formation of PO and a non-resolved group of species at 63 ± 1 amu, which probably included one or more of the species HPO_2, PO_2, and P_2 (Hastie and McBee, 1975). The present HPMS experiments resolved the 63 ± 1 amu group, indicating HPO_2 as the predominant component, as shown in figure 5. Typical post-flame data are given in table 2, where the significant formation of PN is also indicated. The HPO_2/PO relative partial pressure data have been plotted as a function of temperature in figure 6. For a wide range of flame stoichiometry and location, the novel

Table 2

Flame Concentrations of Phosphorus Containing Species

	Flame Conditions				
$H_2/O_2/N_2$	3.1/1/4[a]	9.7/1/3.3	6.5/1/4.2	11.4/1/4	3.1/1/2.7
TMP (10^{-3} atm)	3.0	2.0	3.0	3.0	3.0
Temp. (K)[b]	2100	1460	1600	1350	2340
Time (10^{-3})[c]	2.0	3.0	1.3	∿2.0	∿2.0
P-Species	Partial Pressure X 10^4 atm[d]				
PO	20.0 (20.0)[e]	12.0 (0.7)	24.0	27.6	28.5
HPO_2	0.4 (1.3)	3.1 (0.4)	2.4	2.4	1.5
PN	1.5 (5.6)	1.6 (19.0)	2.4	---	---
P_2	<0.05(0.005)	1.2 (0.4)	<0.2	---	---
PO_2	<0.05(2.1)	<0.4 (0.006)	<0.4	---	---
HPO	<0.05(0.02)	<0.6 (0.002)	<0.2	---	---

[a] NTP mole ratios of burner input gas.

[b] Uncertainty ± 100 K. Determined either from Na D-line reversal or from adiabatic thermodynamic calculation with empirical burner heat-loss correction.

[c] Flow-time, at measurement location relative to reaction zone as origin. Typically, 2 ms ∿ 1 cm distance from reaction zone.

[d] Relative uncertainties ± 10 percent, absolute ± 30 percent. Upper limit values set by mass spectrometer detection limit which can vary at different amu due to fragment ion interference, background noise and mass discrimination effects. Tests showed that a satisfactory mass balance could be achieved between P-added and P-produced using estimated ionization cross sections. Therefore, these data have been normalized by assuming mass balance is present.

[e] Values in parentheses indicate predicted equilibrium partial pressures.

species HPO_2 was always much more abundant than PO_2 or P_2, indicating high stability and HO-P=O bonding rather than H-PO_2[3]. We have determined thermodynamic functions for this species, as summarized in Appendices D and E. The thermodynamic prediction of HPO_2/PO partial pressure dependence on temperature is indicated by curve A of figure 6. Note that the high temperature flame data closely approach this curve, indicating a state of partial thermodynamic equilibrium.

The formation of HPO_2 as a stable reaction intermediate has previously been suggested by Davies and Thrush (1968) based on low pressure flow discharge studies in the O+PH_3 system. To account for a continuous emission in the ultraviolet, they postulated the exothermic process,

$$OH + PO \rightarrow HOPO \text{ (i.e., } HPO_2) \quad .$$

Further evidence for the stability of phosphorus acid species is provided by the observation of numerous $H_xP_yO_z$ ionic species (x=1-3, y=1-4, z=1-11) in the mass spectrum of vapors over damp P_4O_{10} at 400 °C (Muenow et al., 1970).

The mass spectrometric data for the major flame species, N_2, H_2, O_2, and H_2O were found to obey mass balance to better than 90 percent of the theoretical result. For the phosphorus species, where the concentrations are much lower, the mass balance was more uncertain. Typically, the observed total concentration of P-products (primarily, PO, PN, HPO_2) was 50±30 percent of the initial concentration of TMP, as determined by a transpiration calibration experiment. This mass balance discrepancy may be due to the presence of an undetected P-containing species in the flame. However, it is unlikely that such a species would escape mass spectral detection. Considering the difficulty associated

[3]This argument is based on the known P-H bond energy in species such as PH_3.

with quantitative measurement of minor flame species, and particularly those where ionization cross sections are estimated, we are satisfied with the degreee of mass balance achieved.

3.3.4 Optical Spectroscopic Observations

As we have discussed in detail elsewhere (Hastie, 1975, p. 338), the key to understanding catalytic flame inhibition processes centers around reactions involving H-atoms and, perhaps, to a lesser extent, OH radicals, For fuel rich flames, there is a well established correlation between burning velocity and H-atom concentration, at least in the region of the reaction zone (Padley and Sugden, 1959; Hastie and McBee, 1975). These empirical observations are also supported by various theoretical models. For instance, in the Fristom and Sawyer (1971) approach, burning velocity is proportional to the one half power of the H-atom concentration. Thus, from the burning velocity observations of Miller, et al. (1963) for flame inhibition by PCl_3, the corresponding H-atom loss would be 95 percent. That is, in the presence of 2 percent PCl_3, the H-atom concentration is only 5 percent of that for the uninhibited flame. From the observed burning velocity changes in the present study, we can expect H-atom reductions typically in the range of 40 to 80 percent.

While it is possible to monitor H and OH using the HPMS technique (Hastie, 1973), optical spectroscopic techniques are more convenient and accurate under fuel rich conditions.

H-atom Concentration Profiles: Typical hydrogen atom concentration profiles, obtained using the Li-Na technique, are given in figures 7 through 11. Also given are the calculated equilibrium H-atom concentrations, [H], for the experimental flame temperatures. Note that for the hotter flames depicted in figures 8 through 11, [H]-observed is in close agreement with the calculated equilibrium values in the burnt gas region. This agreement can be expected from the known

H-atom recombination rates for these flames and supports the experimental procedures used for H-atom concentration and temperature determinations.

Note in the relatively cool flame (fig. 7), the dramatic reduction in [H] with a small amount (0.47 percent) of phosphorus present. In contrast, addition of a similar amount of phosphorus to the hottest flame (fig. 11) caused an increase in the H-atom concentration level. As H-atom concentrations (near the reaction zone) correlate with burning velocity, these results are indicative of P-induced flame inhibition and promotion for the relatively cool and hot flames, respectively. The significant H-atom reduction in the P-containing lean flame represented in figure 9 is particularly noteworthy. Apparently, phosphorus additives can be effective inhibitors under fuel-lean and fuel-rich conditions, both of which occur in diffusion flames and most non-laboratory combustion systems. Halocarbons, by contrast, appear to be more effective in rich than lean flames.

Using the [H]-burning velocity correlation, the reduction in [H] shown in figure 7, for example, can be used to establish the inhibitor index, ϕ_v, where $\delta[H]/[H]$ replaces the usual $\delta v/v_o$ term. Thus, for the $H_2/O_2/N_2 = 5/1/4.1$ flame, we calculate $\phi_v = 20$. This compares very well with the value of 23 for TMP in a stoichiometric n-hexane/air flame, as determined visually from burning velocity measurements (Lask and Wagner, 1962). Such agreement tends to validate the theoretical basis for defining ϕ_v, as well as the correlation of H-atom concentration with burning velocity and the H-atom concentration measurement procedure. We are reluctant to ascribe an inhibitor index value to the lean flame data (fig. 9) owing to the uncertainty introduced by the large correction for alkali metal-phosphorus species interaction (see figs. D.2 and D.8 in Appendix D).

Temperature Profiles: For flames where a strong inhibition/promotion effect was found, using H-atom concentration changes as an indicator, pronounced temperature changes were noted. Typical temperature vs distance profiles are given in figure 12. These data were obtained using the Na D-line reversal method, discussed in Appendix A. It is interesting to note the parallel between the effect of TMP and HBr on temperature distribution in inhibited flames. As shown in figure 12, TMP inhibition causes a temperature increase downstream from the reaction zone. A similar behavior was noted in HBr-inhibited flames (see fig. 6, Appendix B), and the interpretation (see Section 3.2.3) is believed to be the same for both cases. The converse behavior is found for promoted flames, where the position of maximum temperature moves closer to the burner in the presence of additive. This behavior is consistent with an increased burning velocity, allowing the reaction zone to stabilize closer to the burner face, together with a higher H-atom concentration level near the burner face.

Thermal Emission Observations: Given the strong temperature dependence of the degree of P-induced inhibition/promotion, as shown in figures 7, 8, and 11, together with the sensitivity of temperature itself to inhibition/promotion, and the concerns expressed in Appendix A concerning Na D-line reversal temperature data, a temperature-validation test was sought. At flame distances corresponding to post reaction zone gas flow times of greater than about a millisecond, it is known from previous studies (e.g., see Kallend, 1967) that the electronic states of metal containing species will be thermalized. Hence, the activation energy corresponding to thermal emission will be equivalent to the energy separation of the upper and lower electronic states involved in the transition. This energy difference, E, will determine the temperature dependence of the emission intensity, I, according to the relationship:

$$I = A \exp(-E/RT) \quad ,$$

where A is constant and R is the universal gas constant. The temperature dependence of I can, therefore, be used to determine E, which is independently known from spectrocopic observation. Thus, if E-observed equals E-spectroscopic, the measured temperature data are spectroscopically self-consistent and can be used with confidence for the thermodynamic and kinetic treatment of flame reactions.

During the course of obtaining H-atom concentration data with the Li/Na method, Na D-line emission intensity data were recorded. These data are plotted as a function of the separately obtained (much higher Na concentrations used) Na D-line reversal temperatures in figure 13. Sodium atom concentrations under the conditions of the Li/Na method are typically in the region of 3×10^{-6} mole fraction.

The green emission of HPO at 612.2 nm[4] is particularly intense in fuel rich flames, and this species can be conveniently used as a temperature probe in P-containing flames. Typical data for HPO emission intensity, as a function of Na D-line temperature, are given in figure 13.

It is apparent in figure 13 that the predicted (solid curves) and experimental (data points) temperature dependence for Na and HPO emission are in agreement, within experimental error. Thus, the Na D-line reversal temperatures are self-consistent in addition to being consistent with the Na and HPO emission data.

Emission Intensity Flame Profiles for OH, PO and HPO: Changes in H-atom concentrations, resulting from inhibition/promotion, should also be reflected in the OH concentration profiles owing to the strong coupling of balanced reactions, such as:

[4]This wavelength lies in the broad continuum region of the well known HPO system. Several discrete bands at 525 and 554 nm were also monitored (see Dagnall et al., 1968).

$$OH + H_2 = H_2O + H$$

$$H + O_2 = OH + O$$

$$O + H_2 = OH + H.$$

Emission intensities of OH can be used both as a measure of chemiluminescent processes (i.e., near the reaction zone) and of the OH concentration, particularly in the post flame region. Typical data are given in figures 14 and 15 for an inhibited and promoted flame, respectively. The strong emissions of PO (e.g., see Fenimore and Jones, 1964) and HPO can, likewise, be used as indicators of flame radical processes. Representative profile data are given in figures 16 and 17. Note for each species (OH, PO, and HPO) the excessive emission at distances of a few millimeters, characteristic of chemiluminescence. At greater distances, the emission profiles are characteristically thermal and represent the ground state species concentrations.

The effect of added P on OH emission, sufficiently removed from the reaction zone region to avoid chemiluminescence, correlated well with the corresponding H-atom concentration changes; e.g., compare figures 14 and 9. Thus, OH depletion and enhancement was observed for inhibited and promoted flames, as shown in figures 14 and 15, respectively. These observations do not necessarily indicate that OH is directly involved with P-species, owing to the presence of balanced reactions involving H and OH. Thus we consider the observed OH profiles to reflect the primary effects of H-atom reactions. We should note that the OH emission intensity-versus-distance profiles do not always quantitatively follow the corresponding H-atom concentration data. This results in part from the presence of OH in the shield flame, and its ambiant air boundary, at a different temperature and concentration to that in the core flame, as discussed in detail elsewhere (Grabner and Hastie, 1980). The H-atom data do not suffer from this effect of non-uniform line of sight

species distribution, owing to the method of introducing Li and Na only to the core flame. However, in some flames the accuracy of [H] is also limited owing to the corrections required as discussed in Appendix D. This problem is particularly evident in the post flame region of the 2/1/2 flame as shown in figure 11.

For PO and HPO, the excessively high emission intensities near the burner face (i.e., reaction zone) are indicative of chemiluminescent reactions, such as:

$$PO + H + H \rightarrow PO^* + H_2$$

$$HPO + H + H \rightarrow HPO^* + H_2 \text{ , and}$$

$$PO + H\ (+X) \rightarrow HPO^*\ (+X) \text{ ,}$$

where X is a third body major flame component. Thus, the emission intensities in this region can be correlated with H-atom concentration levels. Figure 18 shows an example of such a correlation for HPO*, and this relationship is good evidence for the participation of HPO in H-atom abstraction and recombination processes. However, no claim can be made with regard to reaction order from these data.

Inhibition/Promotion Temperature Dependence: Through systematic variation of flame stoichiometry, fuel type (e.g., H_2 or CH_4) and temperature, we established temperature as the main factor determining whether the additive functions as an inhibitor or promotor. Subsequent theoretical analysis of this phenomenon in Section 3.3.6 will support this observation, as well as indicating other contributing factors.

At or near the reaction zone, the percent change in H-atom or OH radical concentration, on P-addition, may be taken as a measure of the degree of flame inhibition/promotion. Figure 19 summarizes these changes as a function of temperature. Factors influencing the experimental scatter include, 20 percent

variations in TMP concentration between flames, temperature uncertainties of ±50 K, and ±10 percent uncertainty in [H] resulting from the correction procedure used to account for alkali metal-phosphorus chemical interaction, as discussed in Appendix D. Also, these data were obtained over a period of several years with various burners (but each of the Padley-Sugden type) and apparatus configurations.

Note the cross-over from inhibition to promotion in the region of 2350±50 K. It is also pertinent (in fig. 19), for later discussion in Section 3.3.6, that changes in OH thermal emission intensities also follow the same empirical curve derived from the H-atom data. Also of note is the consistency of the CH_4 flame (point 11, fig. 19) with the H_2 flame data.

3.3.5 Mechanistic Action of Phosphorus on Flame Inhibition

In earlier studies we suggested the reaction:

$$H + PO + (X) \rightarrow HPO + (X)$$

as the most likely dominant process in P-based flame inhibition (Hastie and McBee, 1975). However, with the identification of HPO_2 as a more significant species than HPO and discovery of the inhibition/promotion phenomenon, this suggestion requires reconsideration.

Thermodynamic Considerations: Flame inhibition effects have sometimes been attributed to thermal (heat extraction by inhibitor) rather than chemical kinetic processes (Larson, 1975). However, using the free energy minimization procedure for multicomponent equilibrium systems (see Appendix E), we can show that thermodynamic interactions between flame and additive are negligible in terms of cooling or radical quenching effects for the concentration levels used.

Figure 20 shows an example of the negligible thermodynamic effect of P-inhibitor additions on flame temperature and H-atom concentration changes. This predicted effect can also be verified by experimental observations made a few centimeter downstream of the reaction zone, where thermodynamic equilibrium conditions exist for the hotter flames. For example, in figures 8 and 9, the downstream H-atom concentration level is virtually unaffected by the presence of TMP inhibitor.

Flame reactions involving inorganic species such as metal oxides and hydroxides are usually balanced (e.g., see Hastie, 1975, p. 270) and it is reasonable to expect this condition to hold for the P-intermediates. Thus the various phosphorus species can be expected to be in a state of partial thermodynamic equilibrium. Bimolecular reactions with relatively low heat-changes in either direction are likely candidates for maintaining a balanced, partial thermodynamic equilibrium condition between the phosphorus intermediate species. Examples include reactions listed in table 3. A balanced condition allows one to utilize thermodynamic calculations to determine relative concentrations and trends for various flame conditions, even if the total system is kinetically controlled. Thus, from figures 21 and 22 we see that for fuel rich conditions, PO and HPO_2 should be the predominant P-containing species, in agreement with the mass spectrometric observations. Likewise, the species POH (or HPO) and P_2 are probably not significant. Similar species distributions are found for CH_4-fueled flames. The high PN concentration formed under fuel-rich conditions is of note (fig. 22) as it reduces the availability of active phosphorus species for flame inhibition or promotion.

It is, perhaps, pertinent to compare and contrast our thermodynamic and experimental results on species identities with those of Fenimore and Jones (1964). Their studies involved, primarily, low pressure, very

Table 3

Candidate Reactions for P-Induced Flame Inhibition by H-Atom Removal[a]

	Reaction	Equilibrium Constant[c] $K = \exp(\Delta S/R)\ \exp(-\Delta H/RT)$		Rate Constant[c,d] $k = A \exp(-E/RT)$	
		$\exp(\Delta S/R)$	$-\Delta H/R$ (K)	A[f]	E/R[e] (K)
1	$PO + H + X$[b] $\rightarrow HPO + X$	6.5 (-7)	18,900	1.1 (-29)	300
2	$HPO + H \rightarrow PO + H_2$	0.86	35,600	1.1 (- 9)	300
3	$HPO_2 + H \rightarrow PO + H_2O$	15.1	21,740	1.5 (-10)	300
4	$HPO_2 + H \rightarrow PO_2 + H_2$	3.3	19,200	2.1 (-10)	300
5	$PO_2 + H \rightarrow PO + OH$	19.5	- 4,930	1.5 (-10)	5230
6	$PO_2 + H + X \rightarrow HPO_2 + X$	0.21	35,300	1.5 (-28)	300
7	$PO + OH + X \rightarrow HPO_2 + X$	8.6 (-9)	40,300	1.5 (-28)	300
8	$HPO_2 + OH \rightarrow PO_2 + H_2O$	0.8	26,700	1.5 (-10)	300
9	$HPO_2 + H_2 \rightarrow HPO + H_2O$	18.1	13,900	1.7 (-10)	300
10	$PO + H_2O \rightarrow PO_2 + H_2$	0.22	- 2,500	1.0 (-11)	2800
11	$H + O_2 \rightarrow OH + O$				
12	$H + H_2O \rightarrow H_2 + OH$				
13	$H + OH + X \rightarrow H_2O + X$	see JANAF (1971)		see Baulch et al. (1972)	
14	$H + H + X \rightarrow H_2 + X$				
15	$O + H_2 \rightarrow OH + H$				

[a] Corresponding reactions for OH removal can be written and these may be significant in stoichiometric and lean flames.

[b] X represents a third body major flame constituent, e.g., H_2O or N_2.

[c] ΔS and ΔH are the reaction entropy and enthalpy terms, respectively. Also, ΔS, ΔH, A, and E are taken to be temperature independent, which is a good approximation over the temperature range of interest (1800 to 2600 K). See table E.4, Appendix E, for species thermodynamic functions used.

[d] Data refer to forward reaction rate constants, k_f. Reverse reaction rate constants k_r are given by, $k_r = k_f/K$. It also follows that $A_f/A_r = \exp(\Delta S/R)$ and $E_f/E_r = \Delta H$.

[e] All exothermic processes have been assigned the value 300 K following the procedure used by Jensen and Jones (1974, 1976) for analogous systems.

[f] Units, molecule^{-1} cm^3 s^{-1}.

fuel-rich, H_2- or CH_4-O_2-Ar flames at relatively low temperatures (1100 to 1400 K). In the presence of TMP, they deduced, indirectly, from spectroscopic observations of HPO, the formation of P_2 as the primary phosphorus intermediate. However, our thermodynamic calculations indicate HPO_2 as the predominant species under their flame conditions.

Kinetic Considerations: By analogy with previous observations on the catalytic activity of species such as NO, SO_2, SbO, SnO, BaO, BaOH, and $Ba(OH)_2$ on H-atom recombination [e.g., see the review of this early work given by Hastie (1975), p. 297], together with the above thermodynamic arguments, and the HPO*, OH*, PO*, and [H]-flame profiles, the most reasonable reactions leading to flame inhibition are reactions 1 through 10, given in table 3. The significant number of reactions involving HPO_2 is of note, as is the analogy with HSO_2 as a catalytic intermediate (e.g., see Kallend, 1972). A more detailed discussion of this reaction scheme will be made in connection with the temperature dependent inhibition/promotion phenomenon (see Section 3.6.6).

The H-atom concentration vs distance/time profiles for inhibited flames can be shown to support this mechanistic scheme for catalysed H-atom recombination, as follows. In the absence of inhibitor, H-atom depletion in the post flame region occurs via the relatively slow termolecular reactions [13] and [14]. The radical species H and OH are coupled by the relatively rapidly balanced reactions [11] and [15]. It follows, ignoring diffusion, that

$$[H]_t^{-1} - [H]_o^{-1} = (k_{13} + k_{14}\alpha)t/(1 + \alpha)$$
$$= k_{clean} \cdot t/(1 + \alpha) ,$$

where

$$\alpha = \frac{[OH]}{[H]} = K_{12}[H_2O]/[H_2] ,$$

and t = 0 at the reaction zone. K_{12} is the known equilibrium constant for reaction [12] and k_{13} and k_{14} are the known rate constants for reactions [13] and [14], respectively. In the presence of P-inhibitor, following the approach of Bulewicz and Padley (1970),

$$[H]_t^{-1} - [H]_o^{-1} = (k_{clean} + k_{cat}[P]) \cdot t/(1 + \alpha).$$

In the post reaction zone region of the experimental $H_2/O_2/N_2$ flames, temperature, and α are effectively constant[5]. Hence, plots of $[H]^{-1}$ vs t (time from reaction zone) should yield linear curves, over the recombination region (i.e., where [H] > equilibrium), and with slopes equivalent to k_{clean} and k_{cat} in the absence or presence of inhibitor, respectively. Also, as was suggested by Bulewicz and Padley (1970), the inhibitor effectiveness, E, can be expressed as,

$$E = k_{cat}/k_{clean} .$$

With this approach, values of E, ranging from 2.8 to 1.0, have been determined for various inhibiting additives, as summarized by Hastie (1975, p. 299). These efficiency values also correlate reasonably well with the inhibition parameter ϕ_v. For the very effective Sn inhibitor where ϕ_v = 31, or 12.9, depending on fuel type, the corresponding E value is 1.6. A typical result for P-inhibition from the present work is E = 2.7. This is quite consistent with the observed ϕ_v values in the range of 30 to 40.

[5]However, there is evidence (Bulewicz and Padley, 1970) that the ratio [OH]/[H] can sometimes increase with distance into the burnt gas region, contrary to an ideal flame condition where this ratio should be invariant. This effect is attributed to the effects of air entrainment and changes in $[H_2O]/[H_2]$ along the flame (Bulewicz and Sugden, 1956). We believe that this effect may also be present in some of our flames (Grabner and Hastie, 1980) and that it could tend to reduce the slope of the $[H]^{-1}$ vs t plots and reduce the apparent effectiveness of the catalytic process.

Figure 25 shows typical $[H]^{-1}$ vs time plots for an inhibited flame where the slope ratios yield E = 2.7. That these curves are linear in the recombination region supports the catalysed recombination mechanism, but does not, however, allow us to distinguish between HPO and HPO_2 as catalytic intermediates.

The net rate constant data derived from the slopes of clean flame curves (e.g., see fig. 25) for the set of flames used in this study agree within factors of two to three with the rate constants given by Jensen and Jones (1974) for reactions [13] and [14] (see table 3). This is very good interlaboratory agreement for flame derived rate coefficients.

3.3.6 Kinetic Model for Inhibition/Promotion Temperature Dependence

From the combined results of the mass and optical spectroscopic studies, together with the thermodynamic modeling predictions for balanced reaction systems and the mechanistic evidence for inhibition (Section 3.3.5), we have the following mechanistic clues concerning the inhibition/promotion reversal phenomenon:

a. Inhibition/promotion results from H-atom concentration changes.

b. Inhibition/promotion must be catalytic, with cyclic reaction schemes present.

c. One, or more, of the intermediate species, HPO_2, PO, PO_2, and HPO (in probable decreasing order of significance) are the active catalysts for H-atom removal or formation.

d. PN is present in significant quantity (for fuel-rich conditions) but is too stable to enter into a cyclic reaction scheme involving flame radicals, and serves only as a phosphorus sink.

e. PO_2 is present at lower concentrations than expected from its known thermodynamic stability, thus indicating the presence of relatively fast depletion reactions.

f. HPO and the more stable geometrical isomer POH (as estimated by us), are present at very low concentration, in keeping with their relatively low thermodynamic stabilities. Even though the spectroscopic correlation between HPO emission intensity and H-atom concentration (see fig. 18) is indicative of its participation in the inhibition process, the low HPO stability suggests this participation to be of secondary importance.

g. The persistent presence of HPO_2 and PO over a wide range of flame compositions, temperatures and locations suggests that these are the most generally involved species in the inhibition/promotion process.

h. As the cross-over from inhibition to promotion is primarily a temperature dependent phenomenon (see fig. 19), and as no new P-intermediate species are produced, then promotion most likely results from a reversal of one, or more, of the radical depletion reactions listed in table 3.

i. As the degree of promotion increases with temperature, then processes with a highly temperature dependent rate constant must be involved.

To select reactions meeting these criteria requires consideration of individual rate constants and reaction rates. In principle, one should be able to derive rate data from the observed species concentration profiles, e.g., see Cotton and Jenkins (1971) and Jensen and Jones (1974). However, in the present case there are insufficient data for a rigorous analysis of this type. Such an analysis may be worthwhile when more quantitative data are available and particularly with regard to the formation of $NaPO_x$ and $LiPO_x$ (x=1-3) species (see Appendix D) which enter into the measurement of H-atom concentrations.

The following selection of rate constants is therefore based on analogies with other systems but maintaining consistency with the available data from the present study.

Rate Constants: Table 3 lists rate constant data, estimated as follows. As a point of reference, the chain branching reaction ([11] table 3) rate constant at 1800 K is 3.3×10^{-12} molecule^{-1} cm^3 s^{-1} (Baulch et al, 1972).

Reactions analogous to [1] are known to have rate constants in the range of 10^{-27} to 10^{-31} molecule^{-2} cm^6 s^{-1} at 1800 K, where species such as NO, SnO, SO_2, and various metal oxides and hydroxides are involved, as compared with PO for the present case (e.g., see the review of Hastie, 1975, p. 294). We therefore estimate $k_1 \sim 10^{-29\pm2}$ molecule^{-2} cm^6 s^{-1} at 1800 K. The temperature coefficient should be negligible for the present experimental conditions as the reaction is exothermic in the foreward direction. From similar literature studies, reactions of the type [2] have rate constants in the range 10^{-8} to 10^{-10} molecule^{-1} cm^3 s^{-1} and we estimate $k_2 \sim 10^{-9}$ molecule^{-1} cm^3 s^{-1}.

Reactions analogous to [3] are also known. For similar flame conditions to those used in the present study, Jensen and Jones, (1974, 1975) have estimated self-consistent A_f values ranging from 5×10^{-11} to 1.4×10^{-10} (molecule^{-1} cm^3 s^{-1}) for closely analogous reactions involving Fe and Mo species, where M-OH (M=Mo, Fe, or P) bond breaking is involved in each case. The A_f value selected in table 3 falls within this range.

The unexpected low concentration of PO_2 in the flames studied can be used to estimate a rate constant limit, for reaction [4], as follows. From the observed low PO_2 concentration level of $[HPO_2]/[PO_2] > 20$ and the approximation of [4] and [-10] as the main source and sink processes for PO_2, respectively, we have at steady state:

$$k_4 \leq \frac{k_{-10}}{20}\frac{[H_2]}{[H]} \leq 1.8\text{x}10^{-10} \text{ molecule}^{-1} \text{ cm}^3 \text{ s}^{-1} \text{ at 1800 K.}$$

The value of A_5, given in table 3, was estimated to be similar to that for reaction [3], and the exponent was estimated from the reaction endothermicity.

Rate constants for reactions [6] and [7] should be similar to reaction [1]. However, it is reasonable to expect a more efficient energy transfer owing to the greater number of degrees of freedom associated with HPO_2. Hence, we estimate these reactions to be an order of magnitude faster than reaction [1], as indicated in table 3.

Rate constants for reactions [8], [9] and [10] were estimated in a similar fashion to [3], consistent with the entropy and enthalpy constants of the equilibrium reactions.

Reaction Rates: Using the rate constant data summarized in table 3, reaction rates have been calculated for two typical experimental flame systems. Table 4 summarizes results for representative inhibition and promotion conditions. For these calculations, equilibrium P-species concentrations were assumed, except for H and OH where the experimental (H-atom) reaction zone values were used, but with H and OH in partial thermodynamic equilibrium. These approximations should be adequate for reaction ranking purposes, with the known exception of HPO_2 in inhibited flames where a kinetic excess was observed experimentally (fig. 5).

Inhibition Model: As was indicated by the curves of figure 25, catalysed H-atom recombination underlies the inhibition process. From the reactions and rates given in table 4, four such catalytic schemes are possible, each with a similar overall recombination rate. These are: A--[3], [10], [6]; B--[2], [1]; C--[2], [10], [6], [-9]; D--[4], [6]; with the ternary reactions [1] or [6] probably rate limiting. Note that the net result of each scheme is

Table 4

Typical Reaction Rates for Inhibition and Promotion Conditions[e]

	Reaction	Inhibition (1800 K)[a]				Promotion (2500 K)[b]			
		Forward		Reverse		Forward		Reverse	
		k_f	R_f	k_r	R_r	k_f	R_f	k_r	R_r
1.	$PO + H + X^c \rightarrow HPO + X$	1.1(-29)[d]	1.2(22)	--	--	1.1(-29)	1.0(23)	--	--
2.	$HPO + H \rightarrow PO + H_2$	1.1(- 9)	5.2(20)	3.3(-18)	3.0(16)	1.1(- 9)	3.0(21)	8.5(-16)	1.0(18)
3.	$HPO_2 + H \rightarrow PO + H_2O$	1.5(-10)	4.1(21)	5.8(-18)	3.3(16)	1.5(-10)	2.1(22)	1.7(-15)	3.1(19)
4.	$HPO_2 + H \rightarrow PO_2 + H_2$	1.8(-10)	4.9(21)	1.3(-15)	3.9(19)	1.8(-10)	2.6(22)	2.5(-14)	2.3(19)
5.	$PO_2 + H \rightarrow PO + OH$	8.2(-12)	7.2(17)	1.2(-10)	1.3(21)	1.9(-11)	3.5(22)	5.6(-11)	5.5(23)
6.	$PO_2 + H + X \rightarrow HPO_2 + X$	1.5(-28)	5.2(21)	--	--	1.5(-28)	1.0(24)	--	--
7.	$PO + OH + X \rightarrow HPO_2 + X$	1.5(-28)	6.4(19)	--	--	1.5(-28)	5.8(24)	--	--
8.	$HPO_2 + OH \rightarrow PO_2 + H_2O$	1.3(-10)	1.4(20)	5.8(-17)	1.1(16)	1.3(-10)	7.6(22)	3.9(-15)	5.3(22)
9.	$HPO_2 + H_2 \rightarrow HPO + H_2O$	1.5(-10)	1.4(23)	3.7(-15)	3.7(16)	1.5(-10)	1.1(22)	3.4(-14)	1.1(19)
10.	$PO + H_2O \rightarrow PO_2 + H_2$	2.0(-12)	1.2(22)	3.6(-11)	1.1(22)	3.3(-12)	6.1(22)	4.0(-11)	3.6(22)

[a] Typical conditions, representative of the flame $H_2/O_2/N_2$ = 5/1/4.1, used are: $H(10^{-2})$, $OH(4 \times 10^{-4})$, $H_2(0.34)$, $H_2O(0.21)$, $O_2(2.8 \times 10^{-9})$, $PO(1.5 \times 10^{-3})$, $HPO_2(1.8 \times 10^{-4})$, $PO_2(5.8 \times 10^{-5})$, $HPO(3.1 \times 10^{-6})$, with compositions expressed in mole fraction (equivalent to partial pressure at 1 atm) and obtained from equilibrium calculations, except for H and OH.

[b] Typical conditions, representative of the flame $H_2/O_2/N_2$ = 2/1/2.4 used are: $H(6 \times 10^{-3})$, $OH(0.24)$, $H_2(0.03)$, $H_2O(0.45)$, $O_2(8 \times 10^{-3})$, $PO(2.7 \times 10^{-3})$, $HPO_2(1.6 \times 10^{-4})$, $PO_2(2 \times 10^{-3})$ and $HPO(1.2 \times 10^{-6})$ mole fraction.

[c] Represents combined major flame species ($\sim 3.9 \times 10^{18}$ molecule/cm^3).

[d] Computer notation, e.g., 1.1(-29) = 1.1×10^{-29}.

[e] cm^3-molecule-sec units.

$$H + H\ (+X) \rightarrow H_2\ (+X)\ .$$

Also, from the data of figure 25, the uncatalyzed clean-flame rate for this process is,

$$R_o\ (2200\ K) \sim 3.3 \times 10^{20}\ \text{molecule}^{-2}\ \text{cm}^6\ \text{s}^{-1}\ .$$

Even allowing for an order of magnitude uncertainty in the rate data of table 4, the catalytic processes are clearly competitive with the normal mode of H-atom removal. In fact, H-atom abstraction reactions [1], [3], [4], and [6] are competitive with the key chain branching flame propagating reactions with 10 percent of initial O_2 present.

Schemes involving OH + H recombination are possible secondary contributors to flame inhibition, for instance reactions [8] and [6]. In fact, for lean flames reaction [8] will be more dominant than reaction [3] in the inhibition process.

Scheme A is closely analogous to an inhibition process proposed for Ba, as summarized elsewhere (Hastie, 1975, p. 300). Here, HPO_2 serves a similar function to $Ba(OH)_2$. Reactions [10] and [6] have essentially the same rate, under inhibition conditions, and this balancing of PO_2 formation and loss could account for the low steady state concentrations observed experimentally.

The observations of excess HPO_2, relative to PO over a very narrow region within the reaction zone (see fig. 5) can be rationalized as follows. Reaction [6] is shown (table 5) to be the main HPO_2 forming process. Hence, the profile of kinetic HPO_2 (vs equilibrium or balanced HPO_2) should follow that of H, as observed in figure 5 (H data not given but can be shown to fall-off over a similar distance interval to HPO_2).

Model for Inhibition/Promotion Reversal: In comparing the reaction rates for the promoted and inhibited flames, we see in table 4 that reaction [8] is

virtually reversed in the hotter flame. Reaction [-8] provides an additional source of OH and hence H (via reaction [12]), and appears to be the main reaction in flame promotion. This reaction [-8] is also consistent with experimental observations of HPO_2 enhancement and PO_2 depletion. Conversely, reaction [8] probably contributes to the anomalously low HPO_2 concentration in low temperature flames, as shown in figure 6.

Additional factors influencing the promotion process, or loss of inhibition, are a low kinetic excess of H-atoms--reduces R_3, and a high OH concentration--enhances R_{-5}. Both of these factors are present in hotter, leaner flames.

Loss of inhibitor effectiveness with increasing flame temperature has similarly been noted in Ba-containing flames (Cotton and Jenkins, 1971). Reversal of an endothermic radical-depleting reaction was also suggested as the reason for loss of inhibition. In this case the cross-over temperature from inhibition to promotion was about 2000 K, as compared with 2350 K for phosphorus.

3.3.7 Correlation of Inhibition/Promotion Model with Visual Flame Effects

From the model of flame inhibition/promotion, developed from molecular-level H_2 (or CH_4)-O_2-N_2 flame studies, qualitative arguments can now be offered for the visual effects noted earlier for phosphorus-doped hydrocarbon flames (Section 3.3.2).

For the fuel-rich premixed methane, propane, and benzene-air flames, where strong inhibition (and extinction) effects were observed, the temperature can be calculated for an adiabatic system to be considerably less than the inhibition/promotion reversal temperature of 2350 ± 50 K. For the corresponding diffusion flame studies either very weak inhibition (e.g., CH_4 + TMP

case) or strong flame promotion (e.g., propane + TMP, or $POCl_3$) effects were observed. The most significant difference between diffusion and premixed flames is that the former attains a stoichiometric fuel-oxidant interface at the reaction zone, whereas the stoichiometry for the latter is determined by the premixing fuel-air ratio. A stoichiometric condition leads to higher temperature flames, as can be shown thermodynamically and experimentally. Hence diffusion flames will more likely approach, or exceed, the reversal temperature for flame promotion. For hydrocarbon diffusion flames, this critical temperature is probably lower than for premixed H_2-O_2-N_2 flames owing to the following additional factors.

Diffusion flames form lower kinetic concentration levels of H and OH, relative to their fuel-rich counterpart, thereby, increasing the contribution of reactions [-3], [-8], and [-5] to H-atom production. Such flames also form stoichiometric and lean regions, favoring PO_2 and PO over HPO_2 and HPO. Thus, the inhibiting hydroxy-phosphorus intermediates will be much less significant in these regions of diffusion flames.

In making these distinctions between premixed and diffusion flames, we should emphasize that practical diffusion flames contain areas of premixing and can, therefore, often be inhibited in a similar manner to premixed flames.

At least part of the promotion effect of TMP in hotter, leaner flames, including the diffusion case, can be explained thermodynamically since the additive provides additional fuel to the system. Multicomponent equilibrium calculations show significant increases in temperature and H-atom concentrations. However, similar calculations show that thermodynamic effects are negligible in inhibited flames and cyclic non-equilibrium processes are responsible for the observed effects.

4. Conclusions

The main function of halocarbon flame inhibitors (CF_3Br, CH_2ClBr) is to provide a source of catalytically active HBr to the preflame region where the process:

$$H + HBr \rightarrow H_2 + Br \quad ,$$

serves to remove H-atoms and, thereby, reduce flame strength. At high temperatures (> 2500 K) this process can reverse, leading to an enhanced production of H-atoms and flame promotion. These inhibition/promotion processes can also markedly affect the temperature distribution.

Phosphorus-based systems are more effective flame inhibitors than halocarbons, and could possibly replace halogenated safe-fuel additives. Reactions such as,

$$HPO_2 + H \rightarrow H_2O + PO$$

play a significant role in the inhibition process. For hotter flames, radical producing reactions become significant, and above 2300 K contribute to flame promotion; e.g.,

$$PO_2 + H_2O \rightarrow HPO_2 + OH \ .$$

In lean premixed flames or in hot diffusion flames, thermodynamic effects may also contribute to flame promotion owing to the additional fuel value provided by the phosphorus additive. Thus, hydrocarbon diffusion and premixed flames can show flame promotion and related smoke reduction effects in the presence of added phosphorus ($\sim$ 0.1 percent) depending on the temperature. The thermodynamics and kinetics of this inhibition/promotion reversal process have been sufficiently well determined to suggest that other M-OH (M = metal or metalloid) forming systems could show similar behavior. We suggest that a key factor determining the degree of inhibition, and the temperature of inhibition/

promotion reversal, is the strength of the M-OH bond (OH-PO in the case of HPO_2). Stronger M-OH bonds should favor a higher degree of inhibition and a lower reversal temperature.

This study also revealed a number of measurement problems characteristic of conventional flame analysis methods. A comparison of various classical and newly developed (e.g., rotational Raman) methods revealed problems with classical line-of-sight temperature measurements. Also, the normally reliable Li/Na method of H-atom determination was hampered by the formation of the novel flame species $LiPO_x$ and $NaPO_x$ (x=2 and/or 3). Formation of such species, together with the spectroscopically inactive intermediate HPO_2, point to the necessity of carrying out parallel experiments using both mass and optical spectroscopic detection methods.

5. Acknowledgments

A significant portion of this work was supported by the Army Research Office. In the initial stage, support was also provided by the Office of Fire Programs (now CFR), NEL, NBS.

Valuable contributions were made to the early phase of the experimental work by Mr. Angus Rockett (NBS Summer Student) and Ms. C. L. McBee, with technical assistance provided by Mr. Art Sessoms.

6. References

Baulch, D. L., Drysdale, D. D., Horne, D. G. and Lloyd, A. C., (1972) Evaluated Kinetic Data for High Temperature Reactions--Vol. I Homogeneous Gas Phase Reactions of the H_2-O_2 System, Butterworth & Co., Ltd., London.

Biordi, J. C., Lazarra, C. P. and Papp, J. F., (1978) J. Phys. Chem. 82 125.

Brauman, S. K., (1977) J. Fire Retardant Chem. 4 18.

Buchler, A. and Stauffer, J. L., (1966) J. Phys. Chem. 70 4092.

Bulewicz, E. M. and Padley, P. J., (1970) Symp. (Int'l) Combust., 13th, p. 73. Combust. Inst., Pittsburgh, Pennsylvania.

Bulewicz, E. M. and Sugden, T. M., (1956) Trans. Faraday Soc., 1481.

Cotton, D. H. and Jenkins, D. R., (1971) Trans. Faraday Soc. 67 730.

Creighton, J. R. and Lund, C. M., (1979) 10th Materials Research Symposium on Characterization of High Temperature Vapors and Gases, Vol. 2, Section VIII: 1223. NBS SP 561 (J. W. Hastie, ed.) U.S. Govt. Printing Office, Washington, D.C.

Dagnall, R. M., Thompson, K. C., and West, T. S., (1968) Analyst 93 72.

Davies, P. B. and Thrush, B. A., (1968) Proc. Roy. Soc., A302 243.

Dehn, J. T., (1975) Comb. Flame 24 321.

Dehn, J. T., (1976) "Fire-Safe Fuel Development" BRL Report No. 1944, Nov.

Dixon-Lewis, G., (1979) Comb. Flame 36 1.

Drowart, J., Myers, C. E., Shwarz, R., Vander Auwera-Mahieu, A. and Uy, O. M., (1972) J. Chem. Soc., Faraday Trans. II 68 1749.

Fenimore, C. P. and Jones, C. W., (1964) Comb. Flame 8 133.

Fenimore, C. P. and Jones, C. W. (1965) J. Phys. Chem. 69 3593.

Finnerty, A. E., (1975) "The Effect of Halons on the Autoignition of Propane" Proc. Western States Section Comb. Inst., Palo Alto, Calif.

Fristrom, R. M. and Sawyer, R. F., (1971) "Flame Inhibition Chemistry" AGARD Conf. Proc. #84-71 Aircraft Fuels, Lubricants and Fire Safety.

Fristrom, R. M. and Van Tiggelen, P. J., (1978) Symp. (Int'l) Combust., 17th, 773. Combust. Inst., Pittsburgh, Pennsylvania.

Galant, S. and Appleton, J. P., (1975) Theoretical Investigation of Inhibition Pheonmena in Halogenated Flames, 406, in Gann.

Gann, R. G. (ed), (1975) Halogenated Fire Suppressants, ACS Symp. Series 16.

Gingerich, K. A. and Miller, F., (1975) J. Chem. Phys. 63 1211.

Gordon, S. And McBride, B. J., (1971) "Computer Program for Calculation of Complex Chemical Equilibrium Compositions" NASA SP-273.

Grabner, L. and Hastie, J. W., (1980) Boundary Layer Effect on Line of Sight Flame Temperature Measurements, to be published.

Hastie, J. W., (1975) Chapter 5, in "High Temperature Vapors" Academic Press (New York, NY).

Hastie, J. W., (1975-76) Int'l J. Mass Spec. Ion Phys. 16 89.

Hastie, J. W., (1973) Comb. Flame 21 49.

Hastie, J. W., (1974) Chem. Phys. Lett. 26 338.

Hastie, J. W. and Bonnell, D., (1977) Unpublished observations.

Hastie, J. W. and McBee, C. L., (1975) Mechanistic Studies of TriphenylPhosphine Oxide-Poly(Ethyleneterephthalate) and Related Flame Retardant Systems, NBSIR-741.

JANAF (1971) Joint Army Navy Air Force Thermochemical Tables, Second Edition, Stull, D. R. and Prophet, H. (Eds.), NSRDS-NBS 37, U.S. Government Printing Office, Washington, D.C. (and continuing supplements).

Jensen, D. E. and Jones, G. A., (1974) J. Chem. Phys. 60 3421.

Jensen, D. E. and Jones, G. A., (1976) J. Chem. Soc., Faraday Trans. I 72 2618.

Kallend, A. S., (1967) Trans. Faraday Soc. 63, 2442.

Kallend, A. S., (1972) Comb. Flame 19 227.

Kaskan, W. E., (1958) Comb. Flame 2 229.

Larson, E., (1975) J. Fire and Flammability/Fire Retardant Chem. 2 5.

Lask, G. and Wagner, H. G., (1962) Symp. (Int'l) Combust., 8th, 342. Williams and Wilkins, Baltimore, Maryland.

Lovachev, L. A. and Lovachev, L. N., (1978) Comb. Sci. and Tech. 18 191.

Lovachev, L. A. and Lovachev, L. N., (1979) Comb. Sci. and Tech. 19 195.

Miller, D. R., Evers, R. L., and Skinner, G. B. (1963) Comb. Flame 7 137

Muenow, D. W., Uy, O. M. and Margrave, J. L., (1970) J. Inorg. Nucl. Chem. 32 3459.

Padley, P. J. and Sugden, T. M., (1959) Symp. (Int'l) Combust., 7th, Butterworth, London, 235.

Peeters, J. and Mahnen, G., (1973) Symp. (Int'l) Combust., 14th, 133, Combust. Inst., Pittsburgh, Pennsylvania.

Petrella, R., (1979) J. Fire Retardant Chem. 6 125.

Reuther, J. J., (1979) 10th Materials Research Symp. on Characterization of High Temperature Vapors and Gases, Vol. 2, Section VIII: 1281, NBS SP-561 (J. W. Hastie, ed.) U.S. Govt. Printing Office, Washington, D.C.

Smoes, S. and Drowart, J., (1974) Disc. Faraday Soc.

Steblevskii, A. V. and Alikhanyan, S. S., (1978) Russian J. Inorg. Chem. 23 173.

Vanpee, M. and Shirodhar, P., (1978), Symp. (Int'l) Combust, 17th, 787, Combust. Inst. Pittsburgh, Pennsylvania.

Vanzee, R. J. and Khan, A. U., (1976), J. Chem. Phys. 65 1764.

Weatherford, W. D., Jr. and Wright, B. R., (1976) Corrective Action Program for Bromochloromethane Containing "Fire-Safe" Diesel Fuel. AD-A043323 (AFLRL #81) Final Report.

Figure Captions

1. Calculated equilibrium partial pressures of H, OH and O in adiabatic, 1 atm $H_2/O_2/N_2$ flames with $N_2/O_2 = 3.72$.

2. Calculated effect of temperature on equilibrium H-atom concentration for the $H_2/O_2/N_2 = 3/1/3.72$ flame system.

3. Mass spectrometric ion intensity versus distance profiles for a premixed promoted $H_2/O_2/N_2$ flame showing H-atom enhancement in the presence of CF_3Br. The flame was supported on a laboratory torch with 1 cm downstream distance-from-reaction zone ($\sim$ 0.3 cm) equivalent to 1 ms flow time. Ion intensities were recorded several eV above appearance potential to reduce fragment ion contributions. The Br profile (dashed curve) was not recorded for this particular flame and was estimated from data obtained (by us) for cooler flames. Also shown are the calculated equilibrium partial pressures for the main product species obtained using the JANAF (1971) data base and an estimated value of $\Delta H_{f,298}{}^{CF_3Br} = -149.7 \pm 10$ kcal/mol. The calculations indicate no change in [H]-equilibrium and only a 4° flame cooling effect is predicted for addition of 0.13 percent CF_3Br.

4. Photographic observations (a - n) of various premixed and diffusion flames with and without inhibiting/promoting phosphorus additives. Constant burner gas flows were maintained with and without additive.

5. Typical P-species partial pressure vs distance profiles in a premixed $CH_4/O_2/Ar$ flame, supported on a laboratory torch, at a maximum temperature of about 2300 K ($z > 0.2$ cm). Data obtained along the primary gas flow axis. Mass spectrometric observations of the positive ions were made several eV above appearance potential. The known post flame pressures of H_2O and Ar were used to determine the relationship between ion intensity and partial pressure from which P-species pressures were derived.

Similar ionization cross sections were assumed for each species, hence the slight mass inbalance between P-added (as triphenylphosphine oxide vapor) and product species. The 1 ms marker indicates the position equivalent to 1 ms flow time from the luminous reaction zone at Z. Calculated equilibrium partial pressures are indicated in the right hand margin. These calculations utilized the upgraded JANAF (1971) data base with $\Delta H_{f,298}HPO_2$ = -96 kcal/mol (see Appendix E).

6. Comparison of experimental HPO_2 concentration data, relative to PO, with the predicted values based on the assumption of local thermodynamic equilibrium between HPO_2 and PO. The circles represent experimental values (data given in table 2), with uncertainties indicated by the vertical bars. The solid curve A indicates the predicted trend of HPO_2 with temperature. The rectangles represent the region of uncertainty in the predicted data, arising solely from the experimental temperature errors associated with the data points. In calculating the predicted curve A, the upgraded JANAF (1971) data base was used including the new species and/or thermodynamic functions for PO, PO_2, HPO_2 ($\Delta H_{f,298}$ = -96 kcal/mol), HPO and trimethylphosphate. The predicted curve B shows the effect of reducing the HPO_2 stability by 8 kcal/mol ($\Delta H_{f,298}$ = -88 kcal/mol). Curve C is a fit of the experimental points.

7. H-atom partial pressure vs distance/time profiles for a relatively cool premixed $H_2/O_2/N_2$ flame with (closed symbols) and without (open symbols) TMP present. The indicated equivalent time scale, relative to the reaction zone [R(P) for P present and R for clean flame] as origin, was calculated from the known gas input volumetric flow rate, burnt gas column dimensions and temperature. Curve A represents clean flame data, corrected for a small amount of NaOH present. Curve B shows the effect

of added TMP and was calculated from the raw Na and Li emission intensities. Curve C shows the effect of $NaPO_2$ and $LiPO_2$ formation (see Appendix D) on the apparent H-pressures, assuming no inhibition occurs. Curve D was obtained from the curve B data by correcting for the presence of $NaPO_2$, $LiPO_2$ and NaOH and represents the true H-pressure curve in the presence of TMP. Correction for new species formation was made using the expression relating emission intensities to partial pressures,

$$\frac{Na_p}{Na_c} = 1 - \left[\frac{H_c}{H_e}\right] \left[\frac{NaPO_2 + \Delta NaOH}{NaPO_2 + Na}\right]_e ,$$

where the notation p, c and e refers to phosphorus-containing, clean and calculated equilibrium partial pressures respectively, and $\Delta NaOH = NaOH_c - NaOH_p$, as calculated by the multicomponent equilibrium method. An analogous expression was used for Li (except $\Delta LiOH = 0$). Curve E (coincident with curve D) represents the calculated equilibrium H-atom partial pressure in the presence of TMP.

8. H-atom partial pressure vs distance/time profiles for a medium temperature premixed $H_2/O_2/N_2$ flame with (closed symbols) and without (open symbols) TMP present. For curve notation see the figure 7 caption.

9. H-atom partial pressure vs distance/time profiles for a relatively cool lean $H_2/O_2/N_2$ flame with (closed symbols) and without (open symbols) TMP present at a relatively low concentration level. For curve notation see the figure 7 caption. Curve N represents the clean flame data uncorrected for the presence of NaOH. Curves A and D represent the true H-atom profiles for the clean and TMP-containing flames, respectively.

10. H-atom partial pressure vs distance/time profiles for a high temperature stoichiometric premixed $H_2/O_2/N_2$ flame with (closed symbols) and without (open symbols) TMP present at a relatively low concentration level. For curve notation see the figure 7 caption. Curves A (open circles) and D (closed triangles) represent the true species-corrected profiles for the clean and TMP-promoted flames, respectively.

11. H-atom partial pressure vs distance/time profiles for a high temperature stoichiometric premixed $H_2/O_2/N_2$ flame with (closed symbols) and without (open symbols) TMP present at a relatively high concentration level. For curve notation see the figure 7 caption. Curves E(p) and E(c) represent calculated equilibrium values, at 2450 K, in the presence and absence of TMP, respectively. The two vertical error bars indicate the effect of a factor of two increase in $NaPO_2$ and a corresponding decrease in $LiPO_2$, (see Appendix D), arising from the combined uncertainties in [P], T and the thermodynamic functions used, in decreasing order of likely significance.

12. Temperature (Na line reversal) vs distance profiles for representative hot and cool premixed $H_2/O_2/N_2$ flames where promotion and inhibition effects were present, respectively. For the 2/1/2 flame, two independent data sets are given, set 1--square symbols and set 2--triangle symbols. Each data set used a different burner and gas flow rate. Data set 1 was obtained with the same burner and flow conditions used to obtain the H-atom data of figure 11. The cool flame conditions correspond to those of figure 7.

13. Temperature dependence of thermal emission for Na (open circles) and HPO (closed circles). Total concentrations of Na and P-species added were 2×10^{-6} and 8.6×10^{-4} mole fraction, respectively. The solid curves

have the theoretical slopes for thermal emission. Each data point represents a different $H_2/O_2/N_2$ flame composition. The Na (max) data were obtained at the flame location of maximum temperature and at post-flame flow time in excess of 1 ms. The HPO data were obtained at post-flame flow times of $\sim$ 1 ms.

14. Emission intensity vs distance profiles for OH (307.9 nm) in clean (open circles) and TMP-inhibited (closed circles) premixed $H_2/O_2/N_2$ flames.

15. Emission intensity vs distance profiles for OH (307.9 nm) in clean (open circles) and TMP-promoted (closed circles) premixed $H_2/O_2/N_2$ flames.

16. Emission intensity vs distance profile for PO (322.8 nm) in a TMP-inhibited premixed $H_2/O_2/N_2$ flame.

17. Emission intensity vs distance profiles for HPO (612.2 nm) in a TMP-inhibited premixed $H_2/O_2/N_2$ flame.

18. Correlation of HPO emission intensity (612.2 nm) with H-atom partial pressure in a TMP-inhibited premixed $H_2/O_2/N_2$ flame.

19. Temperature dependence of flame inhibition/promotion, where percent change in [H] is given by:

$$\% \Delta [H] = \left\{ \left[[H]_p - [H]_c \right] \Big/ [H]_c \right\} \times 100 \quad ,$$

and similarly for OH. Data were obtained in the vicinity of the reaction zone (i.e., close to burner face) and represent the points of maximum additive-induced change in H-atom partial pressure or OH-thermal emission. Flame identifications, expressed as point-number and $H_2/O_2/N_2$ unburnt gas NTP mole ratios, are as follows: 1 (5/1/4.1), 2 (3.7/1/3), 3 (3/1/3.7), 4 (3/1/3.7--duplicate run of point 3), 5 (3/1/2.6), 6 (3/1/2.6), 7 (1/8/1/4.3), 8 (2/1/2), 9 (3.7/1/2.1), 10 (2/1/2), and

11 ($CH_4/O_2/N_2$ = 0.53/1/0.8). For data point 5, $POCl_3$ was the inhibiting additive (10^{-2} atm). All other data points refer to TMP additive at concentrations equivalent to 4.5 (±20 percent) $x10^{-3}$ atm, except for point 7 where TMP = $4x10^{-4}$ atm. For data points 6, 9, and 10, OH thermal emission changes were used as measures of inhibition/promotion. The closed-circle points were calculated using apparent H-atom partial pressures without correction for the formation of $LiPO_2$ and $NaPO_2$ (see Appendix D).

20. Calculated thermodynamic equilibrium effects of TMP addition on flame temperature and H-atom mole fraction [H]. The JANAF (1971) data base used was supplemented (see Appendix E) with new species and/or thermodynamic functions for PO, PO_2, HPO_2, HPO, and trimethylphosphate ($\Delta H_{f,298}$ est ∿ 10±3 kcal/mol).

21. Calculated equilibrium distribution of P and alkali-metal-containing species in the experimental flame $H_2/O_2/N_2$ = 5/1/4.1, [P] = $4.4x10^{-4}$ atm, and [Li], [Na] = $3x10^{-6}$ atm. The JANAF (1971) data base was used with the following exceptions. For data set A, the new species $NaPO_2$ was taken to have a 6 kcal/mol lower heat of formation (at 298 K) and a 3 cal/deg mol lower entropy (at 298 K) than the optimum data used for set B. Also, the new species, $LiPO_2$, HPO_2 and HPO were added to the data base using the thermodynamic functions given in Appendix E. For data set B, the JANAF (1971) data for PO and PO_2 were updated to include the recent, and demonstrably more accurate, heat of formation data of Drowart, et al., (1972), as described in Appendix E. For data set A, an interim value for the HPO_2 heat of formation, based on the JANAF (1971) values for PO and PO_2, was used ($\Delta H_{f,298}$ = -88 kcal/mol). For data set B, an optimum values of $\Delta H_{f,298}$ = -96 kcal/mol (see Appendices D and E).

22. Calculated equilibrium distribution of P- and alkali-metal-containing species in the experimental flame $H_2/O_2/N_2$ = 3.7/1/3, [P] = 5.4×10^{-3} atm and [Li],[Na] = 2.8×10^{-6} atm. The upgraded JANAF (1971) data base, as defined for data set B, figure 21 and described in Appendix E, was used.

23. Calculated equilibrium distribution of H, P and alkali-metal-containing species in the experimental flame $H_2/O_2/N_2$ = 2/1/2, [P] = 4.6×10^{-3} atm and [Li],[Na] = 2.8×10^{-6} atm. The upgraded JANAF (1971) data base was used (see fig. 21 caption and Appendix E).

24. Calculated equilibrium distribution of H-atom and P-containing species as a function of added TMP concentration for the experimental flame $H_2/O_2/N_2$ = 1.8/1/4.3, T = 2200 K. The dashed curve represents the H-atom data where the small heating effect of added TMP is included. TMP acts as a fuel in this lean flame. The upgraded JANAF (1971) data base was used for these calculations (see fig. 21 caption and Appendix E).

25. Reciprocal H-atom partial pressure vs time-from-reaction-zone plots, with and without TMP present, showing second order rate behavior and efficient (efficiency = slope D/slope A = 2.7) catalysed radical recombination (same raw data as for fig. 7). The break in curve D (TMP added) corresponds to equilibration of the H-atom partial pressure at times greater than 0.7 ms. For curve terminology see figure 7 caption.

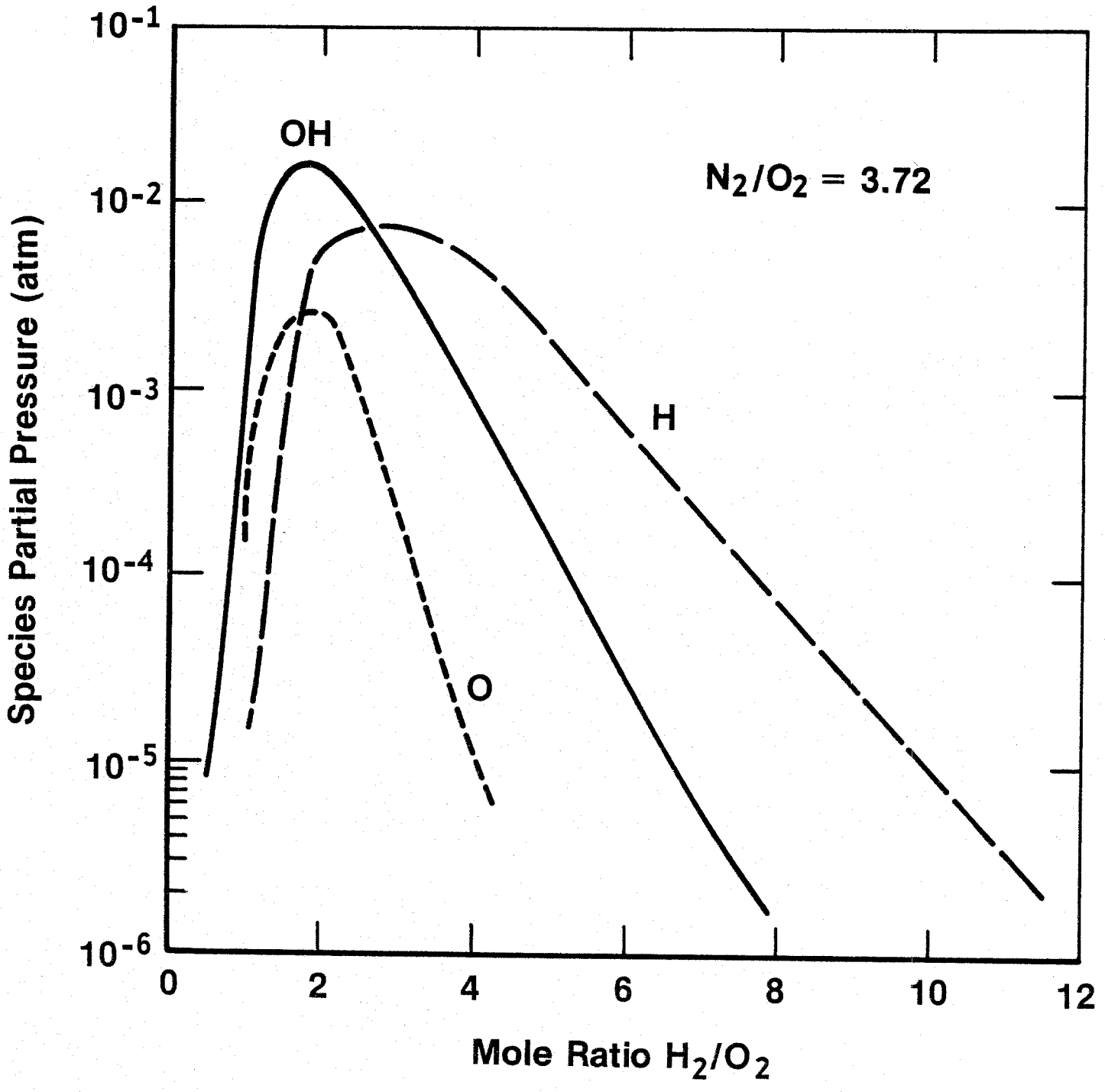
Species Partial Pressure (atm)
10^{-1}
10^{-2}
10^{-3}
10^{-4}
10^{-5}
10^{-6}
OH
$N_2/O_2 = 3.72$
H
O
0
2
4
6
8
10
12
Mole Ratio H_2/O_2

Figure 1

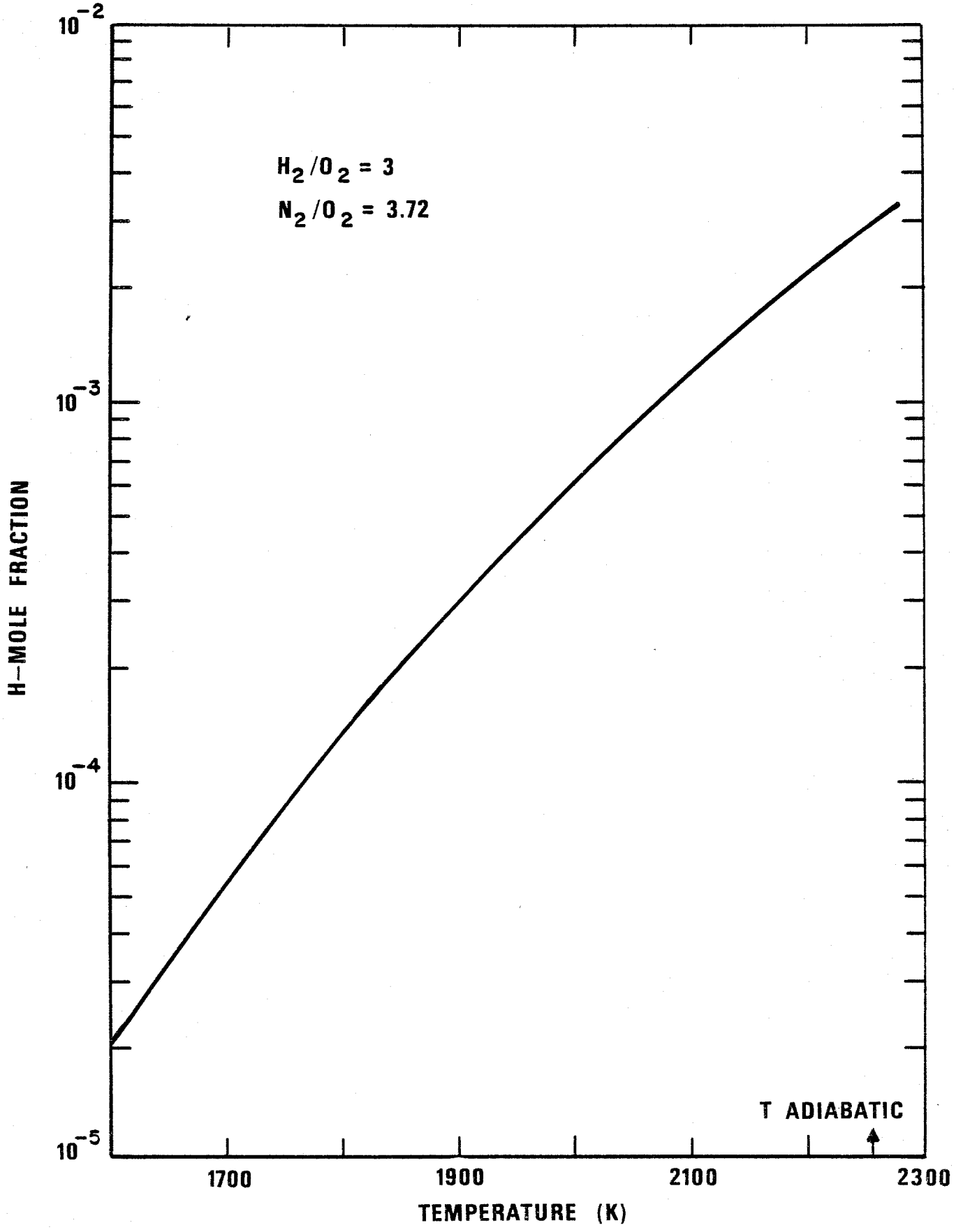
10^{-2}
10^{-3}
10^{-4}
10^{-5}
$H_2/O_2 = 3$
$N_2/O_2 = 3.72$
H-MOLE FRACTION
T ADIABATIC
1700
1900
2100
2300
TEMPERATURE (K)

Figure 2

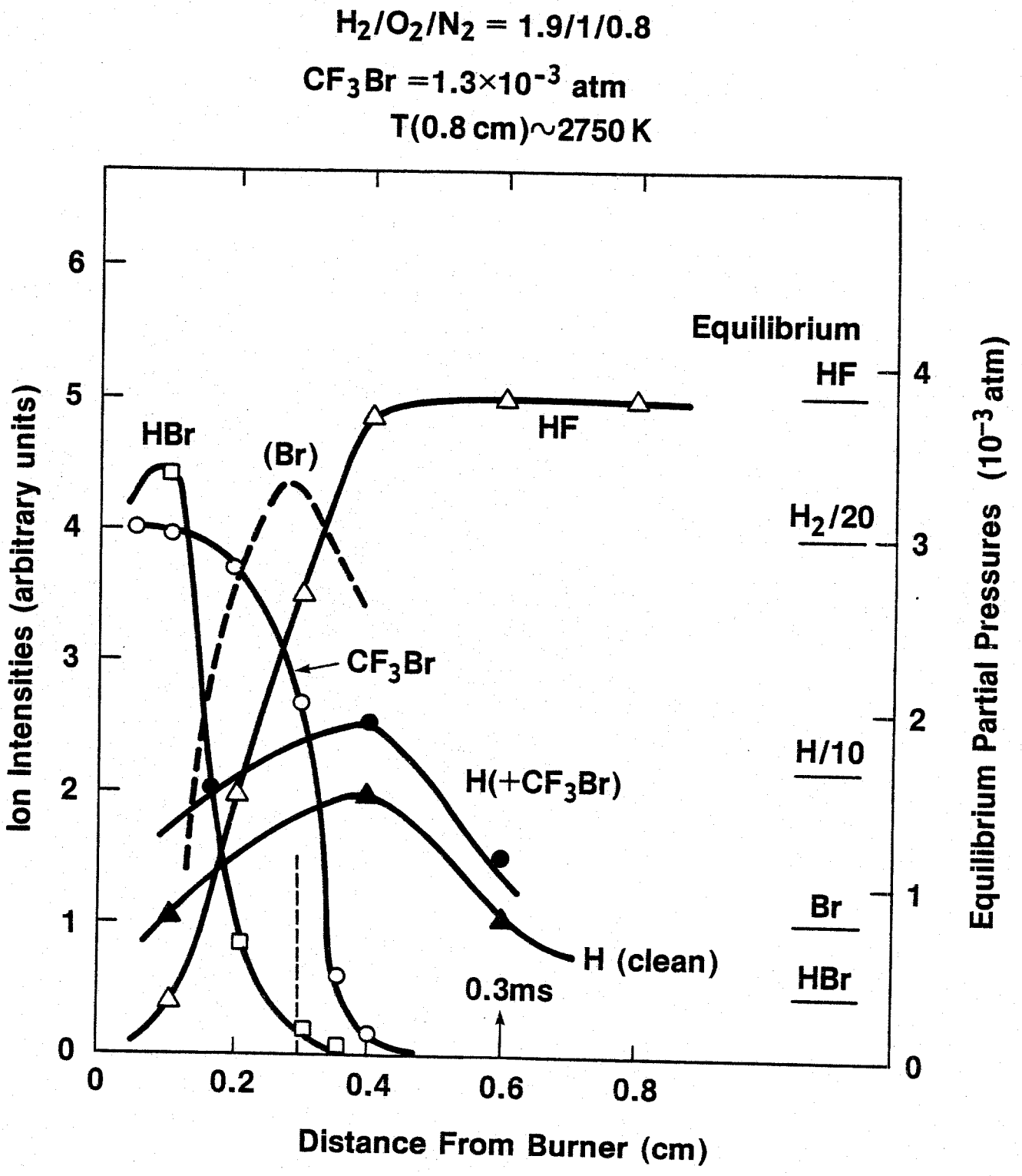
$H_2/O_2/N_2$ = 1.9/1/0.8
CF_3Br =1.3×10^{-3} atm
T(0.8 cm)~2750 K
Ion Intensities (arbitrary units)
Equilibrium Partial Pressures (10^{-3} atm)
Distance From Burner (cm)
HBr
(Br)
HF
CF_3Br
H(+CF_3Br)
H (clean)
0.3ms
Equilibrium
HF
H_2/20
H/10
Br
HBr
0
0.2
0.4
0.6
0.8
1
2
3
4
5
6

Figure 3

FLAME INHIBITION/SMOKE ENHANCEMENT

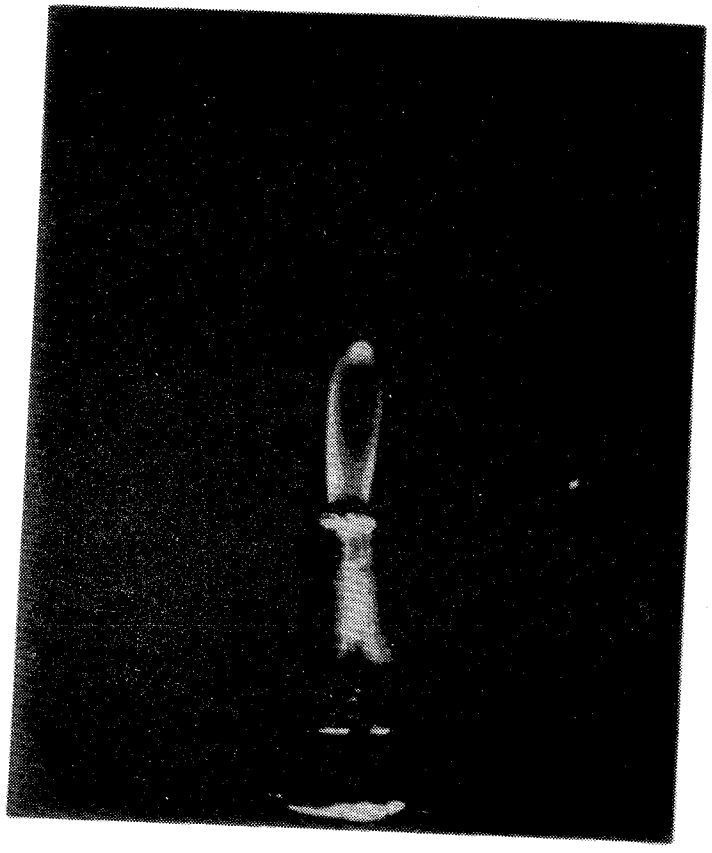

PROPANE + AIR

(a)

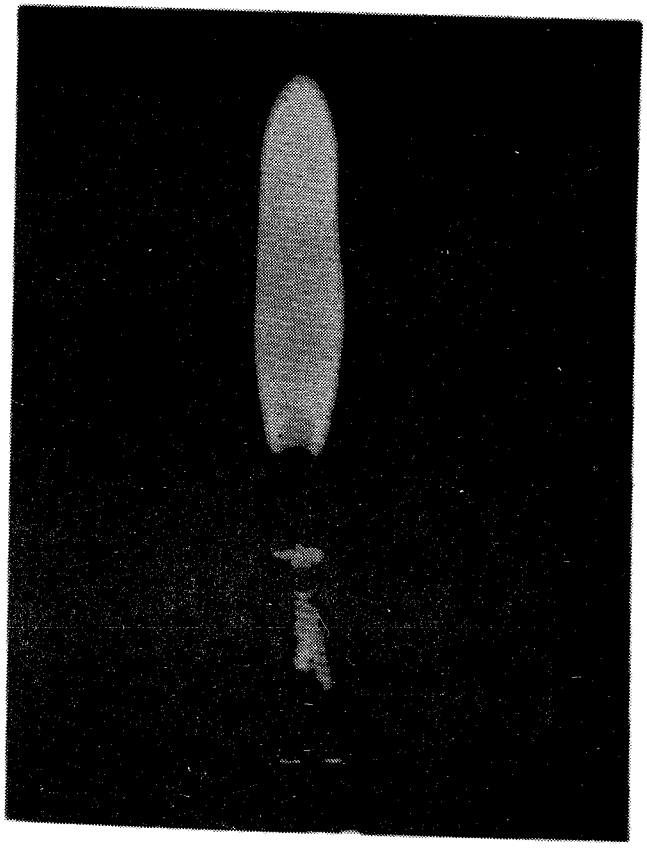

PROPANE + AIR
+ $POCl_3$ (0.04)

(b)

Figure 4

SMOKE REDUCTION

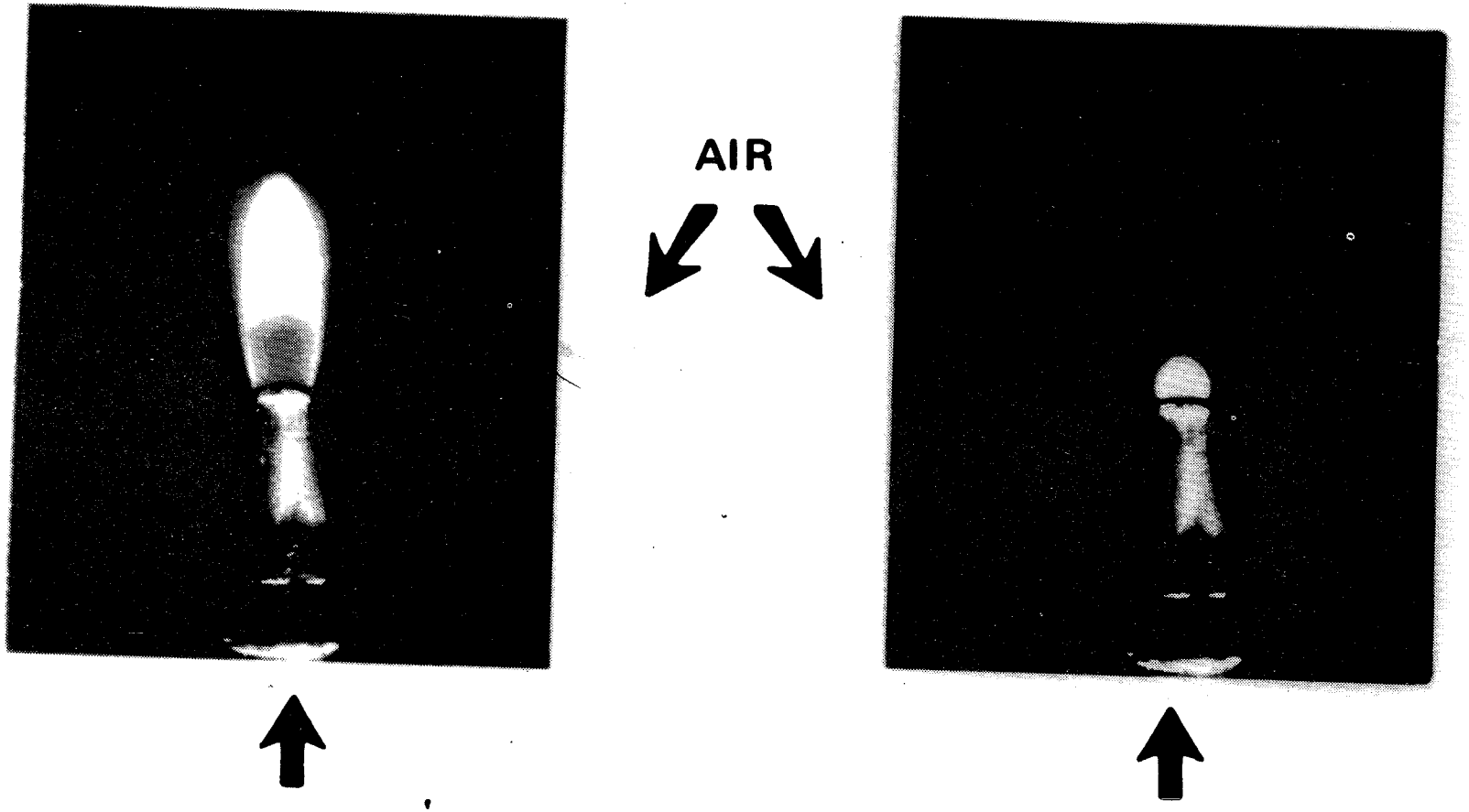

(c)

(d)

Figure 4

FLAME INHIBITION/SMOKE ENHANCEMENT

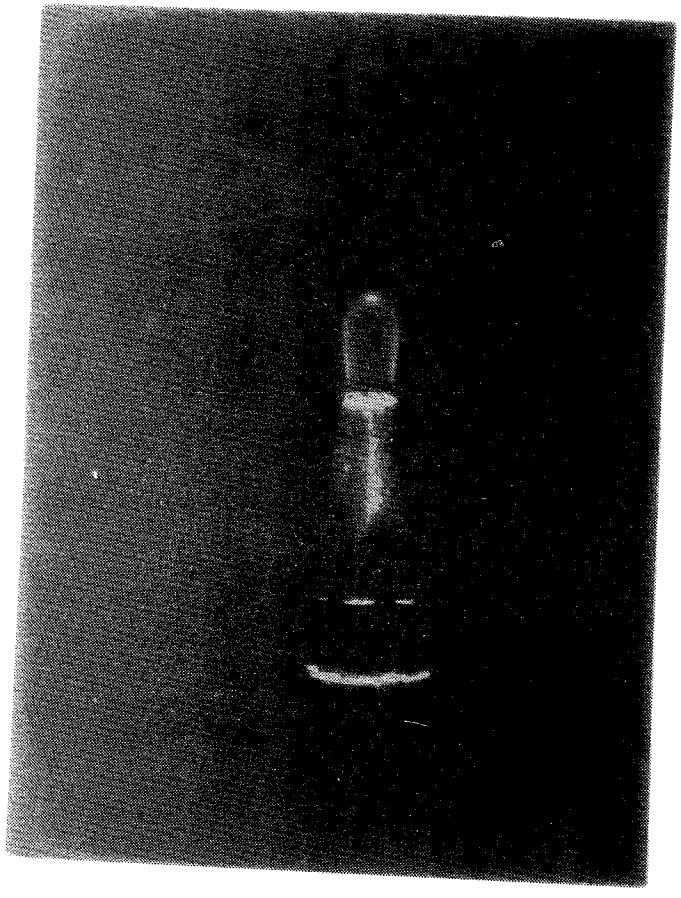

PROPANE + AIR

(e)

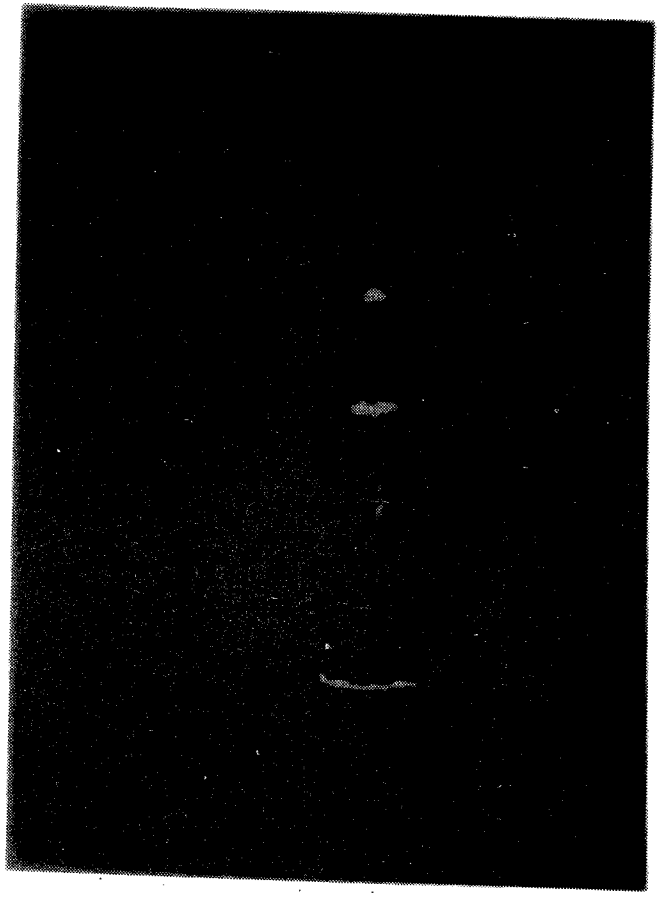

PROPANE + AIR
+ TMP (10^{-3})

(f)

Figure 4

SMOKE REDUCTION

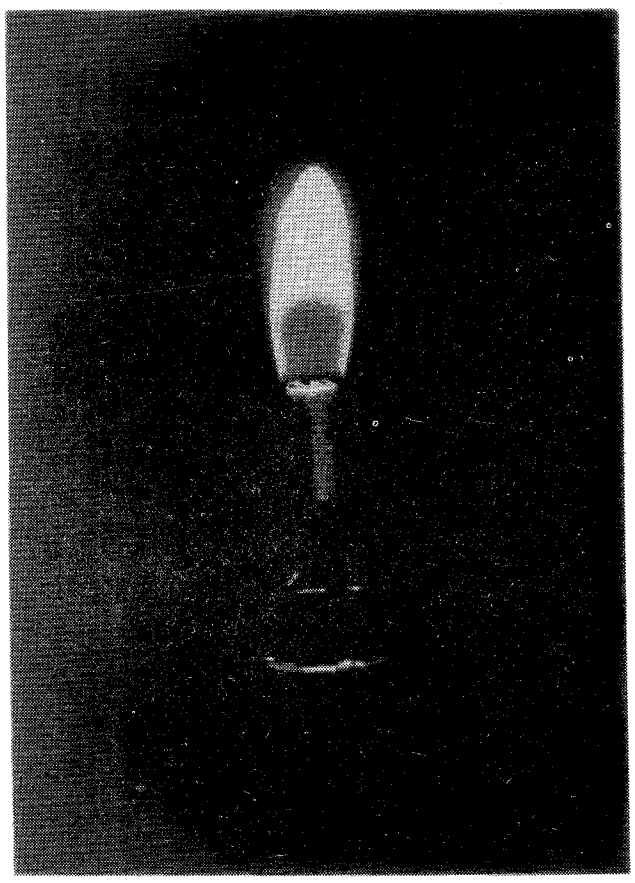

AIR

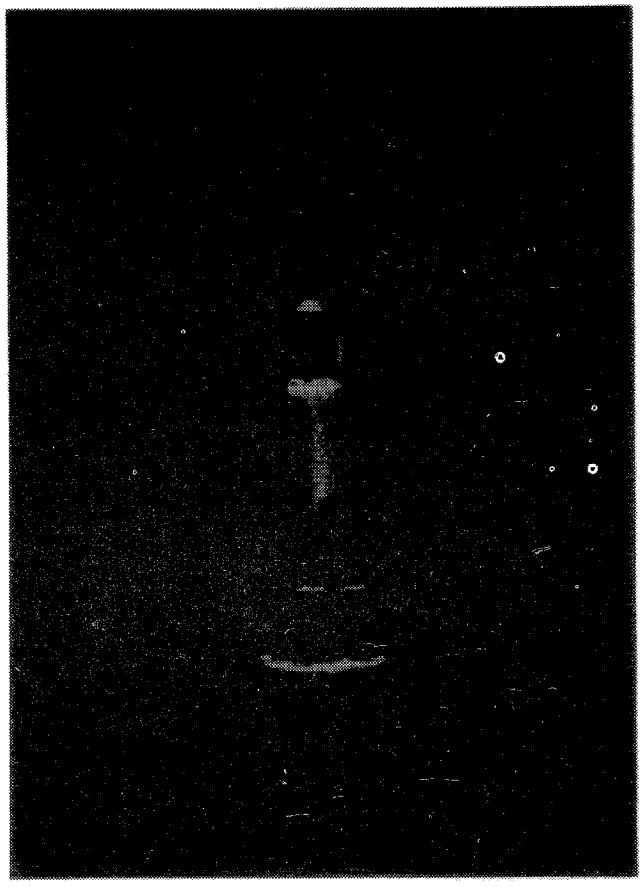

PROPANE

(g)

PROPANE + TMP (10^{-3})

(h)

Figure 4

FLAME INHIBITION

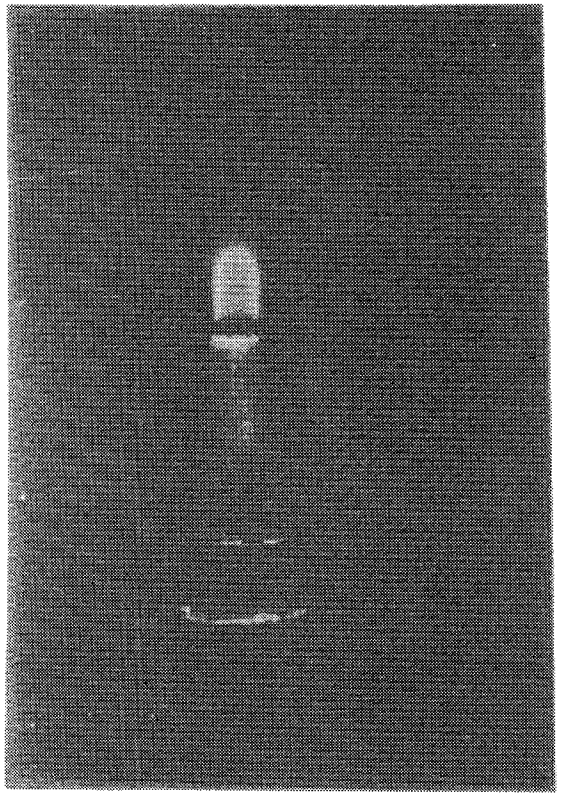

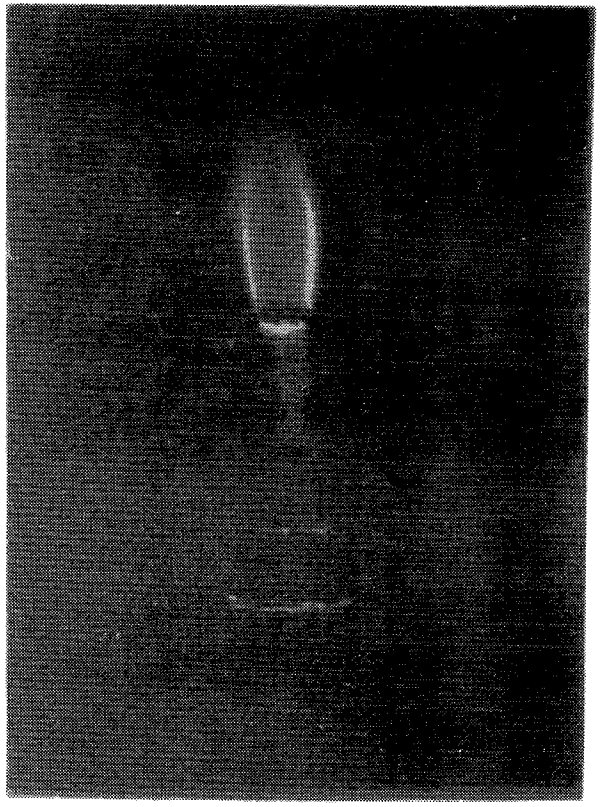

METHANE + AIR

(i)

METHANE + AIR
+ TMP (10^{-3})

(j)

Figure 4

FLAME INHIBITION/SMOKE ENHANCEMENT

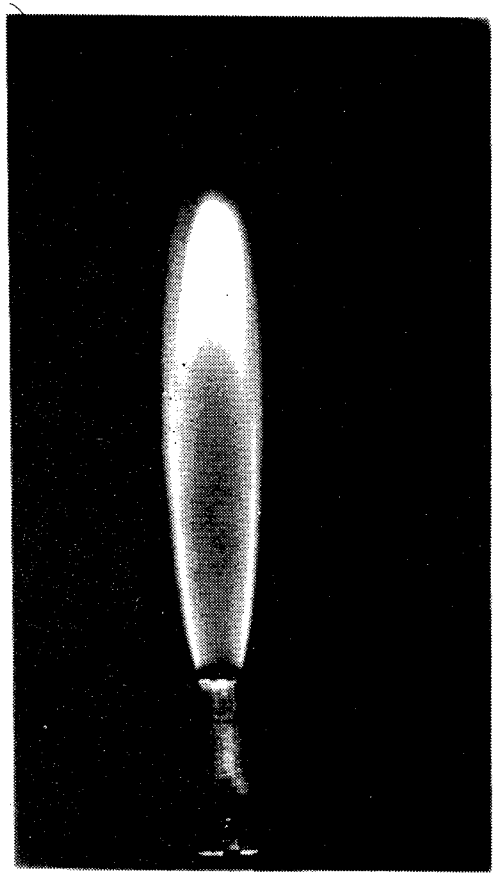

METHANE + AIR

(k)

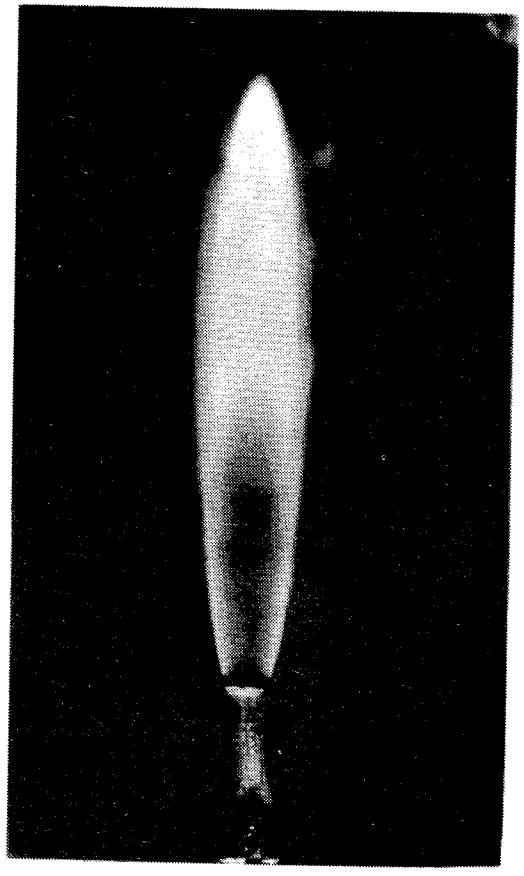

METHANE + AIR
+ TMP (10^{-3})

(l)

Figure 4

SMOKE ENHANCEMENT

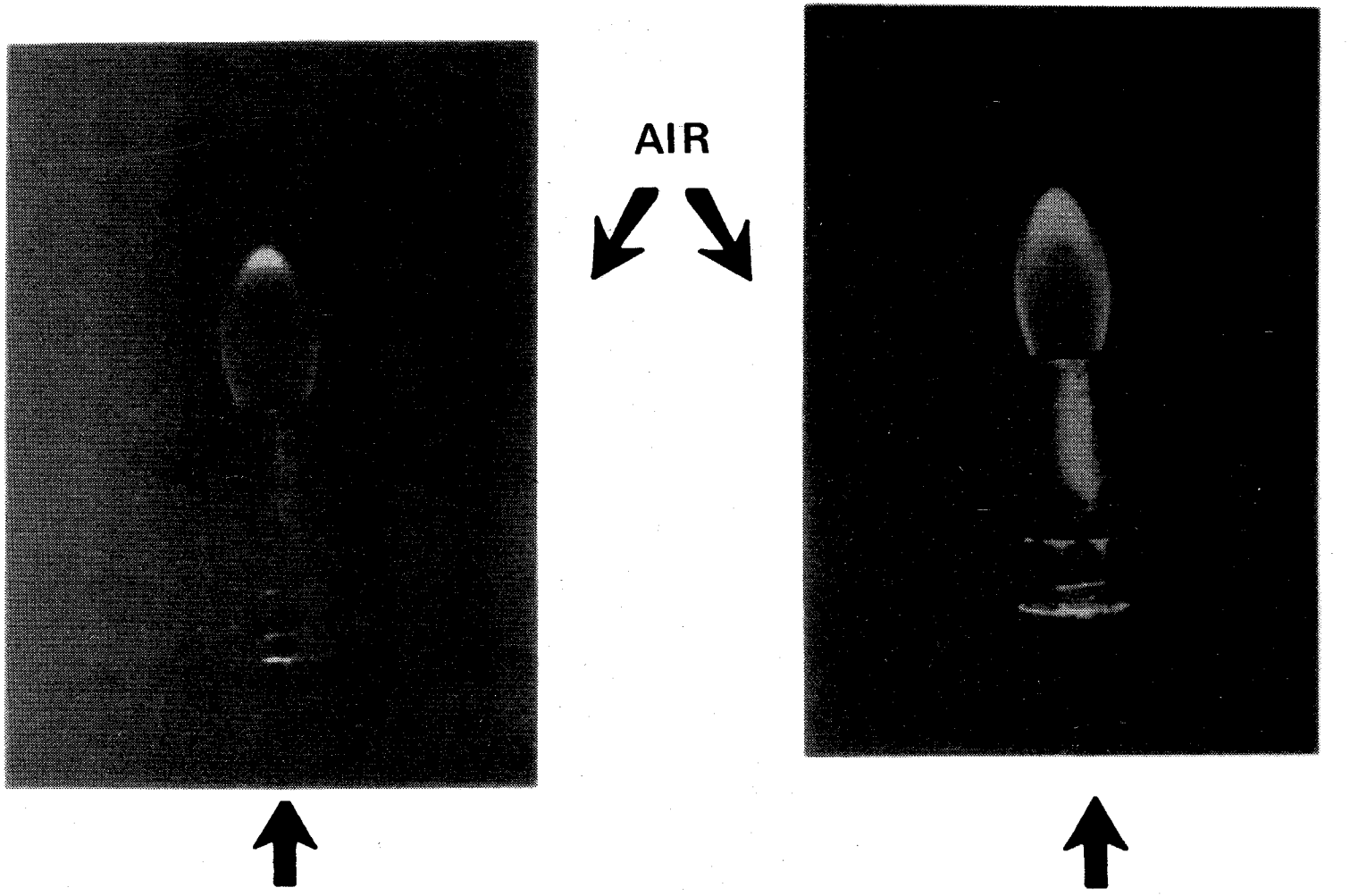

Figure 4

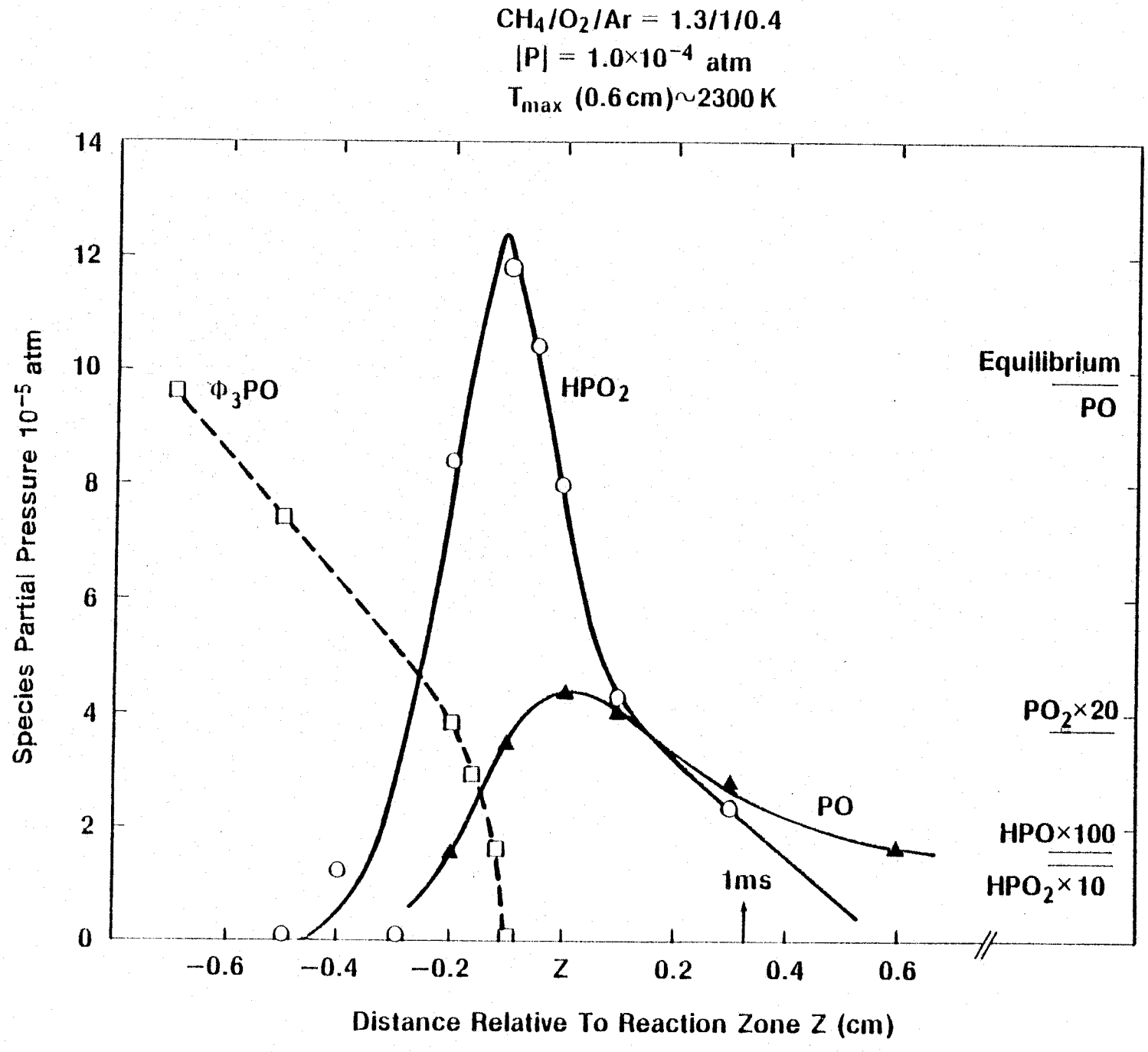
$CH_4/O_2/Ar = 1.3/1/0.4$
$[P] = 1.0\times10^{-4}$ atm
T_{max} (0.6 cm)$\sim$2300 K
Species Partial Pressure 10^{-5} atm
14
12
10
8
6
4
2
0
Φ_3PO
HPO_2
Equilibrium
PO
$PO_2\times20$
PO
HPO×100
$HPO_2\times10$
1ms
−0.6
−0.4
−0.2
Z
0.2
0.4
0.6
Distance Relative To Reaction Zone Z (cm)

Figure 5

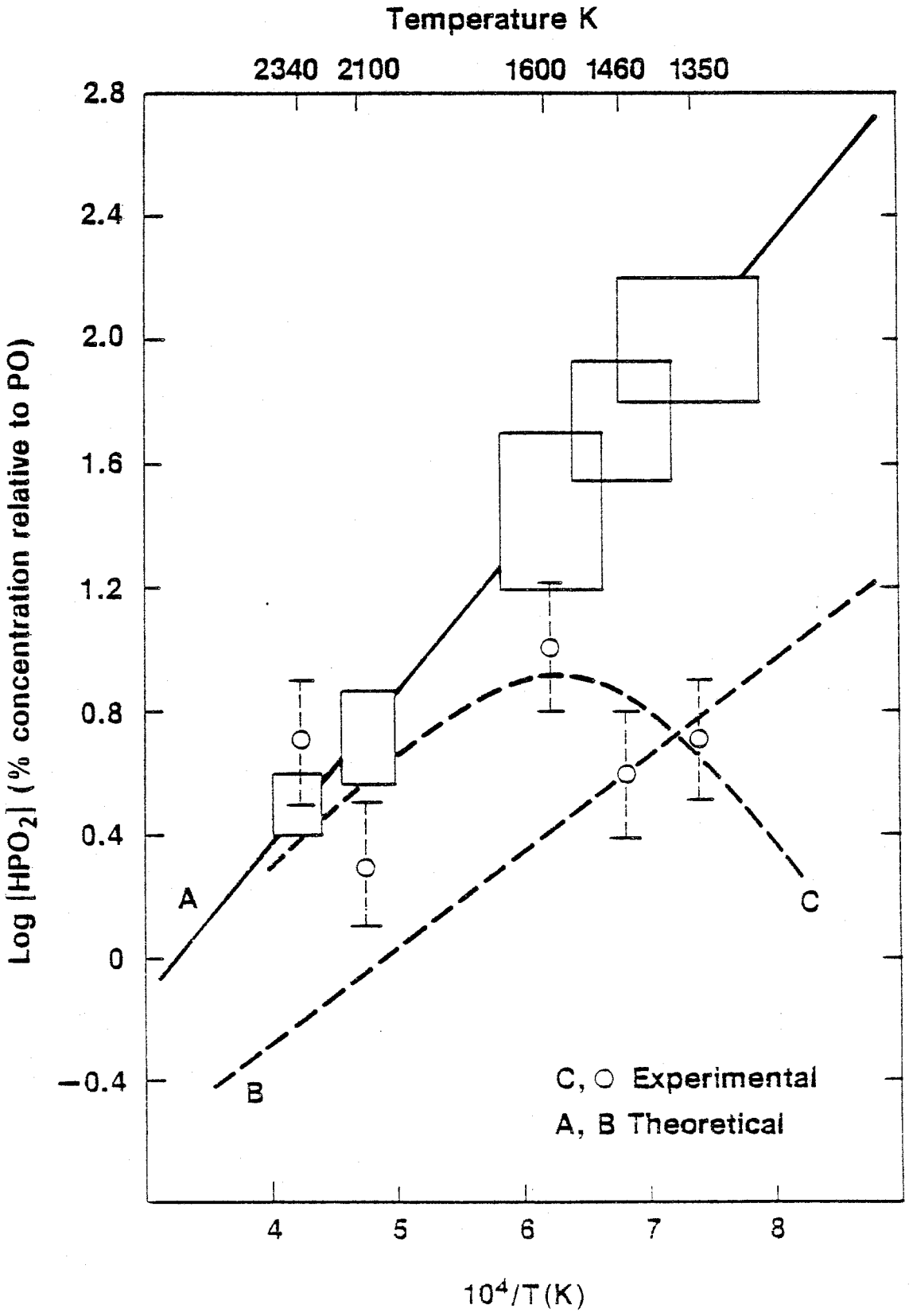
Temperature K
2340 2100 1600 1460 1350
2.8
2.4
2.0
1.6
1.2
0.8
0.4
0
−0.4
Log [HPO2] (% concentration relative to PO)
A
B
C
C, ○ Experimental
A, B Theoretical
4
5
6
7
8
10⁴/T (K)

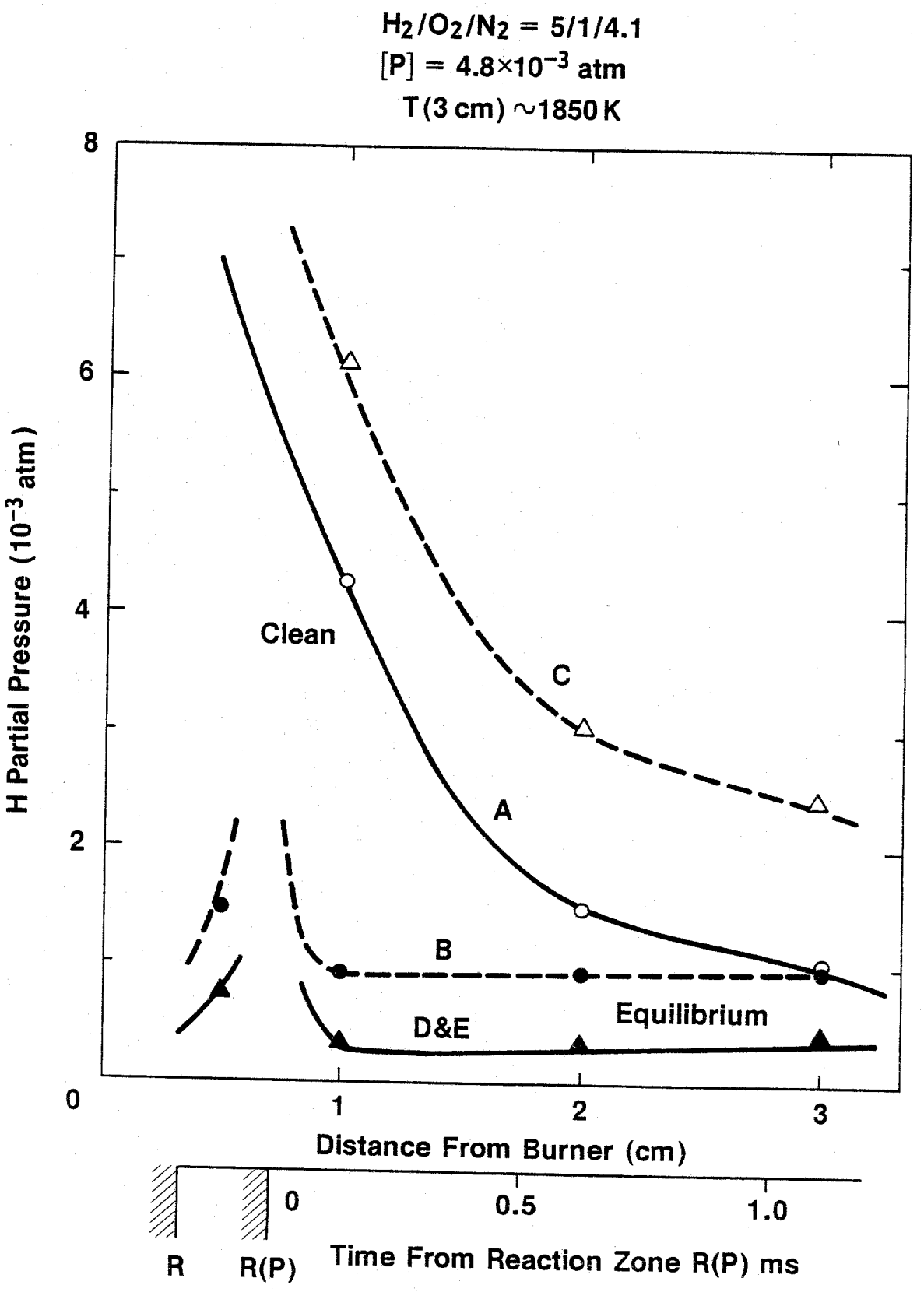
$H_2/O_2/N_2$ = 5/1/4.1
[P] = 4.8×10^{-3} atm
T(3 cm) ~1850 K
H Partial Pressure (10^{-3} atm)
8
6
4
2
0
Clean
C
A
B
D&E
Equilibrium
1
2
3
Distance From Burner (cm)
0
0.5
1.0
R
R(P)
Time From Reaction Zone R(P) ms

Figure 7

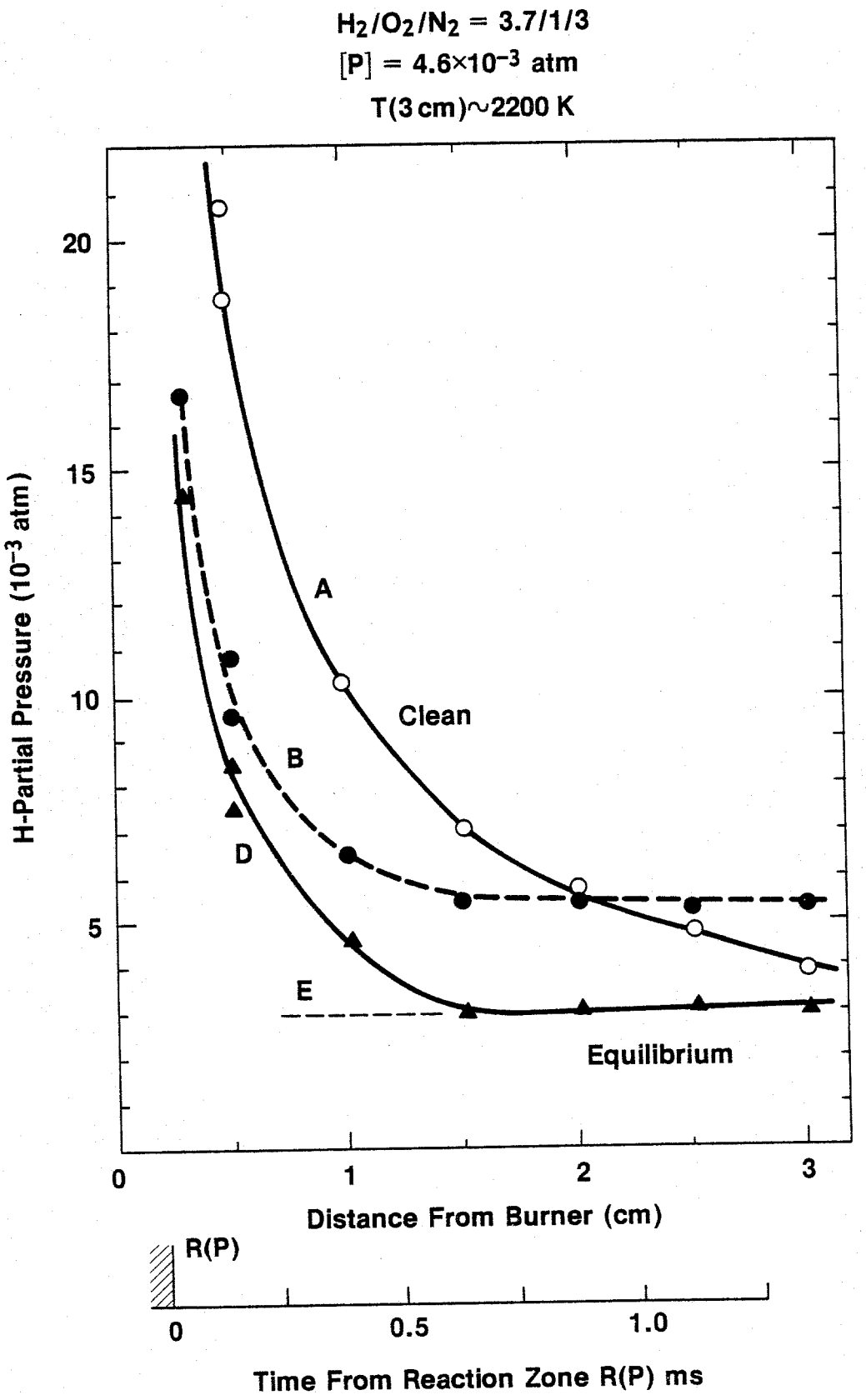
$H_2/O_2/N_2$ = 3.7/1/3
[P] = 4.6×10^{-3} atm
T(3 cm)~2200 K
H-Partial Pressure (10^{-3} atm)
20
15
10
5
A
Clean
B
D
E
Equilibrium
0
1
2
3
Distance From Burner (cm)
R(P)
0
0.5
1.0
Time From Reaction Zone R(P) ms

Figure 8

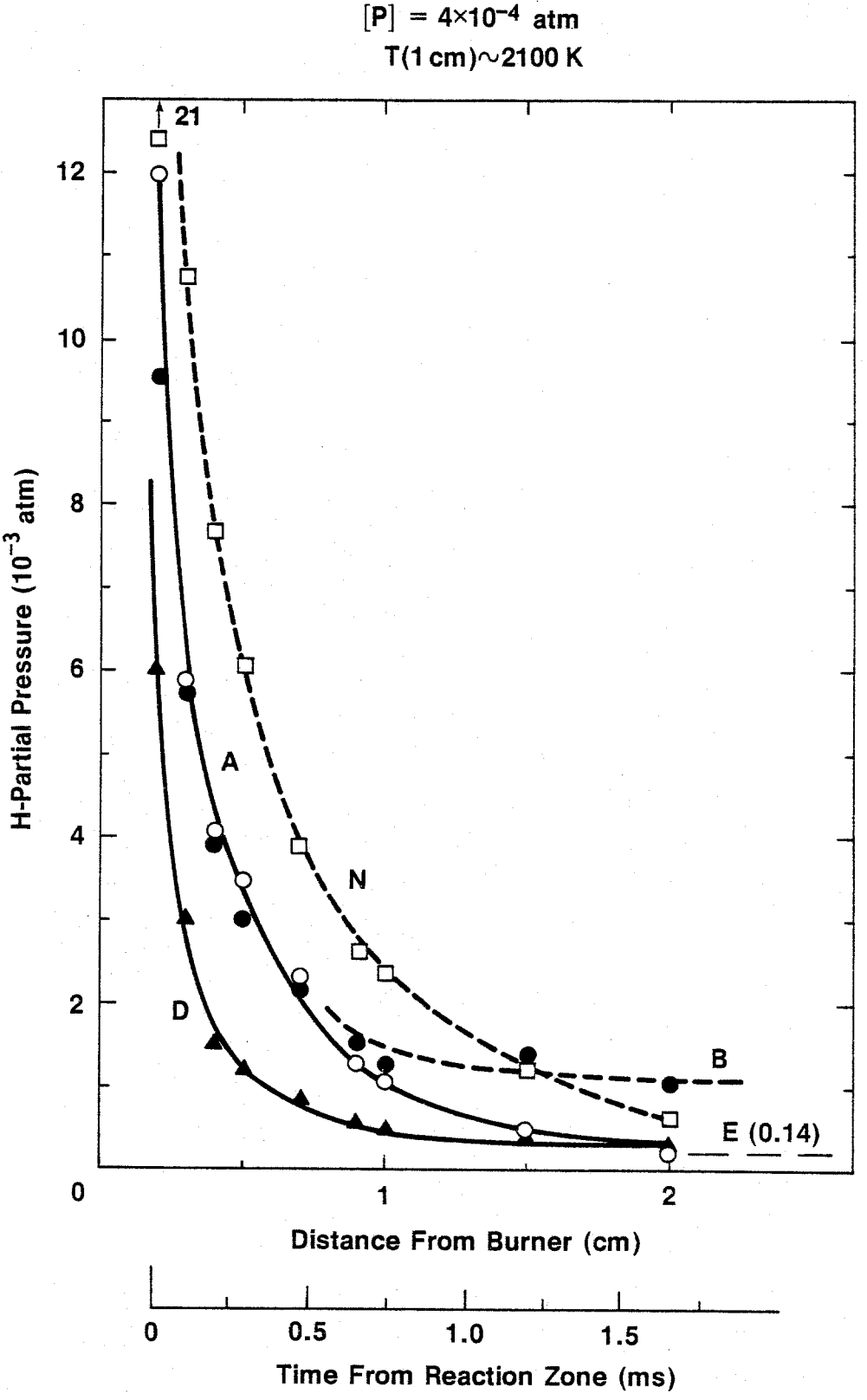
$H_2/O_2/N_2$ = 1.8/1/4.3
[P] = 4×10^{-4} atm
T(1 cm)~2100 K
21
12
10
8
6
4
2
0
H-Partial Pressure (10^{-3} atm)
A
N
D
B
E (0.14)
1
2
Distance From Burner (cm)
0
0.5
1.0
1.5
Time From Reaction Zone (ms)

Figure 9

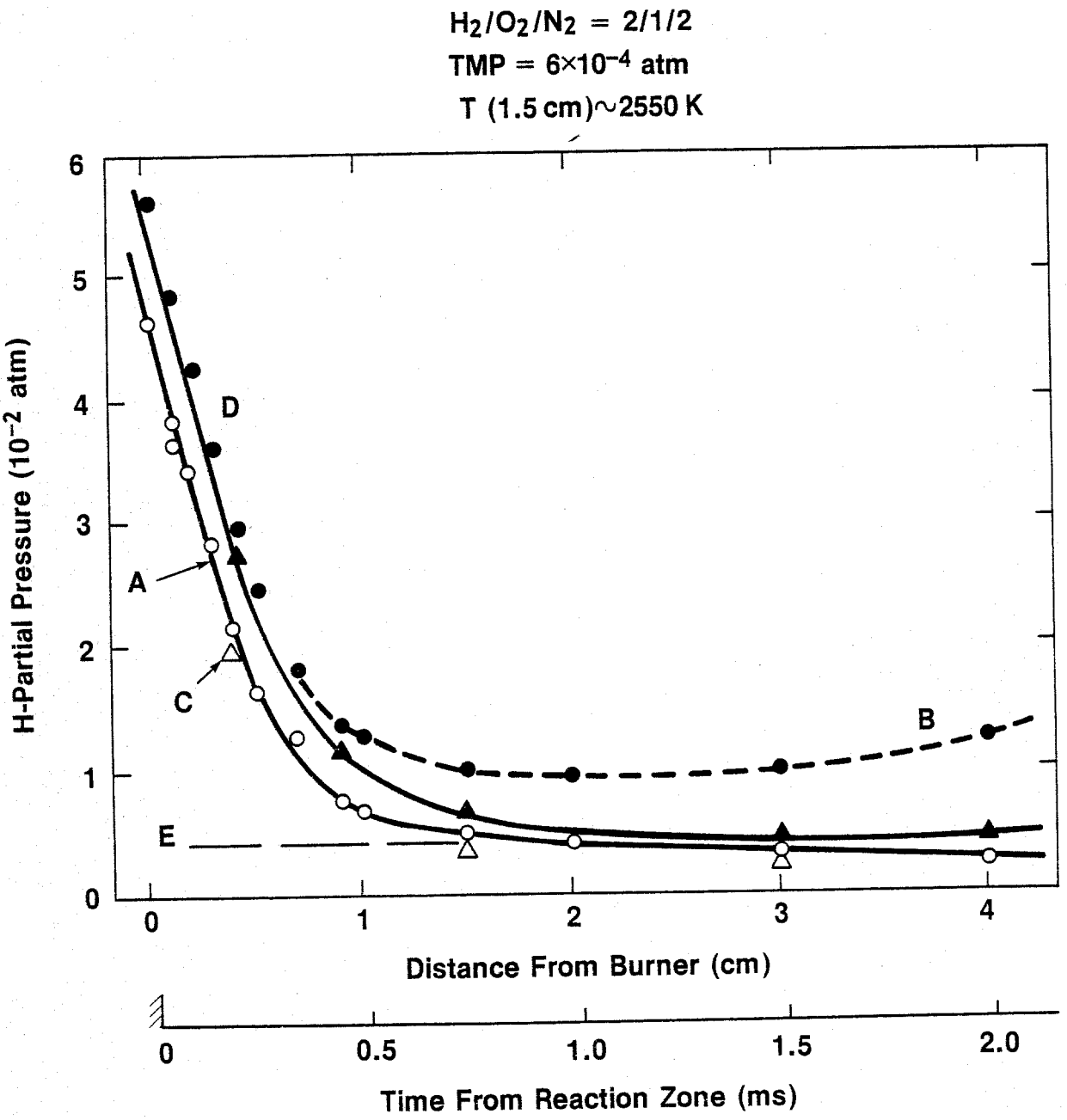
$H_2/O_2/N_2$ = 2/1/2
TMP = 6×10^{-4} atm
T (1.5 cm)~2550 K
H-Partial Pressure (10^{-2} atm)
0
1
2
3
4
5
6
A
B
C
D
E
0
1
2
3
4
Distance From Burner (cm)
0
0.5
1.0
1.5
2.0
Time From Reaction Zone (ms)

Figure 10

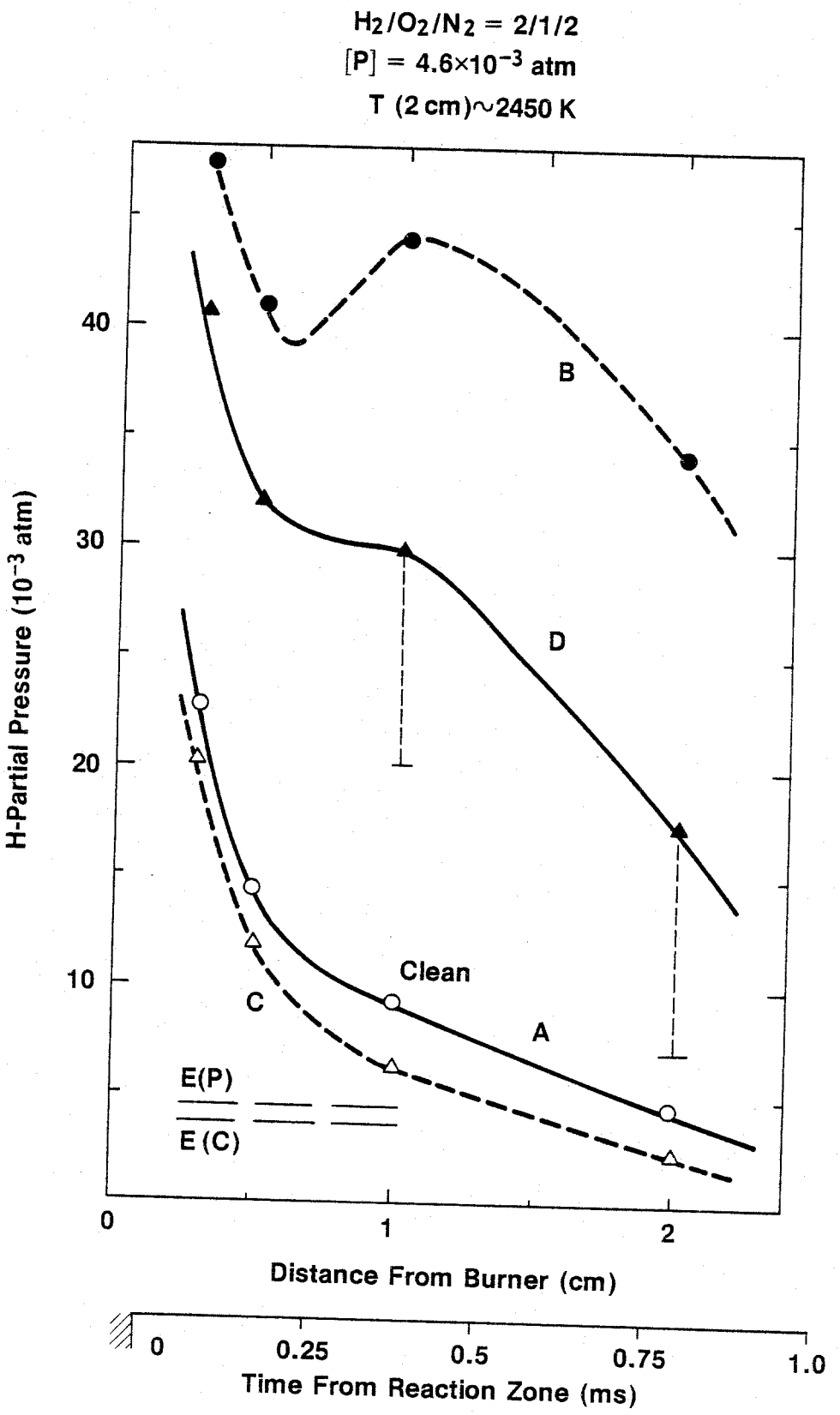
$H_2/O_2/N_2$ = 2/1/2
[P] = 4.6×10^{-3} atm
T (2 cm)~2450 K
H-Partial Pressure (10^{-3} atm)
40
30
20
10
B
D
Clean
C
A
E(P)
E (C)
0
1
2
Distance From Burner (cm)
0
0.25
0.5
0.75
1.0
Time From Reaction Zone (ms)

Figure 11

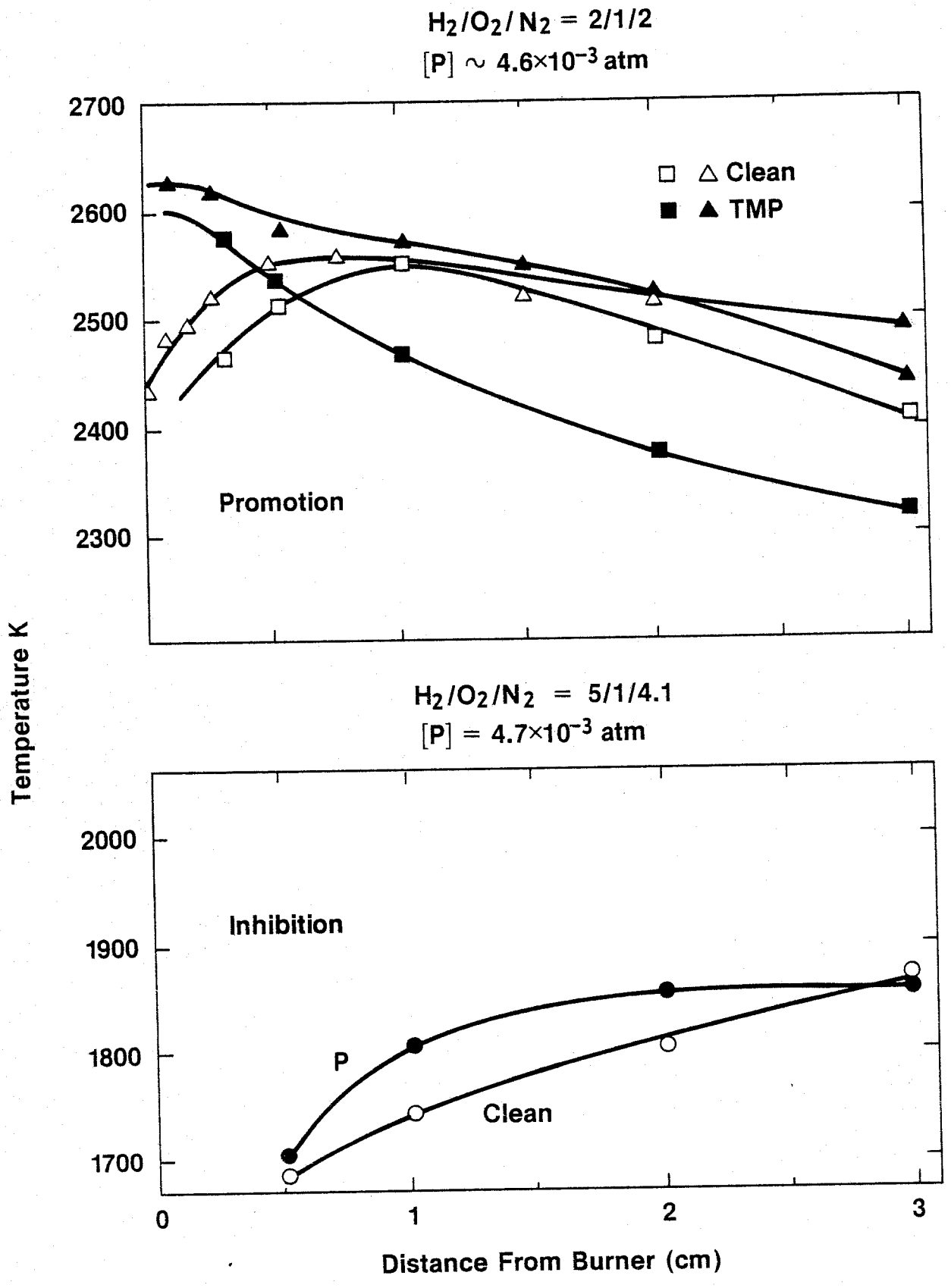
$H_2/O_2/N_2$ = 2/1/2
[P] ~ 4.6×10^{-3} atm
2700
2600
2500
2400
2300
Clean
TMP
Promotion
$H_2/O_2/N_2$ = 5/1/4.1
[P] = 4.7×10^{-3} atm
2000
1900
1800
1700
Inhibition
P
Clean
0
1
2
3
Temperature K
Distance From Burner (cm)

Figure 12

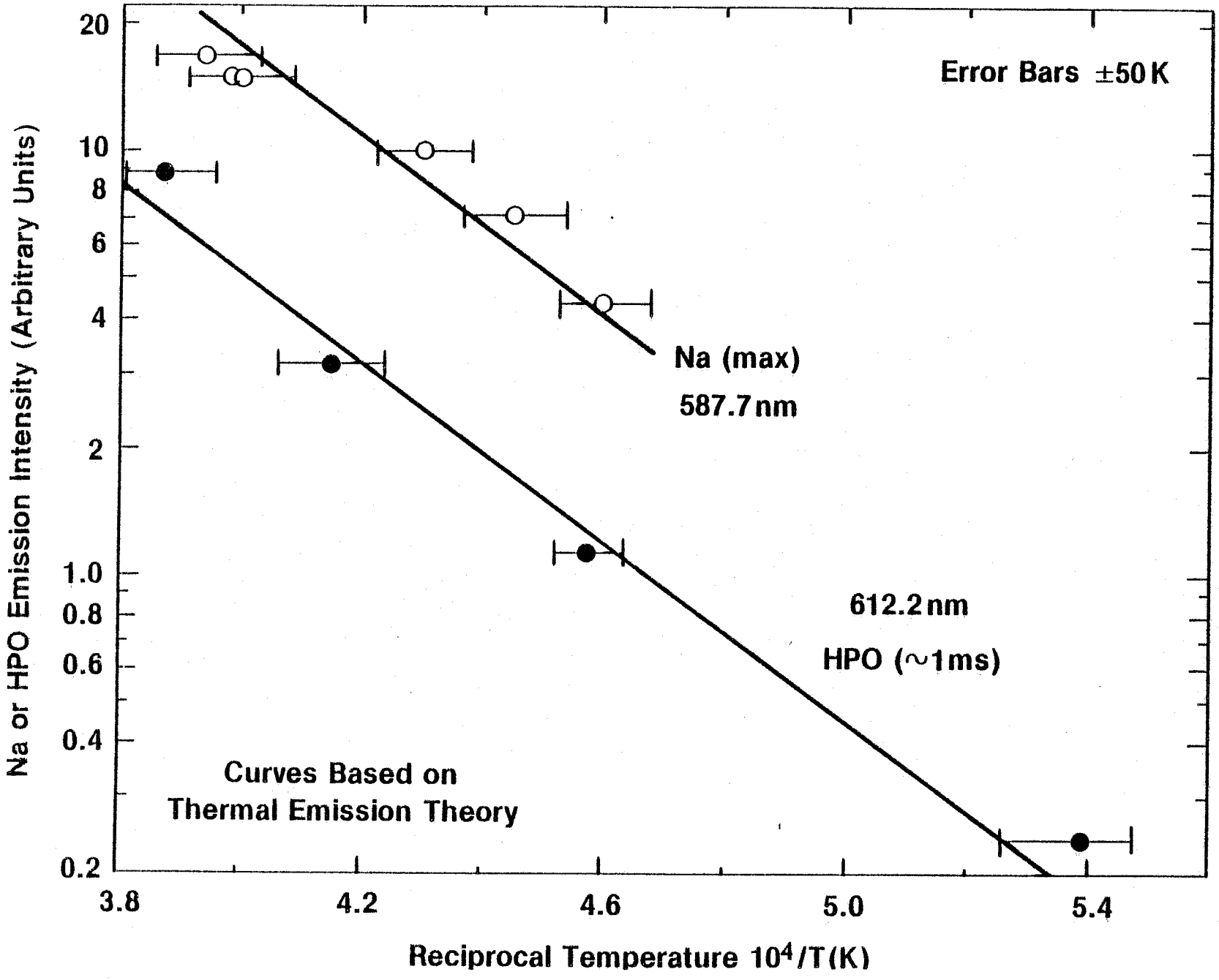
Error Bars ±50 K
Na (max)
587.7 nm
612.2 nm
HPO (~1 ms)
Curves Based on
Thermal Emission Theory
Na or HPO Emission Intensity (Arbitrary Units)
20
10
8
6
4
2
1.0
0.8
0.6
0.4
0.2
3.8
4.2
4.6
5.0
5.4
Reciprocal Temperature 10⁴/T(K)

Figure 13

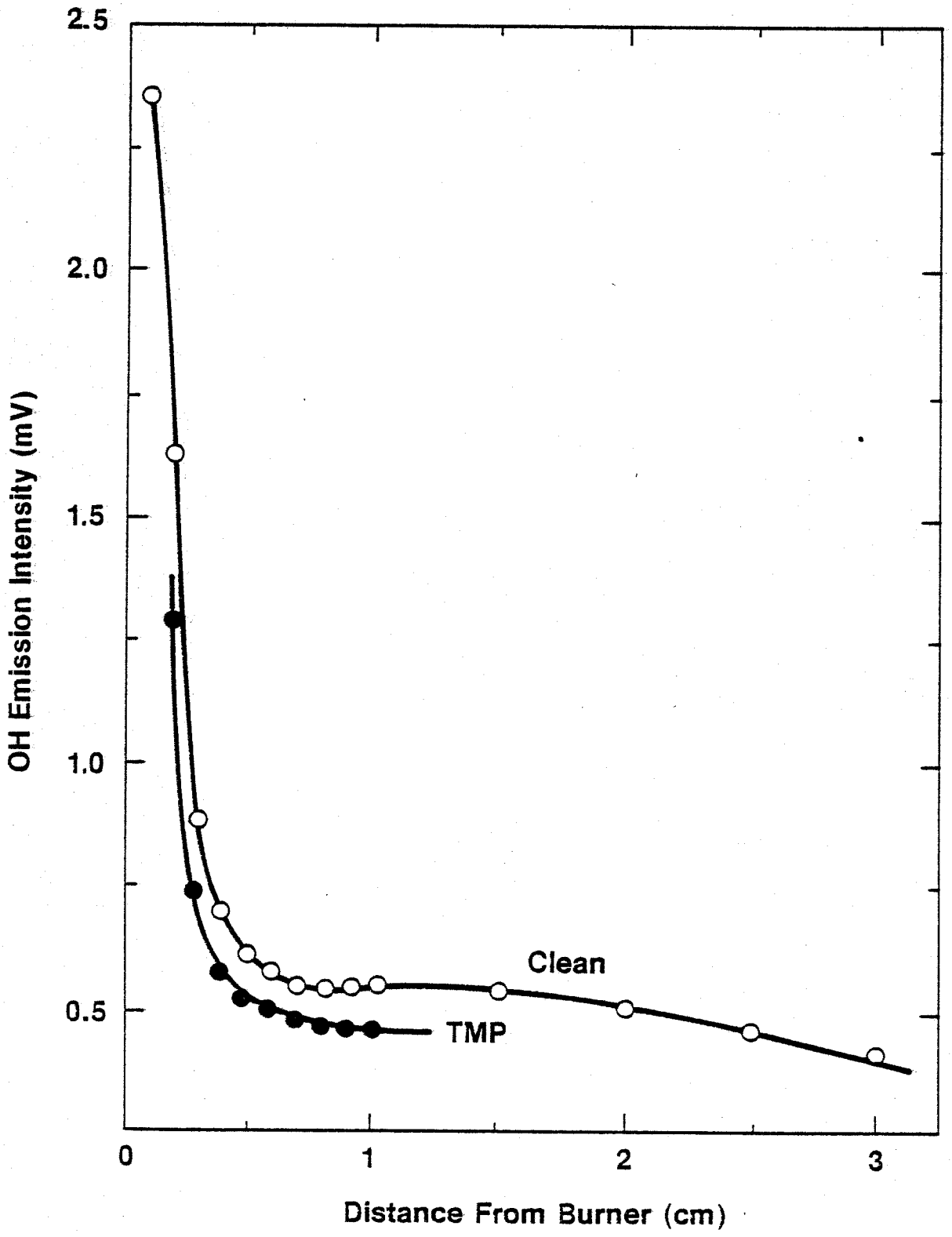
$H_2/O_2/N_2 = 3.7/1/3$
$[P] = 4.6\times10^{-3}$ atm
T(3 cm)~ 2200 K
OH Emission Intensity (mV)
2.5
2.0
1.5
1.0
0.5
0
1
2
3
Distance From Burner (cm)
Clean
TMP

Figure 14

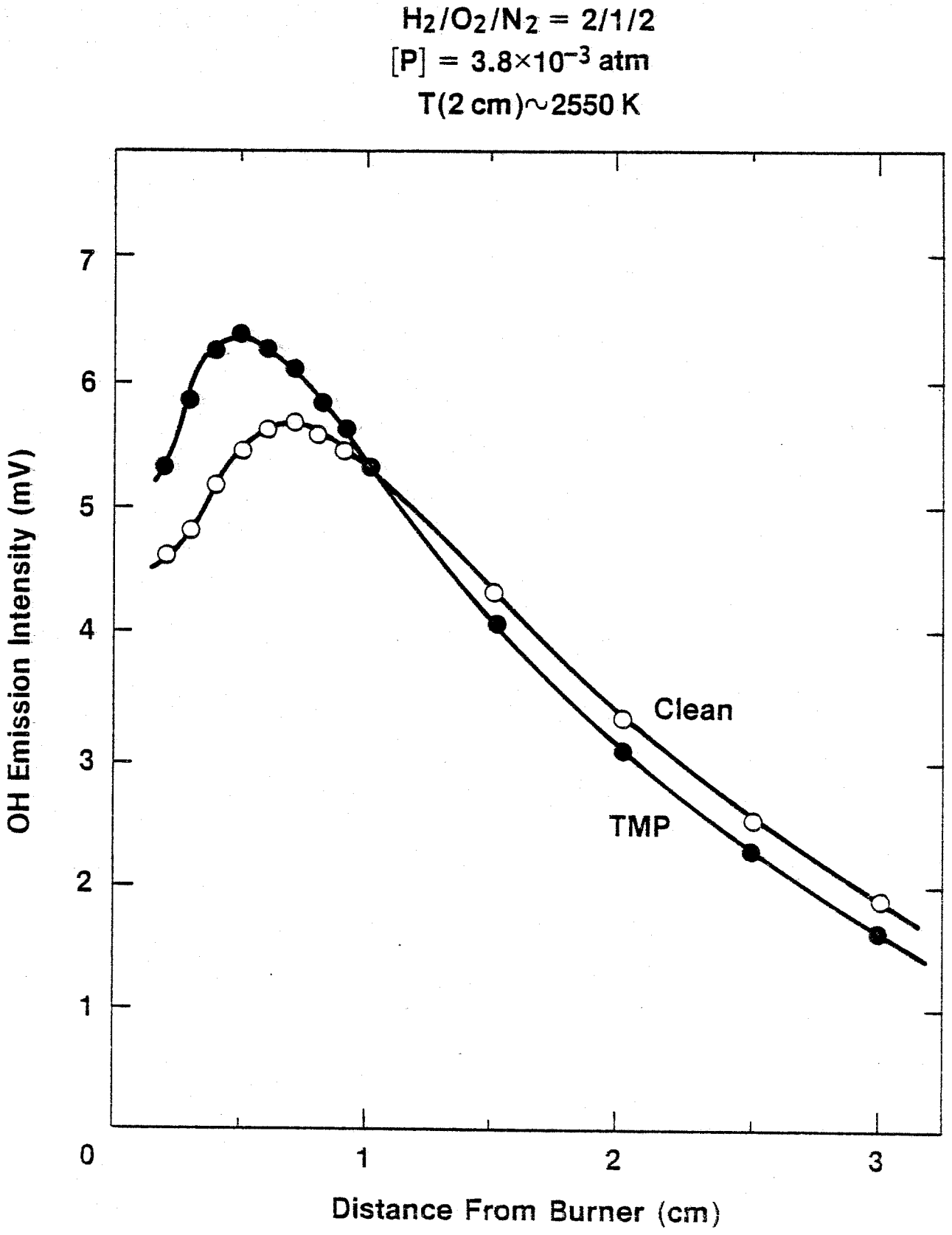
$H_2/O_2/N_2 = 2/1/2$
$[P] = 3.8\times10^{-3}$ atm
T(2 cm)~2550 K
OH Emission Intensity (mV)
0
1
2
3
4
5
6
7
1
2
3
Distance From Burner (cm)
Clean
TMP

Figure 15

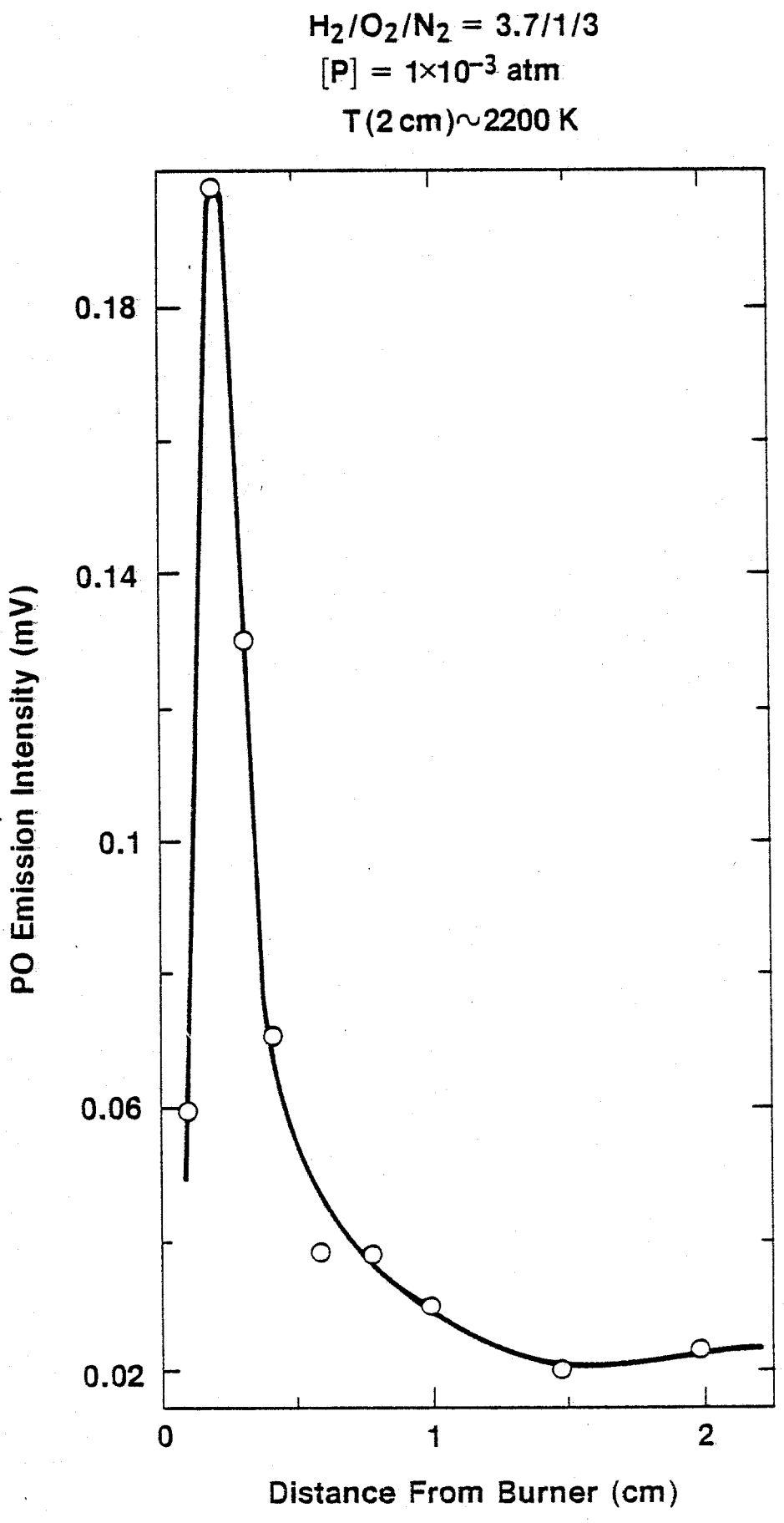
$H_2/O_2/N_2$ = 3.7/1/3
[P] = 1×10^{-3} atm
T(2 cm)~2200 K
PO Emission Intensity (mV)
0.18
0.14
0.1
0.06
0.02
0
1
2
Distance From Burner (cm)

Figure 16

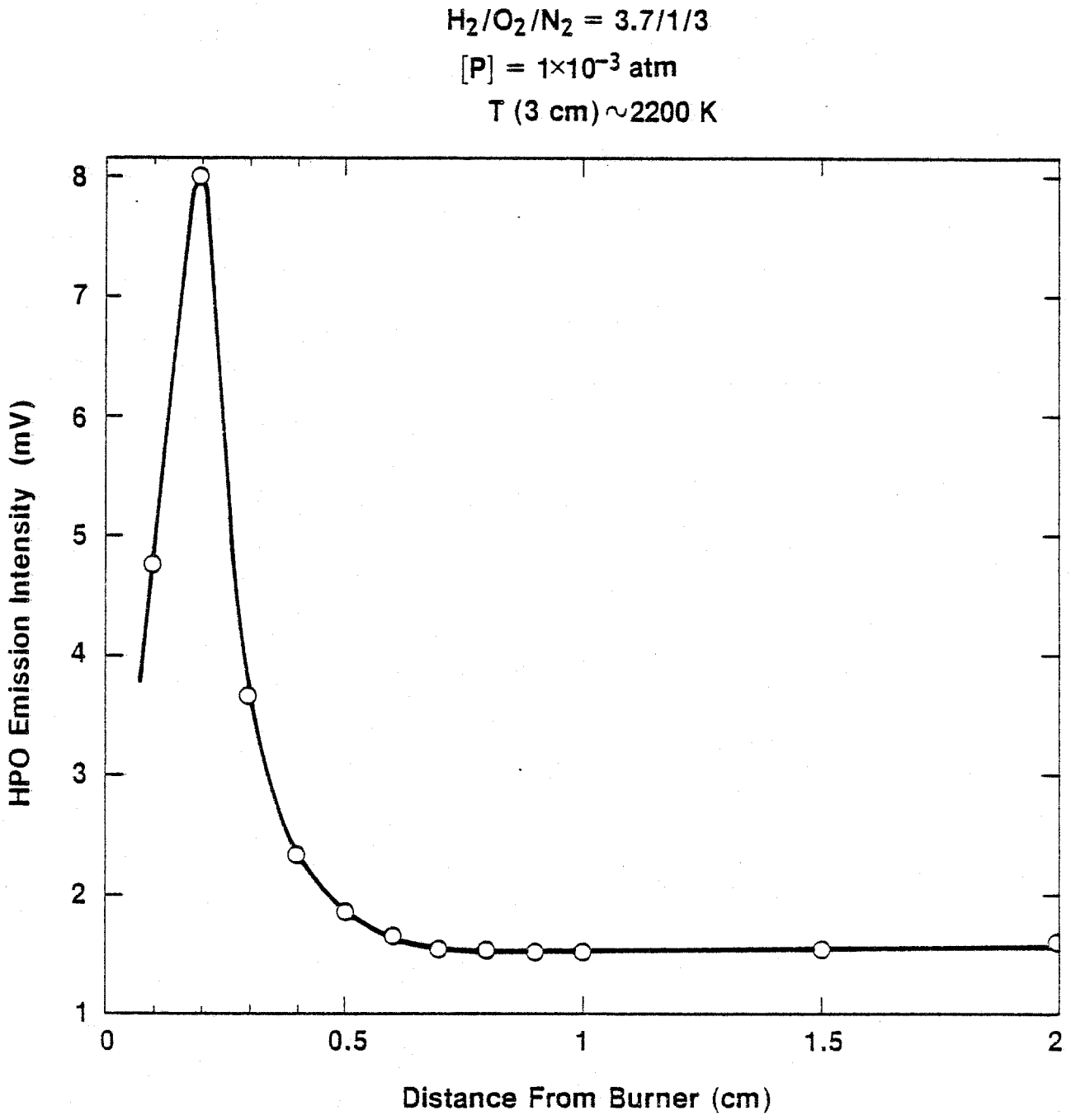
$H_2/O_2/N_2$ = 3.7/1/3
[P] = 1×10^{-3} atm
T (3 cm) ~2200 K
HPO Emission Intensity (mV)
8
7
6
5
4
3
2
1
0
0.5
1
1.5
2
Distance From Burner (cm)

Figure 17

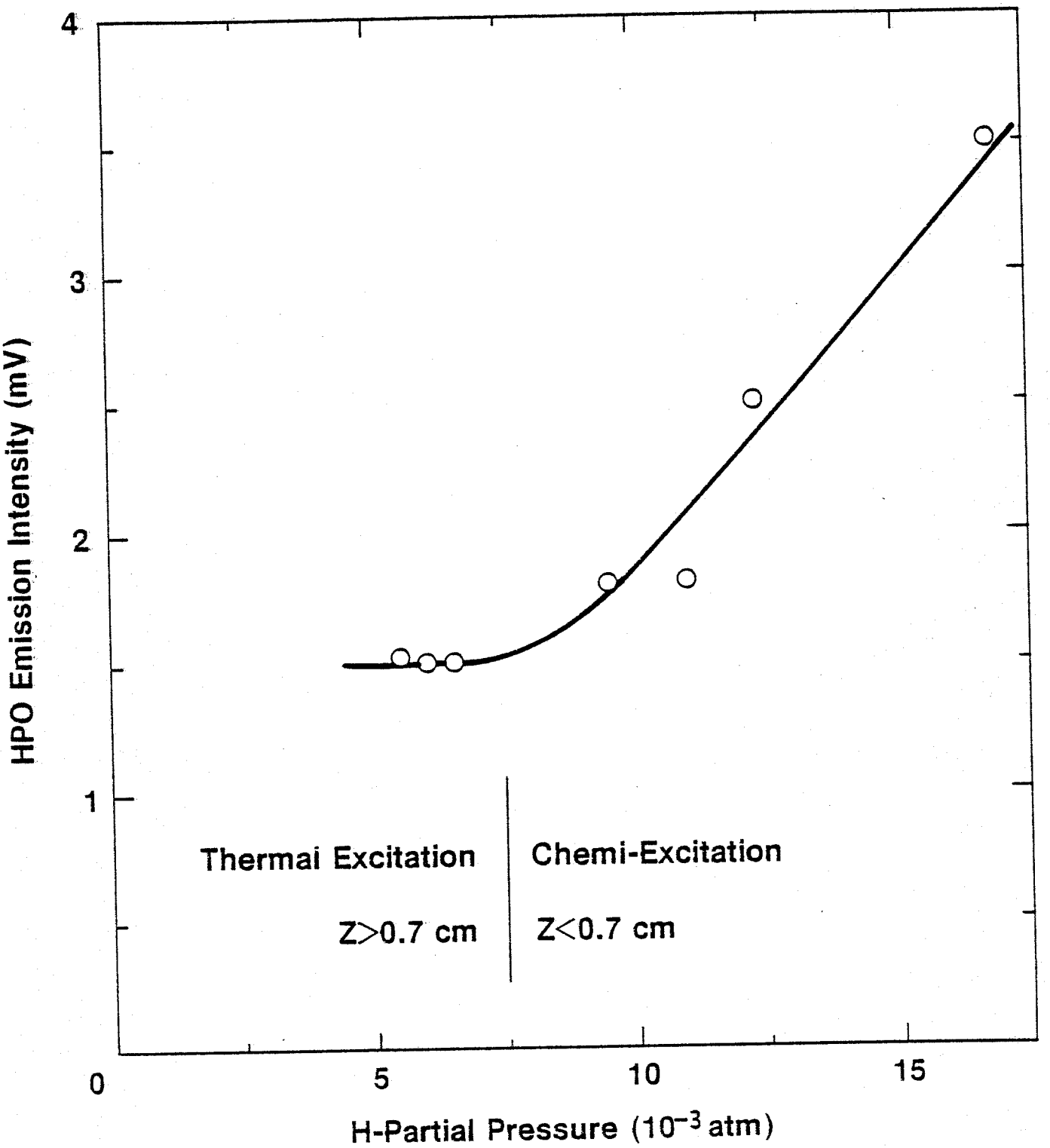
$H_2/O_2/N_2 = 3.7/1/3$
$[P] = 1\times10^{-3}$ atm
T(3 cm)~2200 K
HPO Emission Intensity (mV)
H-Partial Pressure (10^{-3} atm)
Thermal Excitation
Z>0.7 cm
Chemi-Excitation
Z<0.7 cm
0
1
2
3
4
5
10
15

Figure 18

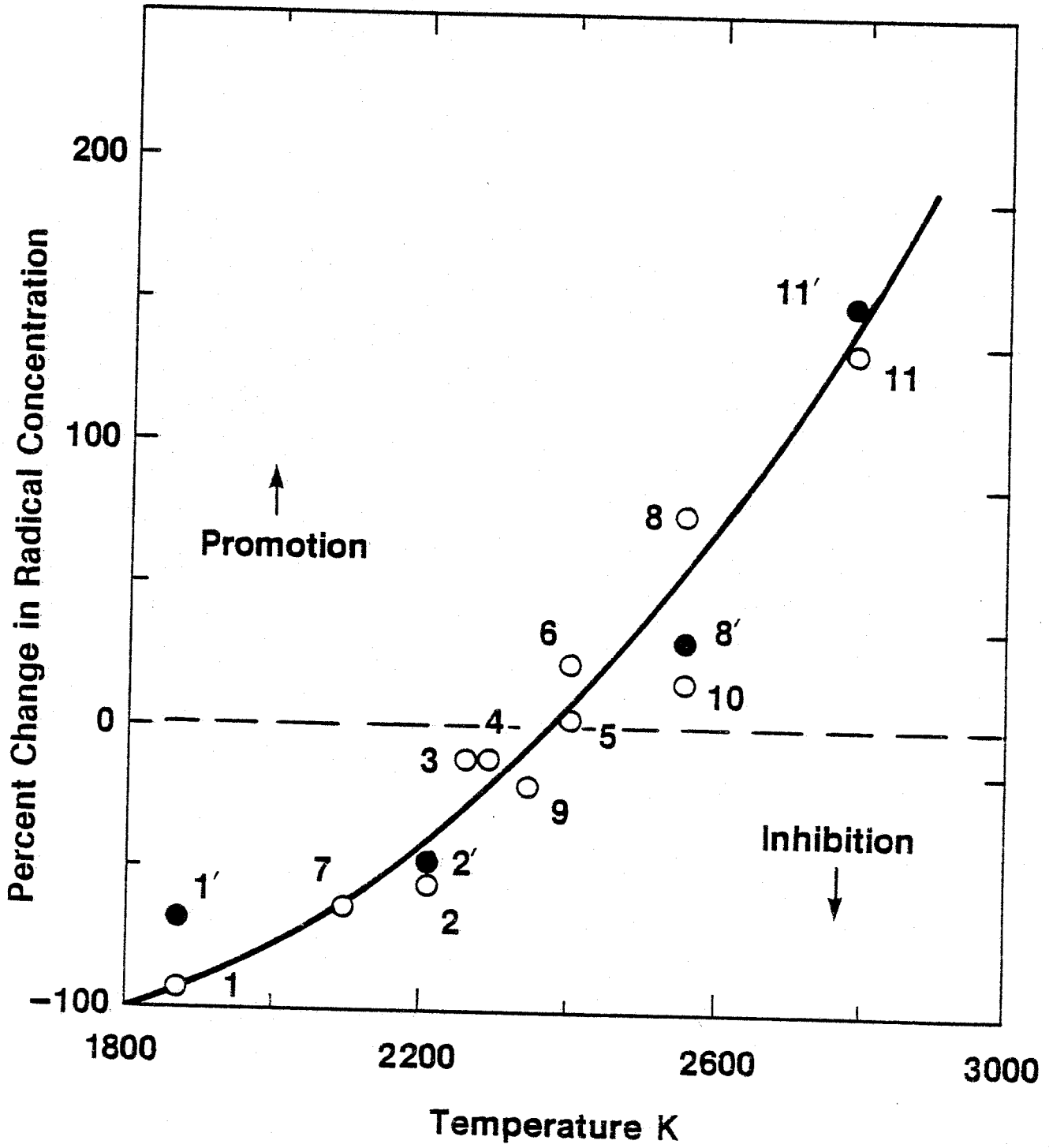
200
100
0
−100
1800
2200
2600
3000
Percent Change in Radical Concentration
Temperature K
Promotion
Inhibition
1′
1
2′
2
3
4
5
6
7
8
8′
9
10
11′
11

Figure 19

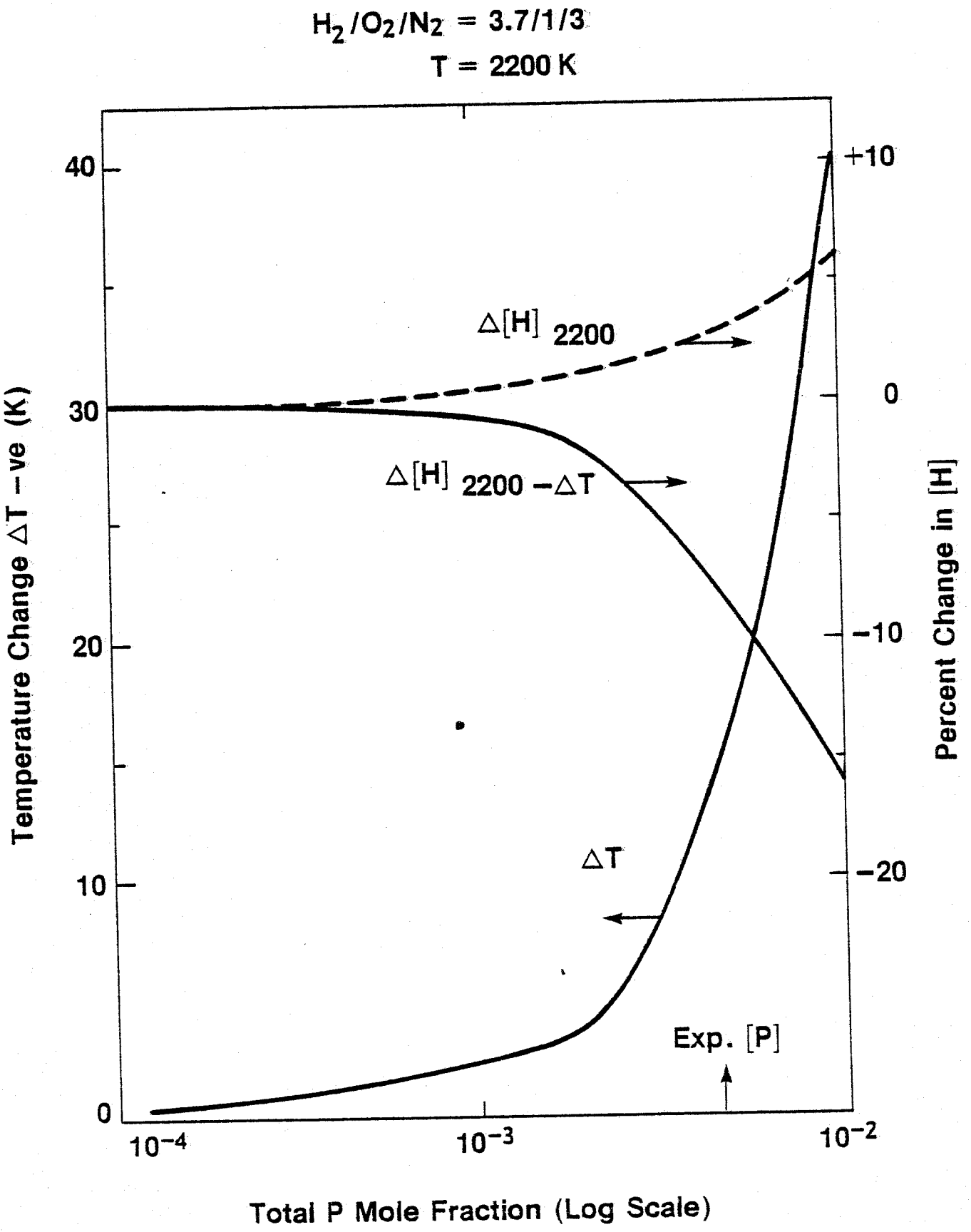
$H_2/O_2/N_2$ = 3.7/1/3
T = 2200 K
40
30
20
10
0
+10
0
−10
−20
Δ[H] 2200
Δ[H] 2200 −ΔT
ΔT
Exp. [P]
10^{-4}
10^{-3}
10^{-2}
Temperature Change ΔT −ve (K)
Percent Change in [H]
Total P Mole Fraction (Log Scale)

Figure 20

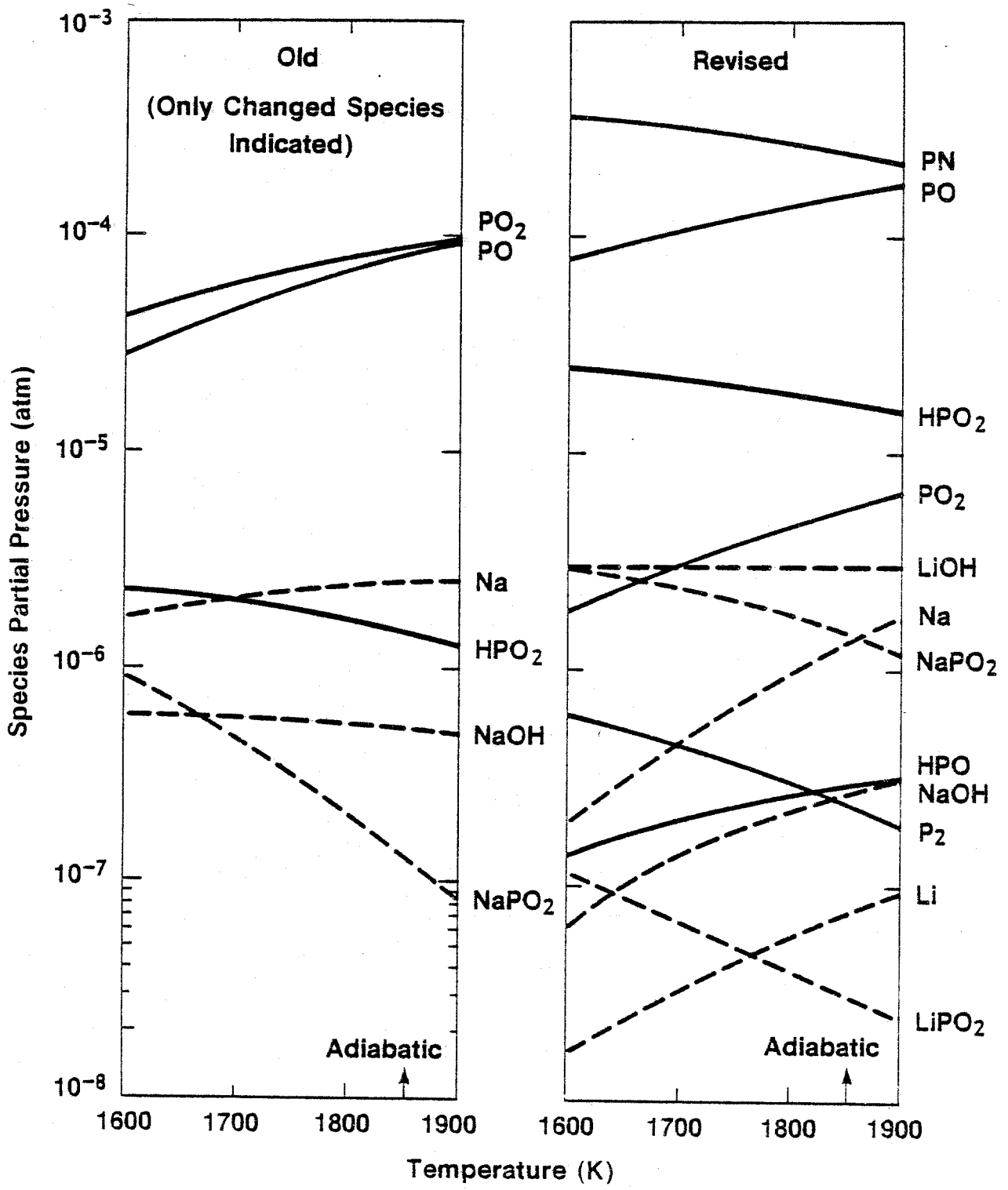
$H_2/O_2/N_2$ = 5/1/4.1
[P] = 4.4×10^{-4} atm
A [Li], [Na] = 3×10^{-6} atm B
Old
(Only Changed Species Indicated)
Revised
Species Partial Pressure (atm)
10^{-3}
10^{-4}
10^{-5}
10^{-6}
10^{-7}
10^{-8}
PO_2
PO
Na
HPO_2
NaOH
$NaPO_2$
Adiabatic
PN
PO
HPO_2
PO_2
LiOH
Na
$NaPO_2$
HPO
NaOH
P_2
Li
$LiPO_2$
Adiabatic
1600
1700
1800
1900
Temperature (K)

Figure 21

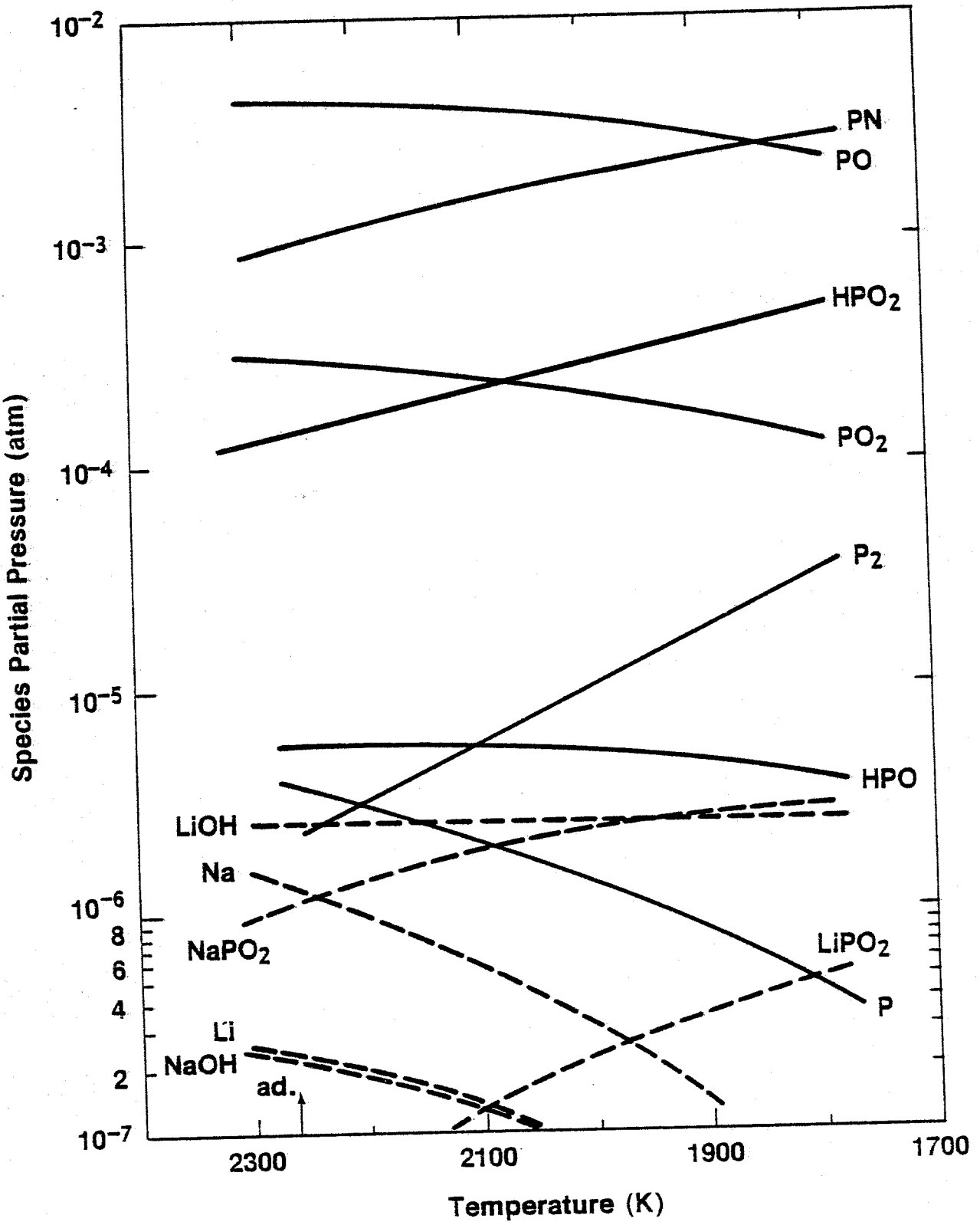
$H_2/O_2/N_2$ = 3.7/1/3
[P] = 5.4×10⁻³ atm
[Li], [Na] = 2.8×10⁻⁶ atm
Species Partial Pressure (atm)
10⁻²
10⁻³
10⁻⁴
10⁻⁵
10⁻⁶
8
6
4
2
10⁻⁷
PN
PO
HPO₂
PO₂
P₂
HPO
LiOH
Na
NaPO₂
LiPO₂
P
Li
NaOH
ad.
2300
2100
1900
1700
Temperature (K)

Figure 22

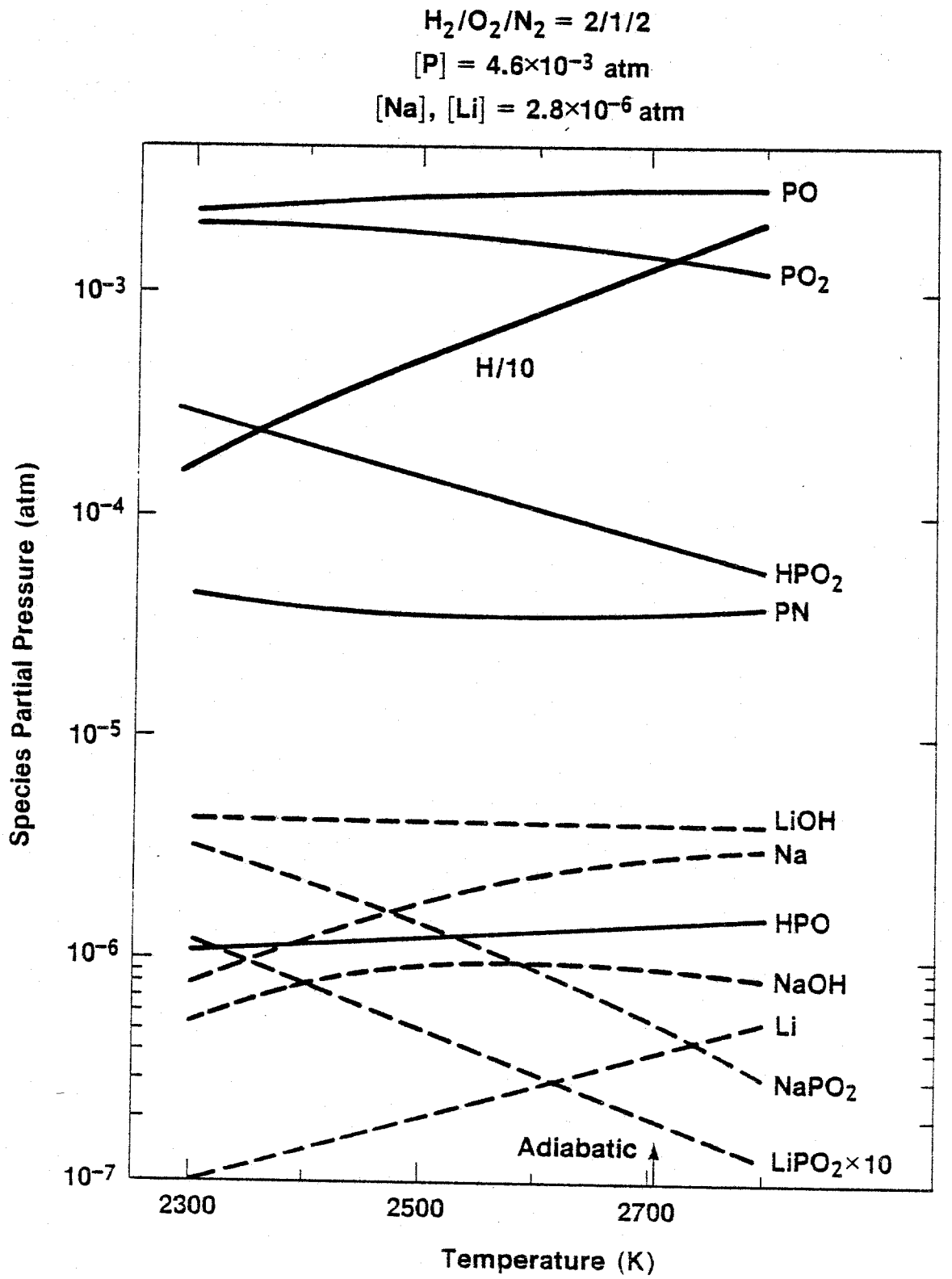
$H_2/O_2/N_2$ = 2/1/2
[P] = 4.6×10⁻³ atm
[Na], [Li] = 2.8×10⁻⁶ atm
PO
PO2
H/10
HPO2
PN
LiOH
Na
HPO
NaOH
Li
NaPO2
LiPO2×10
Adiabatic
10⁻³
10⁻⁴
10⁻⁵
10⁻⁶
10⁻⁷
2300
2500
2700
Species Partial Pressure (atm)
Temperature (K)

Figure 23

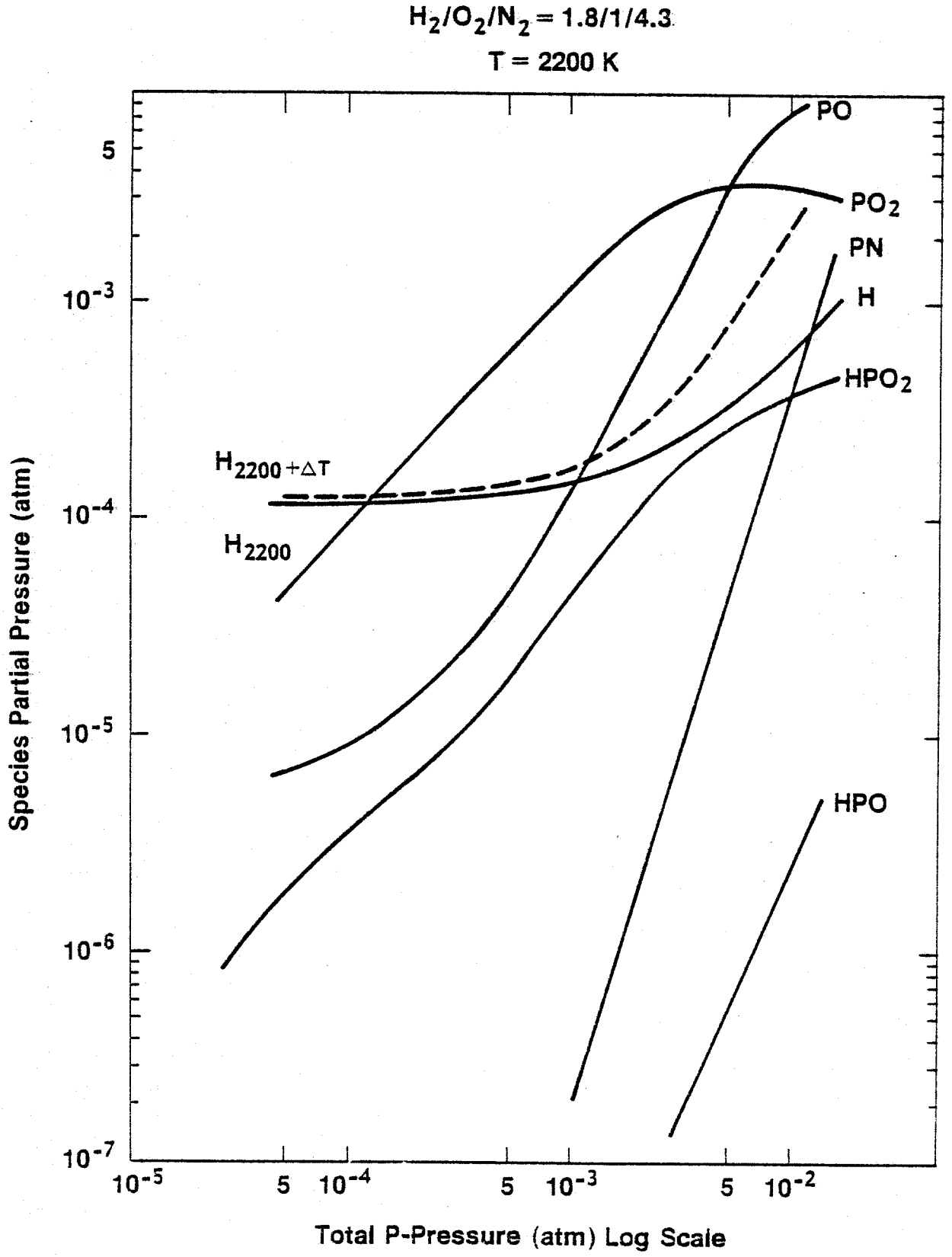
$H_2/O_2/N_2 = 1.8/1/4.3$
T = 2200 K
PO
PO_2
PN
H
HPO_2
$H_{2200+\Delta T}$
H_{2200}
HPO
Species Partial Pressure (atm)
5
10^{-3}
10^{-4}
10^{-5}
10^{-6}
10^{-7}
10^{-5}
5 10^{-4}
5 10^{-3}
5 10^{-2}
Total P-Pressure (atm) Log Scale

Figure 24

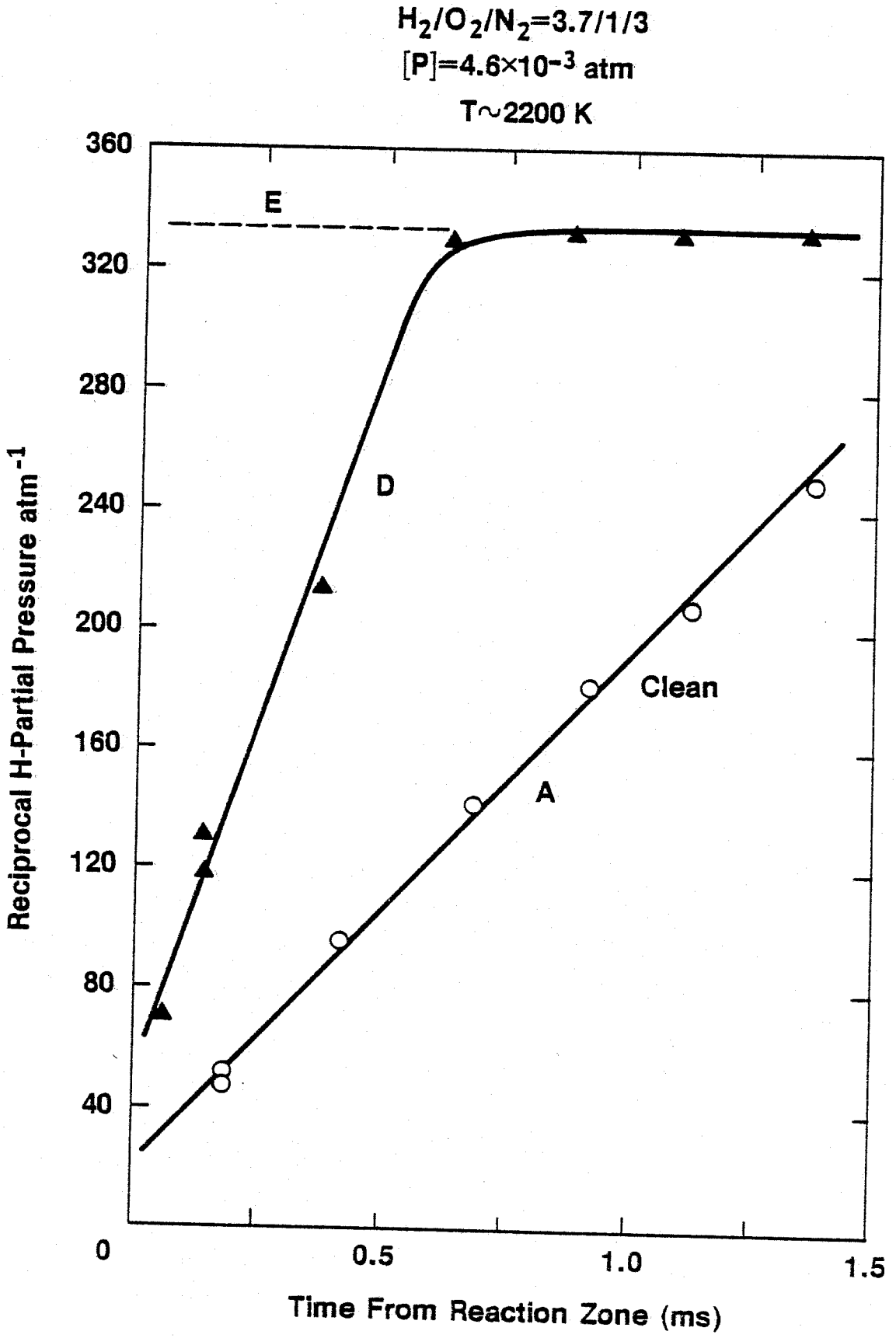
$H_2/O_2/N_2$=3.7/1/3
[P]=4.6×10^{-3} atm
T~2200 K
360
320
280
240
200
160
120
80
40
0
E
D
Clean
A
Reciprocal H-Partial Pressure atm^{-1}
0.5
1.0
1.5
Time From Reaction Zone (ms)

Figure 25

Appendix A

National Bureau of Standards Special Publication 561, Proceedings of the 10th Materials Research Symposium on Characterization of High Temperature Vapors and Gases held at NBS, Gaithersburg, Maryland, September 18-22, 1978. Issued October 1979.

A Comparison of Spectroscopic Flame Temperature Measurements: Na-D Line Reversal, Rotational and Vibrational Raman, and OH Absorption

M. C. Drake,[1] L. H. Grabner, and J. W. Hastie[2]
National Bureau of Standards
Washington, D.C. 20234

Different spectroscopic methods are used for the measurement of flame temperature. This report compares measurement of temperature profiles for atmospheric premixed $H_2/O_2/N_2$ laminar flames using the methods of: (1) Raman scattering (N_2, vibrational and rotational temperatures), (2) line reversal (D-line of Na, electronic temperature), and (3) line ratio (OH, rotational temperature). Two separate burner designs are considered. To obtain the most accurate comparison possible, all measurements were made with the same burners and auxiliary gas-feed system. The theory for each technique is summarized and the sensitivity, accuracy, and convenience are compared. Necessary corrections are discussed. In general, the results indicate very good agreement (better than 98 percent) between the various methods for certain combinations of flame composition and burner type.

1. Introduction

1.1 Status of flame temperature measurement

Temperature, and its spatial and temporal distribution, is perhaps the most important fundamental quantity for characterization of a high temperature vapor or gaseous system. This is especially the case for atmospheric pressure flames, where both laboratory and industrial systems are included. For instance, temperature can be used as a rating parameter for comparing the effectiveness of various control measures in combustion efficiency and flame inhibition [1][3]. More commonly, temperature is used in conjunction with species concentration data to define the kinetic or thermodynamic state of the flame [2,3].

The recent development of computer-based methods of temperature calculation for both equilibrium [4] and non-equilibrium [5] flame systems, together with the availability of an

---

[1] NRC-NBS Doctoral Research Associate, present address, General Electric Co., Research and Development Center, P. O. Box 8, Schenectady, New York.

[2] Authors listed alphabetically.

[3] Figures in brackets indicate the literature references at the end of this paper.

adequate basic thermodynamic [6] and chemical kinetic data base [7,8], particularly for $H_2/O_2/N_2$, has added a new dimension to temperature determination. Accurate experimental flame temperature profiles are now needed to validate these computer based models of flame processes.

On the experimental side, the use of different burners and flames by most workers is a serious impediment to interlaboratory transfer of data. It is now apparent that combustion standards are needed, particularly in the areas of burner design and flame selection. The present study is a mere beginning in this direction.

In addition to these difficulties, little is known about the accuracy of various temperature measurement methods. With the continuing development, in recent years, of novel temperature measurement techniques, e.g., Raman scattering, Coherent Antistokes Raman Spectroscopy (CARS), and two line fluorescence, the need for accurate comparison data by established techniques such as line-reversal for validation of these methods is further indicated. Evidence of this continued development of new or modified flame temperature measurement techniques is provided by the chapters presented elsewhere in this volume on the methods:

- Coherent Antistokes Raman Spectroscopy [9,10],
- Raman [11,12],
- optoacoustic [13],
- two line fluorescence [14], and
- modified D-line reversal [15].

An obvious first candidate for a standard burner-flame system is the Padley-Sugden type burner [16] - $H_2/O_2/N_2$ flame combination. Many workers have used this combination over the past twenty years or so (e.g., see ref. [17]). In practically all cases the Na-D line reversal method was used for temperature measurement, and good interlaboratory agreement obtained. Much basic thermodynamic and kinetic data for high temperature inorganic species is based on these temperature results [17]. The present study extends these earlier investigations by including other optical temperature measurement methods (see Section 1.3), and different burner geometries.

1.2 Thermal nature of flames

The thermal nature of flames, that is, the distribution of combustion energy in the form of kinetic or translational energy, internal, and chemical energy, is well understood in a broad sense [17]. For atmospheric pressure flames, these degrees of freedom are usually thermalized rapidly with the internal energy states achieving a Boltzmann population distribution. However, for such flames the relaxation times associated with the redistribution of excess energy arising from the exothermic combustion process are such that regions of disequilibrium may exist, particularly near the primary reaction zone. The location and extent of this disequilibrium varies according to the flame type, burner, gas flow rate, temperature and pressure. Well known examples of the occurrence of nonequilibrium

state-distributions include certain OH rotational energy levels and Na-D line chemiluminescence near the reaction zone (<1ms)[4] of atmospheric premixed flames. Under turbulant conditions these effects may be even more significant [18]. Chemical (concentration) disequilibrium for the radicals H, OH, and O persists for times of several ms (or a few cm distance from the reaction zone) or longer, depending largely on the flame temperature.

Usually there is insufficient quantitative data available on the various flame relaxation processes, to predict a priori when or where a particular flame system will achieve a thermalized condition with respect to each, or all, of the degrees of freedom. Hence, if a spectroscopic temperature measurement is to be used in a chemical kinetic or thermodynamic sense, the thermal condition of the internal energy needs to be established by empirical means.

Usually, the time required to achieve a thermal energy distribution increases according to the sequence:

translation < rotational < vibrational < electronic < chemical.

Generally, if one can establish thermalization for one of these energy states then higher (faster) members can be assumed to follow the same condition. Also, if the state populations are thermally distributed then measurement of these populations can be used as a basis for spectroscopic temperature measurements.

Temperature, so obtained, represents only the local thermodynamic equilibrium (LTE) condition of those states monitored. Thus, such a temperature does not necessarily correlate with the thermodynamic equilibrium temperature for the total system, where all degrees of freedom are included. If an LTE temperature is to be used to characterize a particular kinetic or thermodynamic process, all the states involved must satisfy the LTE condition.

As flames are not isolated systems, due to burner and atmospheric influences, they can only approach equilibrium and it is therefore useful to retain the term LTE when referring to flame temperature data. Also, in the absence of general information about the thermal nature of all the states present, we should qualify temperature statements with respect to the states involved in the measurement of temperature. Thus, terms such as rotational, vibrational, and electronic temperature are used, with the understanding that not all rotational states, etc., are included.

1.3 Selection of temperature measurement methods

Following the discussion of Section 1.2, it is clear that a definitive measurement of flame temperature should include direct observation of the relative population distribution for as many degrees of freedom as possible. For practical purposes the states of rotational, vibrational and electronic degrees of freedom are the most accessible. As these three state-types encompass an exceptionally wide range of relaxation times (ca 10^{-8}-10^{-3}s) a demonstration of LTE for each state with the same temperature would indicate that this characteristic temperature is valid for the whole system.

[4] Represents flow time downstream of the reaction zone; the distance equivalent is typically several mm.

Temperature measurement methods covering these three state-types and selected for the present study include:

(1) The Na-D line reversal method, which essentially measures an electronic temperature for the spectroscopic transition $3S_{1/2} - 3P_{3/2}$ at 589.0 nm.

(2) A line ratio method where the relative intensities of the rotational lines of the $A^2\Sigma - X^2\Pi$ electronic transition (306.5 nm band) for OH are measured.

(3) A Raman spectroscopic method using scattering from the vibrational and rotational states of N_2.

Method (1) is an established technique of known accuracy for temperature measurement in post flame regions[5]. However, there are limitations, among which is a possible disturbance of the chemical balance in the flame by the presence of Na. Errors inherent in the line reversal method have been discussed in detail by Snelleman [21].

Method (2) has rarely been used with atmospheric pressure flames and its accuracy is uncertain.

Method (3) is a novel technique developed in recent years [22] and the use of rotational states has only barely begun [23,12].

Each technique has relative merit, depending on the system of interest. For instance, the Raman method can be used throughout the flame whereas methods (1) and (2) are limited to the post reaction zone region[6]. Thus an intercomparison of temperatures obtained from these methods serves both as a test for thermal equilibrium between the various states and as a demonstration of the reliability and accuracy of methods (2) and (3) with respect to (1).

The measured temperatures may also be compared with the calculated adiabatic values, using a well established minimization of free energy multicomponent equilibrium computation procedure [4]. This technique provides an upper limit to the possible measured flame temperature (for constant stoichiometry) and is based on the ideal condition of general thermodynamic equilibrium. That is, all states are in LTE and no heat transfer to, or from, the surroundings occurs. In order that the calculated temperatures be useful, we have used burners where heat losses are small and flame temperatures closely approach the adiabatic values (to within 96 percent).

For convenience we shall refer to temperatures obtained by these four approaches as:

- reversal temperature,
- OH rotational temperature,
- Raman (rotational or vibrational) temperature, and
- adiabatic temperature,

where these first three terms refer only to the actual spectroscopic states involved. A fifth temperature:

- the LTE (local thermodynamic equilibrium) temperature will be referred to when the states involved are believed to be thermalized, i.e., follow a single Boltzmann

---

[5]The long established Na-D line reversal method of temperature measurement continues to find new application, e.g., in propellant gases [19] and in magnetohydrodynamic flame gases [20].

[6]A particularly useful combination is to use Na-D line reversal data for thermocouple correction, thereby permitting a complete temperature profile to be obtained [9,24] with subsequent thermocouple measurements.

population distribution. For cases where LTE is not established, the term:

- pseudo temperature

may be used [25].

2. The Methods

2.1 Na-D line reversal

This method is the oldest optical technique for measuring flame temperature [26]. A recent description may be found in the book of Gaydon and Wolfhard [27] and a critical evaluation is given in references [21] and [28]. Figure 1 shows our particular experimental arrangement. The method is popular because it is rapid, convenient, and requires no data analysis. Upon reversal, the Na-D line temperature is measured directly by a pyrometer. The following discussion of this well known method serves mainly to derive the reversal sensitivity with temperature and to indicate the physical meaning of the reversal temperature.

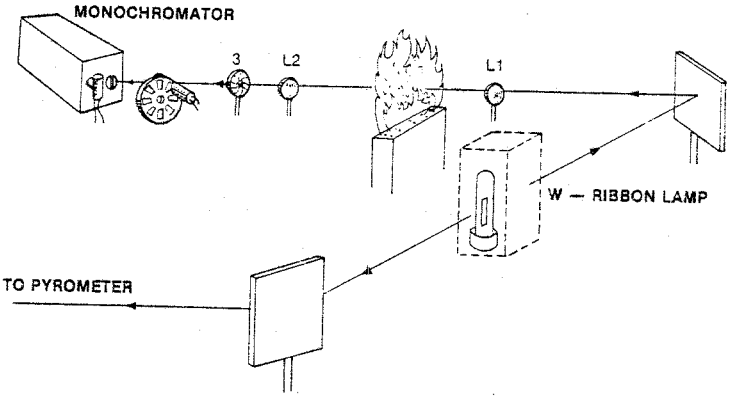

Figure 1. Na-D line reversal apparatus (isometric view). Light from W-ribbon lamp is focused by lens L1 to give an image of the W-ribbon in the flame. A second lens L2 forms an image of both flame and W-ribbon on the monochromator entrance slit. Aperture stop 3, located at the position of image of L1 formed by L2, is adjusted so that the solid angle of the light from flame and reversing source are equal. The optics must be alined so that the image of flame and W-ribbon overlap on the monochromator entrance slit. This is best done photoelectrically. Reversal temperature is pyrometer reading at 655 nm uncorrected for W-emissivity change with λ. This change is generally assumed (and so verified) to be compensated by reflection losses from L1, taken as 5 percent.

The method depends on the spectrally resolved observation of one of the D-lines of a Na colored flame which is simultaneously irradiated in the D-line region by a reversing source, a W-ribbon lamp. In the present study, Na was introduced to the flame in the form of a spray of $NaNO_3$ solution (0.01 molar). Depending on the current carried by the lamp (i.e., color temperature), the D-line (at 589.0 nm) is observed either in absorption or emission, and the lamp current is adjusted to "reverse," i.e., until neither occurs. This is shown by the curves a of figure 2. At reversal, the radiation absorbed by the flame from the reversing source is just compensated by the Na-D line emission from the flame. If the solid angle of the reversing source and flame, as seen by the detector, are equal, then the following relationships apply [29]

$$[1 - A(\lambda,T)]\cdot I(\lambda,T_R) + E(\lambda,T) \gtreqless I(\lambda,T_R) \quad . \tag{1}$$

λ = wavelength.

T = temperature as measured by the pyrometer.

$A(\lambda,T)$ = absorbing power of flame at T and D line λ.

$E(\lambda,T)$ = emissive power of flame at T and D line λ.

$I(\lambda,T_R)$ = radiant flux from reversing source at brightness temperature T_R of D line λ.

In the relationships (1), reflection of the reversing radiation by the flame is neglected. For emission we have (>), for absorption (<), and at reversal (=). At reversal eq. (1) does not directly determine T in terms of T_R. However, if Kirchhoff's law applies,

$$E(\lambda,T) = A(\lambda,T)I(\lambda,T) \quad ,$$

where $I(\lambda,T)$ = radiant flux of a blackbody, and eq. (1) reduces to

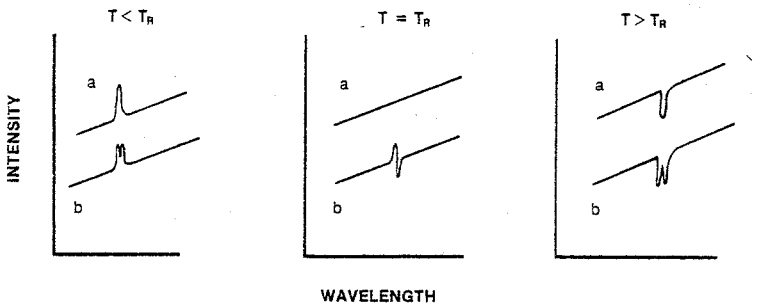

Figure 2. Reversal method. Spectrum of Na-D_1 line (schematic). When brightness temperature of W-ribbon lamp $T<T_R$, $T=T_R$, and $T>T_R$. T_R is the reversal temperature. In series (a) the concentration of Na in the nebulizing solution is 0.01M, in (b) 0.1M. Burner: rectangular with either O(2) or U(4) composition.

$$I(\lambda,T) = I(\lambda,T_R)$$

which is satisfied only if $T = T_R$. T_R is the brightness temperature (pyrometer reading) at the D-line λ and not the temperature of the reversing source (lamp), except if the source is a blackbody, which is usually not the case.

It should be noted that the Na-D line method contains no criterion for local thermodynamic equilibrium (LTE). Even if the line of another element, such as Li, is found to reverse at the same temperature as the Na-D line this condition is necessary but not sufficient that T_R is a LTE temperature. However, it has been our experience that Na-D line emission intensities follow a Boltzmann distribution with temperature and with the correct energy for thermal excitation to the $3P_{3/2}$ level. This has been observed for a large number of $H_2/O_2/N_2$ flames over the temperature range 1800-2500 K and at distances of ~10-30 mm from the reaction zone and suggests LTE for the internal degrees of freedom present.

With the reasonable assumption that Kirchhoff's law applies here, a temperature sensitivity can be defined. Re-arranging relationships (1):

$$I(\lambda,T_R) + A(\lambda,T)[I(\lambda,T) - I(\lambda,T_R)] \gtrless I(\lambda,T_R) \quad .$$

Close to reversal, the expression in the square brackets is

$$\left[\frac{dI(\lambda,T)}{dT}\right]_{T_R} dT, \text{ where } dT = T-T_R \quad . \qquad (2)$$

We shall define the derivative as the temperature sensitivity. $I(\lambda,T)$ is Planck's function. The value of the derivative as a function of T is tabulated in reference [30]. A sensitivity plot for the temperature range of interest to the present study is given in figure 3. It should also be noted that the signal increases inversely with the spectral slit width of the monochromator until this is equal to the Doppler width of the Na-D line (~0.005 nm at 2000 K). This is because the integrated absorption is invariant with spectral slit width [31,32]. Errors in the method of line-reversal have been extensively discussed by Snelleman [21].

Finally, we wish to call attention to the physical significance of T_R measured by the reversal method. Kohn [33] has shown that

$$\frac{N_m}{N_n} = \frac{g_m}{g_n} \exp(-h\nu/kT_R^{nm}) \quad ,$$

where g_m and g_n are the degeneracy of the states involved in the transition $h\nu$, with populations N_m and N_n. The superscript nm is affixed to T_R, to emphasize that, in general, T_R depends on the transition except for conditions of LTE.

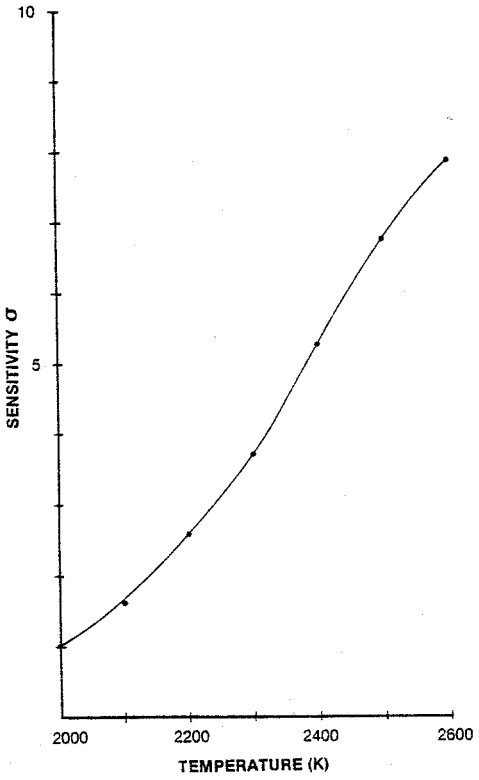

Figure 3. Temperature sensitivity of reversal method defined by equation (2) $dI(\lambda,T)/dT$ vs T at λ = 589 nm. The temperature sensitivity $\sigma = \frac{dI}{dT} / (\frac{dI}{dT})_{T_o}$ is normalized to T_o = 2000 K.

In applying the Na-D line reversal method, one has to empirically determine the appropriate range of flame Na concentration where reversal occurs [24]. Typical D-line spectra are given in figure 2 where the effects of too great a Na concentration are indicated (curves b). In the present study the temperature sensitivity of the reversal was within several Kelvins. Reproducibility was limited by the human eye response to the pyrometer, which was typically in the range 5-10 K.

2.2 OH-rotational line ratio

2.2.1 Method

A schematic of the apparatus used to obtain OH-absorption spectra, and hence, flame temperatures, is given in figure 4. Figure 5 shows a typical OH absorption spectrum in the region of 307-309 nm which is a particularly useful region for temperature measurements, as will be discussed in Section 4. The general theory of the method is as follows.

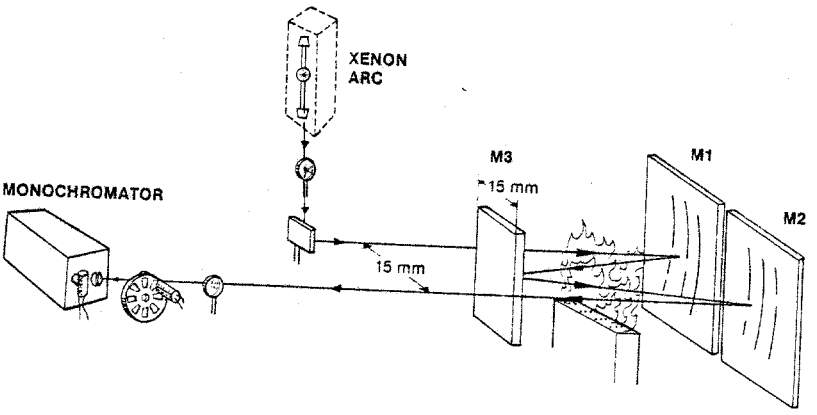

Figure 4. Apparatus for OH absorption measurements (isometric view). White multi-reflection system consists of three concave mirrors each of focal length f = 22.9 cm. M1 and M2 are separated by distance 2f from M3 which is cut to 15 mm width to minimize beam spread through flame. Xe-arc light is focused onto M3. The number of traversals is changed by adjustment of the dihedral angle between M1 and M2 from 4, shown in the figure, to 8, or 12, or any multiple of 4. Two traversals use only M2 and M3. For a single traversal the White system cannot be used, and Xe source-lens-flame-lens-monochromator are set up collinearly.

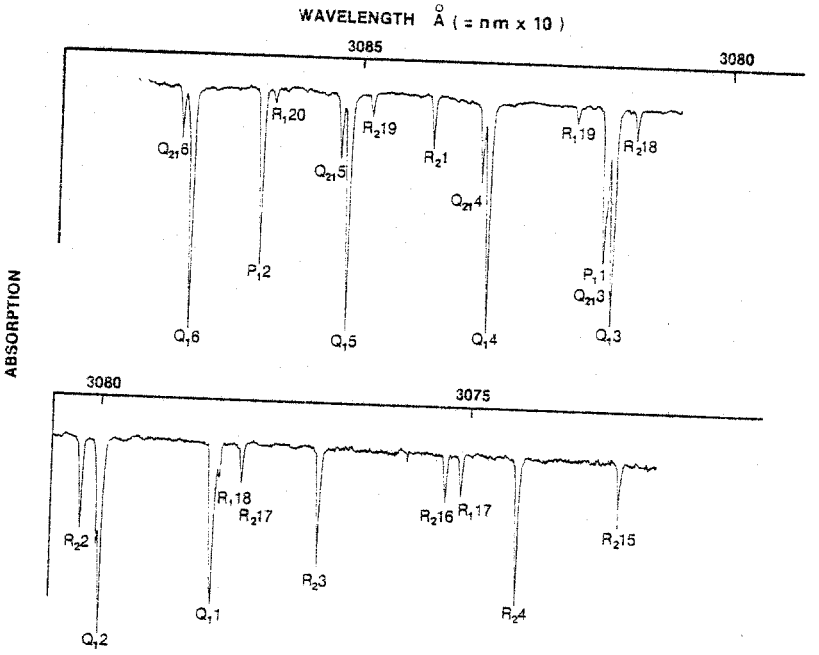

Figure 5. OH rotational absorption spectrum. Lines are identified by standard spectroscopic notation. For an atlas, see reference [34]. For $R_2 4$ line, $I_{abs} = \left[(I_\nu^o - I_\nu)/I_\nu^o\right]_{peak} = 0.54$. Rectangular burner, O(2) composition $H_2/O_2/N_2 = 3.4/1/2$, and two passes of Xe-arc radiation through flame.

In this method, the intensity of two lines is measured in absorption, although emission can be used in some instances, and the temperature is calculated from their ratio. This tem-temperature has thermodynamic significance if the population of the two states has a thermal (Boltzmann) distribution. The following comments are mainly methodological and apply only to absorption. Similar arguments can be made for the case of emission.

The absorption is measured by an absorption-coefficient α_ν defined by Lambert's law. An index is affixed to indicate a functional dependence on the wave number ν of the radiation. In quantum theory the coefficient is described by Einstein's phenomenological theory of the interaction of radiation with matter. The connection between the two is provided by:

$$\int \alpha_\nu d\nu = \frac{h\nu}{c} B_{mn} N_n \quad , \tag{3}$$

where B_{mn} = Einstein probability for absorption and N_n = population of upper state. This relationship was developed by Füchtbauer [35] and Ladenberg [36]. In equation (3) there is no restriction on the state of the system. If a Boltzmann distribution of the states under consideration is assumed:

$$N_i = g_i \exp(-E_i/kT)/\Sigma g_i \exp(-E_i/kT) \quad ,$$

where g_i = statistical weight,
E_i = energy, and
k = Boltzmann constant, and
the system is restricted to a state of local thermodynamic equilibrium. Temperature can then be calculated using equation (3) if the ratio of $\int \alpha_\nu d\nu$ is measured for two lines, and if the B_{nm} of the corresponding transitions are known. For example, for two lines in absorption, we have:

$$\frac{[\int \alpha_\nu d\nu]_1}{[\int \alpha_\nu d\nu]_2} = \frac{(\nu \cdot B_{mn} \cdot N_n)_1}{(\nu \cdot B_{mn} \cdot N_n)_2} = \frac{(\nu \cdot B_{mn} \cdot g_n)_1}{(\nu \cdot B_{mn} \cdot g_n)_2} \cdot \exp[-(E_{n1} - E_{n2})/kT]$$

The B_{nm} have been calculated for the transitions of OH by Learner [37] and tabulated in the convenient form, $(gB)\nu \equiv P\nu$, for absorption, and for emission, where P is a weighted probability factor.

Thus, only two lines are needed in the line ratio method for temperature determination. A necessary, but not sufficient, condition that the temperature thus obtained refers to LTE is that a plot (sometimes known as a Boltzmann plot) of

$$\log \frac{[\int \alpha_\nu d\nu]_n}{P\nu} \text{ vs } E_n$$

be linear. For such a case the temperature may be derived from the slope of the line, as will be shown in Section 4. There are cases known where such plots have been found to yield two straight lines [38], indicating a different effective temperature for two sets of states.

As in the Na-D line reversal method, the line ratio approach does not contain a criterion of how well the measured temperature approximates the thermodynamic equilibrium value. Coincidence of the 'reversal' and the 'line ratio' temperatures (where greatly different energy states are involved) is good, though not conclusive, evidence that the temperatures have thermodynamic significance.

If $\ell\int\alpha_\nu d\nu$ is to be measured, for optical path length ℓ, the line must be "optically thin," i.e., $\alpha_\nu\ell<<1$. Otherwise $\int(1-e^{-\alpha_\nu\ell})d\nu$ is measured in absorption. From equation (3) it can be shown that this quantity, representing an optical thickness condition, cannot be related to the temperature. The optical thickness of an absorption line of a flame species, OH for example, can be checked by measuring absorption as a function of the number of radiation passes through the flame. This is conveniently accomplished by a White [39] multi-reflection system shown in figure 4. If a flame is optically thick for a particular absorption line, but not too thick, the fractional absorption for various numbers of passes (i.e., ℓ) can be extrapolated to zero passes ($\ell = 0$) to yield $\ell\int\alpha_\nu d\nu$. Examples of this procedure are given in Section 4.2.

2.2.2 Sensitivity

Assuming $\alpha_\nu\ell<<1$ and a state of thermodynamic equilibrium, the temperature sensitivity can be given as

$$\frac{d}{dT}\frac{(\int\alpha_\nu d\nu)_1}{(\int\alpha_\nu d\nu)_2} \equiv \frac{d}{dT}\left[\frac{\alpha_1}{\alpha_2}\right] .$$

Using equation (3) for absorption ratios $r = \frac{\alpha_1}{\alpha_2}$ and energy difference between lower (upper) and upper (lower) states of E_1-E_2

$$\frac{dr}{dT} = r\,\frac{E_1-E_2}{kT}\cdot\frac{1}{T} .$$

Thus, the relative error, $\frac{\Delta T}{T}$, due to error, Δr, in the measurement of the absorption ratio of the two lines is

$$\frac{\Delta T}{T} = \frac{kT}{E_1-E_2}\cdot\frac{\Delta r}{r} , \qquad (4)$$

an expression given by Broida [38].

Values of r can be measured by the ratio of the peak intensity of the lines since

$$\int \alpha_\nu d\nu \simeq [(I_\nu^\circ - I_\nu)/I_\nu^\circ]_{peak} \cdot \Delta\nu_{slit}$$

is invariant with the spectral slit width $\Delta\nu_{slit}$ [28,29], which is usually constant over the scanned spectral range. It is advantageous to maximize the peak intensity of a line by setting $\Delta\nu_{slit} \simeq \Delta\nu_D$, the Doppler width of the line ($\sim$0.005 nm for OH at 2000 K). This minimizes the fractional error with which the peak intensity can be measured and thus Δr of equation (4) which is the sum of these errors for two lines. The same conclusions can be drawn if emission instead of absorption lines are used.

For the flames used in this report the OH radical can be detected in absorption but not by its thermal emission, except near the reaction zone where chemiluminescence occurs. This is in contrast to the high oscillator strength D-lines of Na for which thermal emission is strong. A contributing factor here is the wavelength dependence of the emissivity (Planck's radiation law). In order to demonstrate this dependence we shall assume (arbitrarily) that, at 2200 K, the concentrations of OH and Na are such as to give equal absorption coefficients α_ν at 300 nm and 590 nm, respectively. The application of Kirchhoff's relationship then shows that ε(590 nm)/ε(300 nm) $\sim 10^3$ for emission. Thus, the detection of thermal emission from OH is indeed unfavorable compared with that from the Na-D lines.

2.3 Raman scattering

The application of pure rotational and vibrational-rotational Raman intensities to flame temperature measurements is reasonably well established [40-43] and has been discussed elsewhere in this volume by Drake and Rosenblatt [12]. Raman temperature measurements typically rely on scattering from the major flame species, e.g., N_2, O_2, or H_2. The apparatus used for the present study is shown schematically in figure 6.

2.3.1 Rotational Raman

Determining temperatures from rotational Raman scattering is similar to the line ratio method discussed for OH absorption. In both cases measured relative intensities are converted to relative energy level populations. If only two rotational Raman lines are used, the sensitivity is given by equation (4). It is important to measure intensities of rotational transitions from low to high rotational states to maximize the $E_1 - E_2$ term in equation (4). The most accurate temperatures are calculated from measurement of many, rather than just two, transitions.

In this study, Raman scattering from many individual rotational transitions in N_2 is easily observed and provides reliable temperatures, particularly below 2000 K [12]. A typical spectrum from which temperature data were obtained is shown in figure 7. Both Stokes and anti-Stokes regions were routinely scanned and analyzed, but the anti-Stokes spectrum is not shown since it is essentially a mirror image of the Stokes case. Since

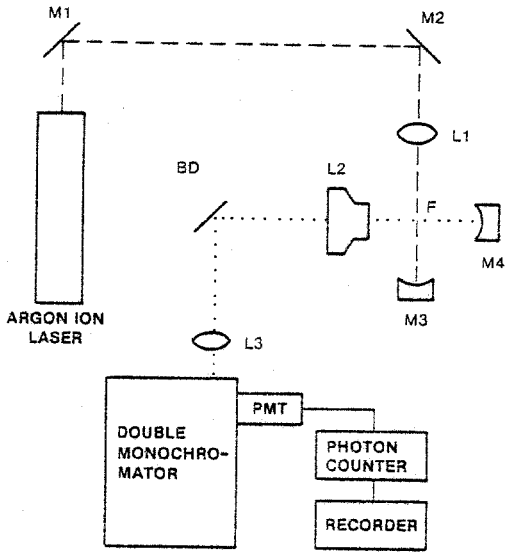

Figure 6. Schematic (in plan view) of Raman spectroscopic apparatus. Output from a 12W argon ion laser (Coherent Radiation) is focused by L1 (60 mm focal length) into the cylindrical sample volume (~0.1 mm diameter x 1.5 mm length--in the same direction as the flame gas flow) of the flame (F). The flame burns in a vertical direction and the vertical spatial resolution is 1.5 mm. The mirror M3 reflects the laser beam back into the sample area creating an external resonating cavity (gain factor 5-7) between M3 and the output mirror of the laser without appreciably increasing the size of the sampled volume. The lens (L2 (~f/1.0, 25 mm working distance) collects light scattered at right angles to the incident laser beam. A two mirror beam detector (BD) and lens L3 focus the scattered light onto a Spex double monochromator which incorporates a thermoelectrically cooled photomultiplier tube (ITT FW130) and photon counting electronics. The mirror M4 effectively doubles the signal intensity by directing light scattered opposite to the collection lens back along the collection optical axis.

a large number (typically 100) of intensities can be measured, rotational Raman temperature measurements are statistically precise (±1 percent for ± σ, where σ is the standard deviation).

In figure 7, notice in addition to the major peaks of alternating intensity, small sidepeaks appear on the low frequency shift side of the major peaks. This is particularly noticeable in the 300-400 cm^{-1} region. These side peaks are the result of pure rotational Raman scattering from vibrationally excited N_2 molecules which naturally become more prominent in hotter flames. For example, figure 8 shows a section of the Stokes rotational Raman spectrum from a hotter $H_2/O_2/N_2$ flame where the side peaks are much more pronounced. The separation of the side peaks from the main peaks in figure 8 increases with the rotational quantum number of the transition involved. This is in quantitative agreement with separations calculated from known energy levels of N_2 (see for example figure 10 in reference [12]).

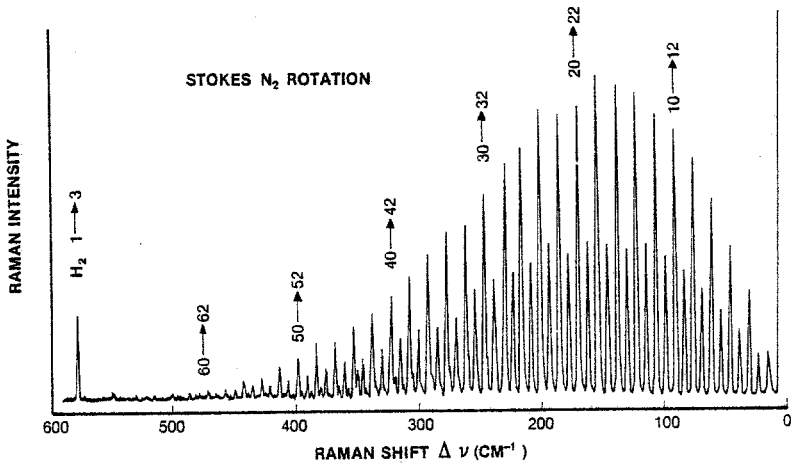

Figure 7. Stokes rotational Raman scattering from flame N_2 and H_2. The only H_2 feature shown is near 600 cm^{-1}. Labels indicate the rotational quantum numbers of the states involved in the transition. Spectrum obtained for the U(4) flame at a location, relative to the face of the rectangular burner, of z = 30, y = 2, and x = 0 mm (see fig. 11 coordinate system). Temperature (rotational) corresponds to 2113 K (see fig. 12).

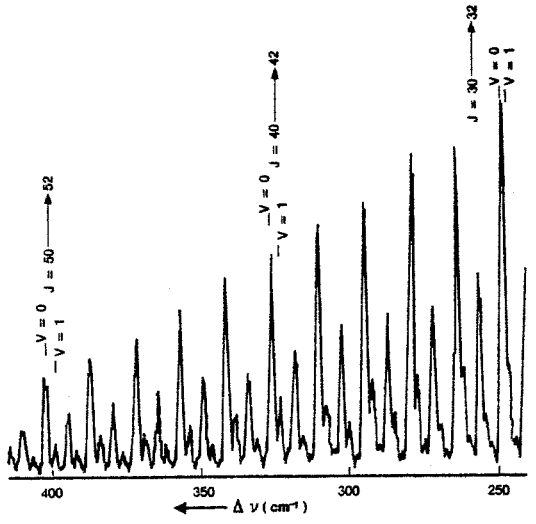

Figure 8. Segment of the Stokes rotational Raman Spectrum from an O(2) torch flame showing the presence of hot bands (v = 1). Temperature (rotational) corresponds to 2450 K.

The effects of scattering from vibrationally excited molecules must be accounted for in temperature determinations from pure rotational Raman spectra. Above about 2000 K, the overlapping contribution of pure rotational Raman transitions from vibrationally excited N_2 molecules necessitates a large correction (>100 K) in the temperature calculation. Although this correction could be made precisely if the spectrometer slit function was accurately known, in practice additional uncertainty is introduced because the correction is very sensitive to the shape and width of this function. Other corrections necessary for accurate temperature determinations from rotational Raman spectra, i.e., centrifugal distortion corrections to the line strength, are relatively small for N_2 [12]. The statistical uncertainties in the calculated temperature (±1 percent in the best cases) do not include the additional uncertainties in the magnitude of the correction terms which may be a large source of uncertainty, particularly for temperatures greater than 2000 K.

2.3.2 Vibrational Raman

More commonly, for the measurement of temperature, vibrational rather than rotational Raman intensities are used. Since individual rotational transitions within the vibrational-rotational Q branch of N_2 cannot be resolved at high temperature in conventional Raman measurements, computer generated profiles are required. At least three methods of determining the flame temperature from vibrational Raman scattering intensities are possible. These are:

(1) Stokes/anti-Stokes intensity ratios,

(2) comparison of the entire Stokes profile with computer generated profiles, and

(3) determination of the Stokes intensity ratios for transitions from the ground state and from vibrationally excited states [12,40].

Previous studies have found that the various vibrational Raman methods give flame temperatures which agree with each other and with radiation corrected thermocouple measurements (within 2 percent for the best cases) for premixed flames of H_2-air [22], CH_4-air [42], and NH_3-O_2 [42].

In the present study, Stokes vibrational Raman scattering profiles from N_2 are scanned. Results are similar to spectra shown in figure 11 in reference [12]. Ratios are calculated from intensities measured for the $v = 1 \rightarrow 2$ peak and the $v = 0 \rightarrow 1$ peak and for the $v = 2 \rightarrow 3$ peak and the $v = 0 \rightarrow 1$ peak. These measured ratios are converted to a vibrational temperature by comparison with intensity ratios obtained from computer band profile calculations shown in figure 9. A trapezoidal spectrometer slit function, determined experimentally from the shape of the $J = 1 \rightarrow 3$ rotational Raman peak from room temperature H_2, was used in the computer calculation. The band profile calculations are similar to those of Setchell [43] and Lapp and Penney [22,40] who include the isotropic part of the $Q(\Delta J = 0)$ branch which is the dominant part of the vibrational-rotational Raman profile. However, the present calculations also include contributions from, (1) the anisotropic part of the Q branch, (2) $O(\Delta J = -2)$ and $S(\Delta J = +2)$ branch transitions, and (3) corrections to the line strength due to centrifugal distortion (discussed in detail in reference [12]). These additional

correction terms have a negligible (<10 K at 2000 K) effect on the calculated intensity ratios. Uncertainties in vibrational temperatures (ΔT), measured from peak intensity ratios are estimated by the uncertainty in measuring the intensity ratio (Δr) multiplied by $(dT/dr)\big|_r$ determined from figure 9. From photon statistics the minimum uncertainty in an intensity measurement equals $\sqrt{I}$ where I is the number of detected photons so

$$\Delta r \gtrsim \sqrt{I(v = 1 \rightarrow 2)}/I(v = 0 \rightarrow 1) \quad .$$

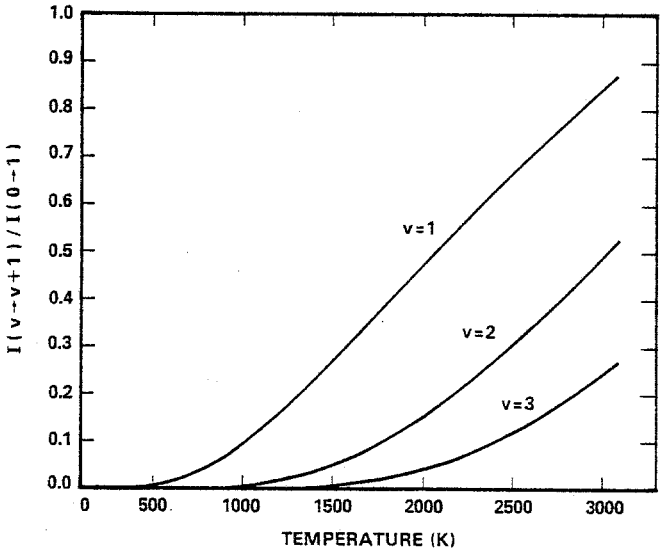

Figure 9. Computer calculation of the N_2 Stokes intensity ratios for the $v \rightarrow v + 1$ transition compared to $v = 0 \rightarrow v = 1$. An experimentally determined slit function was used in the calculation.

2.4 Adiabatic temperature computation

Calculated adiabatic flame temperatures are computed using the free energy minimization algorithm implemented by Gordon and McBride (GB) [4].

The calculations are posed as "assigned" enthalpy-pressure problems since, by definition, the term adiabatic implies no net heat transfer. The calculations are specified using the mixed burner-input gas (ideal mixing) heats of formation as the enthalpy to be assigned for reactants. Where the reactant mixture gases are in the data base, the program is requested to calculate the initial heats at laboratory initial temperature and pressure. Where the initial gases are not present in the data base and are not expected to be product species, heats of formation at laboratory conditions are supplied. In this case, selected thermodynamic data are prepared for inclusion in the data base using GB equations (90-92) (see [4]) via a fit to C_p/R data. It should be noted that in the syntax of this program, assigned enthalpies are defined by GB equation (89),

$$\Delta H_T^\circ = (\Delta H_f^\circ)_{298.15} + (H_T^\circ - H_{298.15}^\circ)$$

and for assigned enthalpy-pressure problems, the product heat is set equal to the reactant heat.

Calculations varying the laboratory pressure by ±10 percent showed the expected insignificant effect of small errors in knowledge of the exact pressure (expected error <±1 percent) of the reactants just below the reaction zone. For the $H_2/O_2/N_2$ system the thermodynamic data for reactants, products and intermediate species are sufficiently accurate that the uncertainty in calculated temperature should not exceed one degree Kelvin. Calculations were also made to verify the insignificant cooling effect of the small amounts of added H_2O in the Na-D line reversal method.

3. Burners

Two water-cooled (but non-quenching) burners, of differing geometry, were used to generate laminar premixed $H_2/O_2/N_2$ flames at atmospheric pressure. Both burners were constructed after the fashion of that used by Padley and Sugden [16], and subsequently by many others [2,17]. Bundles of stainless steel capillary tubing, or hypodermic needles, are the essential feature of this burner-type. Stiff columns of flame gas, over a distance of at least 50 mm, are provided by such burners. For optical convenience and minimization of convection effects, the burners were mounted vertically. The low heat losses associated with this type of burner allow flames to be supported under near-adiabatic conditions.

3.1 Cylindrical burner

For comparison with literature data one of the burners was designed and constructed to be basically very similar to the Padley-Sugden burner [16]. This burner type produces well shielded circular cross section pseudo-flat premixed flames. The inner flame has a 0.7 cm cross section and the concentric shield flame produces an overall cross section of 1.1 cm. Additional details of construction, characteristic properties, kinematic control, and the auxiliary gas flow control system will be given elsewhere in connection with a discussion of species concentration profiles [44]; see also reference [45].

3.2 Rectangular burner

A second burner of rectangular configuration was designed for use with the White multi-reflection system, used to make optical thickness corrections in the OH absorption measurements. In the White cell (fig. 4), there is an inherent spread (18 mm) in the lateral dimension of the light beams passed by the cell. In order to confine this spread to a well defined cross section of the flame, with an essentially constant temperature, a rectangular capillary burner was constructed similar to the design of Padley and Sugden and modelled after that of Adams, et al. [46]. The capillary tube bundles are supported by a water-cooled brass burner body. The rectangular central flame section (cross section

3.6 mm x 22 mm) contains 90 stainless steel tubes (0.028 in o.d., 0.016 in i.d.) and the encircling shield flame section (5.2 mm x 25 mm) contains 148 tubes. It should be noted that the cross sectional area for the central flame is twice that for the corresponding dimension of the cylindrical burner. Since air entrainment was considered more probable with this long narrow burner, a rectangular slot (0.005 in wide) with outer dimensions of 10 mm x 30 mm, provided an additional shield of argon around the flame. Experience has shown such a shield to be unnecessary with the cylindrical burners. The rectangular burner design had the additional advantage for Raman measurements of permitting short focal length, low f-number collection, lenses to be used for efficient light collection.

For both burners, the same gas flow and kinematic control systems were used. Gas flows were controlled by pressure regulators and measured by calibrated flow rotameters. The central and shield burner gas compositions were identical and adjusted so that the linear flow velocities were the same. The argon flow rate was adjusted (arbitrarily) to fifty percent of the value where turbulence was observed.

4. Results

Flame temperature profiles have been obtained using the optical methods discussed in Section 2 for the combinations of flames and burners listed in table 1.

Table 1. Combinations of Measurement Technique and Burner-Flame Composition Used

flame $H_2/O_2/N_2$	4/1/4[a]	3.4/1/2[a]
burner	U(4)[b]	O(2)[b]
cylindrical[c]	Na-D line	
	none[e]	
	Raman	
rectangular[d]	Na-D line	Na-D line
	OH-absorption	OH-absorption
	Raman	Raman

[a]Mole ratios of initial gas mixture (NTP); gas flows were 141.5 and 94.3 cm^3/s for the O(2) and U(4) flames, respectively, at NTP.

[b]"Standard" notation in common use, e.g., see Miller [47] and elsewhere in this volume [2].

[c]Refers to three dimensional geometry of flame.

[d]Refers to cross sectional geometry of flame.

[e]The cross sectional temperature plateau was not wide enough to allow use of multibeam passing for OH-absorption measurement of temperature.

4.1 Cylindrical burner

For the O(2) flame-cylindrical burner combination, a high background luminosity and relatively unfavorable scattered light collection optics prevented useful high precision Raman temperature data from being obtained. Also, the relatively narrow cross sectional temperature plateau meant that the OH-absorption method could not be applied to this especially optically thick flame. Thus no useful comparisons between methods could be obtained for this flame-burner combination.

Longitudinal temperature profiles (i.e., along the z coordinate of fig. 10) were obtained by passing the light or laser beams through the flame along the x axis (see fig. 10) and adjusting the motor driven micrometer burner drive along the z axis. Application of the Raman and Na-D line reversal methods to temperature profile determinations were relatively straightforward. However, this was not the case for the line-ratio method using optical absorption by the OH radical as the condition for optical thinness ($\alpha_\upsilon \ell << 1$) was not met, except for very weak transitions. The optical thickness was checked and extrapolated to $\alpha_\upsilon \ell << 1$ using the White multi-reflection system.

The longitudinal temperature profile, for the U(4) flame, obtained by the vibrational Raman method is compared with that obtained by the Na-D line reversal technique

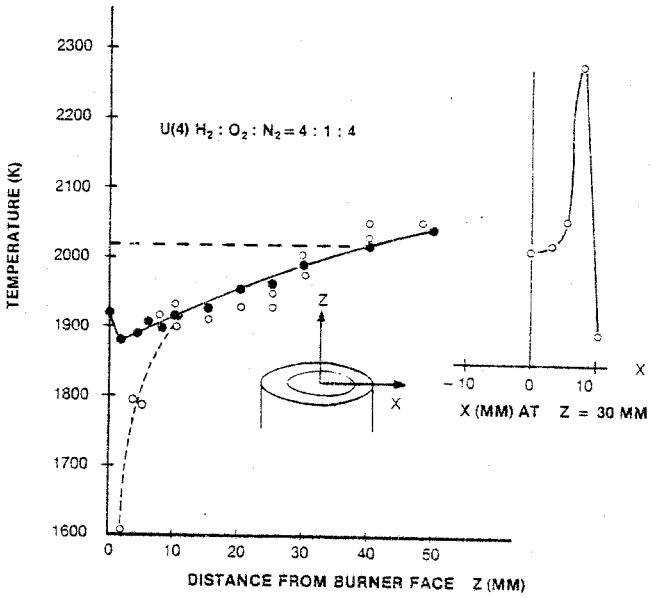

Figure 10. Longitudinal (z) and transverse (x) temperature profiles, for y = 0 mm, using Na-D_1 line reversal (closed circles) and vibrational Raman techniques (open circles). Burner: cylindrical. Broken horizontal line indicates calculated adiabatic temperature. Flame gas compositions (initial at STP) are given as mole ratios. Calculated linear hot gas velocity equals 1.5×10^3 cm/s.

in figure 10. The calculated adiabatic temperature and a transverse Raman temperature profile are also shown. Note (in fig. 10) that in the outer flame regions (z = 50 mm or x = 8 mm) the observed temperatures exceed the maximum allowed adiabatic value for the initial flame stoichiometry indicated.

Previous information on transverse temperature profiles for $H_2/O_2/N_2$ flames using the Padley-Sugden type burner is limited to the recent thermocouple measurements of Hayhurst and Kittelson [48]. Evidence of a several hundred degree temperature rise at the outer flame edge due to afterburning was noted for fuel-rich flames. Leaner flames, on the other hand, showed a tendency to decrease in temperature along the radial axis due to the cooling effect of air entrainment. Under these non-isothermal conditions, line of sight methods will yield temperatures intermediate of the highest and lowest values along the optical path [28].

4.2 Rectangular burner

A summary of the data obtained using the various methods is given in figure 11. In addition to the vibrational Raman data (fig. 11), rotational Raman spectra and temperatures were obtained, at z = 30, y = 2 mm, for the U(4) flame as shown in figure 7. To obtain similar data for the O(2) flame, a small torch burner was used (see fig. 8). Temperatures were determined indirectly from measured rotational Raman intensities using the slopes of the linear least square data fits, such as those given in figure 12. Stokes and anti-Stokes data points are plotted on the same graph and any deviation from a Boltzmann distribution of rotational states would be evident since both data sets would simultaneously deviate from the straight line.

Vibrational Raman spectra were used to obtain the flame temperature profiles for the U(4) flame shown in figure 11. Note the large temperature gradient (45 K/mm) which exists across the burner (along the y axis) with the temperature maximum 4 mm from the center. A somewhat lower gradient (~38 K/mm) was found for the cylindrical burner (see fig. 10), with the central 10 mm having a nearly flat temperature profile (~10 K/mm). The temperatures determined from the rotational (2113 ± 22 K) and the vibrational (2096 ± 40 K) Raman spectra at z = 30 mm and y = 2 mm are in good agreement with each other. For the U(4) flame data in figure 11, seven N_2 Stokes vibrational Raman spectra were also obtained at the location, z = 30, y = 0 mm. The vibrational Raman temperatures were determined from measured peak intensity ratios for $v = 1 \rightarrow 2$ compared to $v = 0 \rightarrow 1$, and $v = 2 \rightarrow 3$ compared to $v = 0 \rightarrow 1$ in the N_2 Stokes vibrational Raman profile. The seven temperature values ranged from 2006 to 2043 K with an uncertainty of ~ ± 40 K. Only the three median values are shown in figure 11.

Raman measurements on the less fuel rich O(2) composition were more difficult, particularly for the vibrational Raman, because of the increased flame luminosity. At 30 mm above the burner face the temperatures measured were 2500 ± 150 K from vibrational and 2450 ± 40 K from rotational Raman spectra. The lower uncertainties in the rotational temperature data result from the reduced background luminosity associated with the use of smaller slit widths (~2 cm^{-1} versus ~5 cm^{-1} resolution for vibrational data). These stated

uncertainties are statistical only. True uncertainties, particularly for rotational temperatures, are larger and must include uncertainties in temperature corrections for vibrationally excited molecules [41].

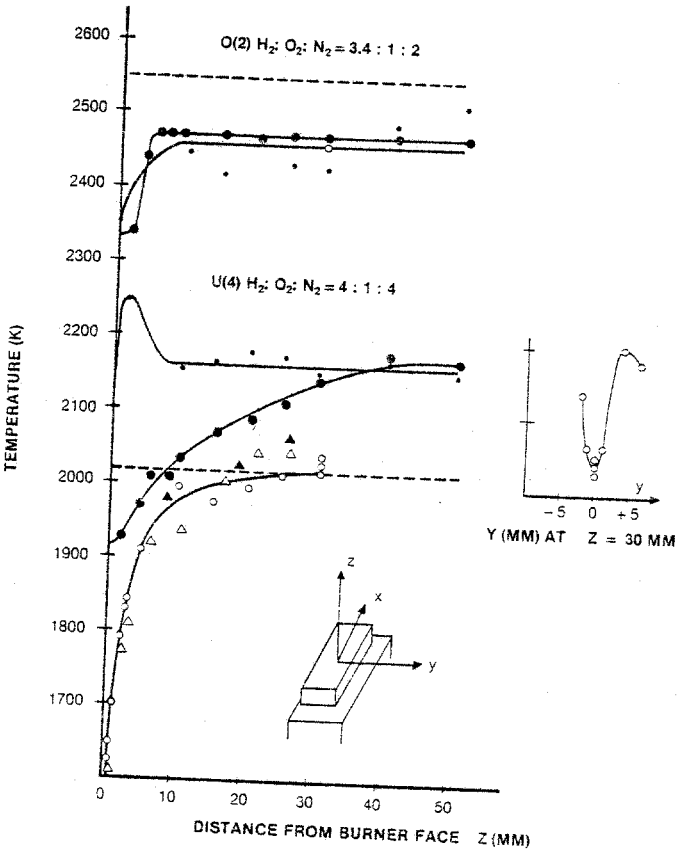

Figure 11. Longitudinal (z) and transverse (y) temperature profiles, at x = 0 mm, for U(4) and O(2) flames using Na-D_1 line reversal (large closed circles), vibrational Raman (open circles) and OH absorption (small closed circles). Broken horizontal line indicates calculated adiabatic temperature. Burner: rectangular; argon shield on. Flame burns in z direction. Flame gas compositions are given as mole ratios of initial gas mixture. Calculated linear hot gas velocities = 0.75×10^3 cm/s [U(4)] and 0.96×10^3 cm/s [O(2)]. Data from figure 10, normalized to the same time scale, are indicated by closed triangles (Na-D line) and open triangles (Raman).

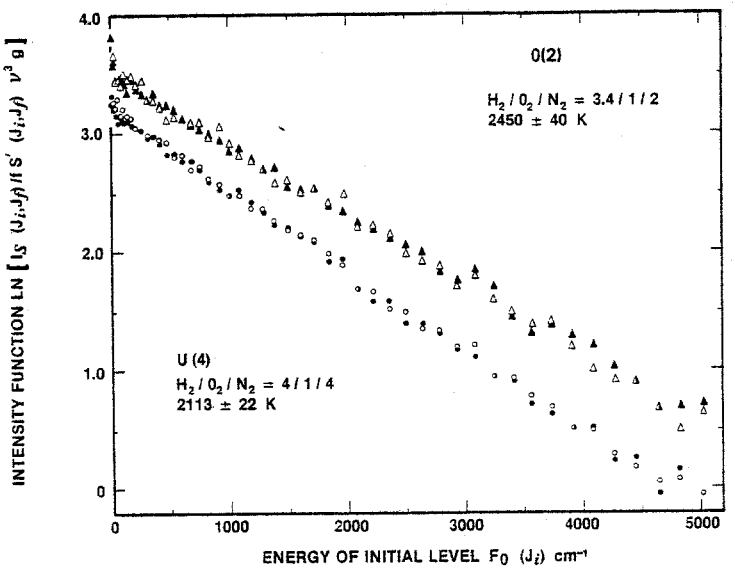

Figure 12. Temperature determination plot (Boltzmann-type) from rotational Raman intensities. I_s are relative Raman intensities, measured from spectra such as that shown in figure 7, and corrected for contributions from scattering by vibrationally excited N_2 molecules; f S' (J_i,J_f) is the rotational Raman line strength corrected for centrifugal distortion effects; is the frequency of the scattered light; g is the nuclear degeneracy factor; and F_0 (J_i) is the energy of the initial energy level. The temperature is inversely proportional to the slope. The uncertainties listed are ± two standard deviations including statistical uncertainty only. Large temperature corrections are required to correct for contributions from transitions from vibrationally excited N_2 molecules. For the O(2) flame, T = 2450 ± 40 K (2262 ± 42 K without correction). For the U(4) flame, T = 2113 ± 22 K (2082 ± 22 K without correction). The required experimental slit function was determined by measuring the line shape of the H_2 (J = 1 → 3) line at room temperature. The slit function is approximately trapezoidal with f w h m = 2.05 cm^{-1} and top = 0.76 cm^{-1}. Flame location z = 30 and y = 0 mm for O(2) and z = 30 and y = 2 mm for U(4) flame.

For the line ratio method of temperature measurement, a suitable band for measurement of the OH absorption spectrum is that in the region of 306.4 nm (see fig. 5). A plot of the optical density of the absorption lines versus the number of radiation passes through the flame (fig. 13) shows that many of the lines are not optically thin. Extrapolation of the fractional absorption I_{abs} to $\alpha_\nu \ell \ll 1$, shown in figure 13, yields values of I_{abs} which can be converted by the theory (see Section 2.2) to a temperature. Alternatively, the data can be expressed in logarithmic form, as shown in figure 14. Both sets of curves (figs. 13 and 14) yield the same values of I_{abs} and hence temperature. The self

consistency of the extrapolation procedure and the thermal nature (Boltzmann distribution pertains) of the selected rotational states is demonstrated by the linear relationships given in figure 15 for both the U(4) and O(2) flames. Another alternative extrapolation procedure for obtaining corrected values of I_{abs} is from a growth curve (van der Held plot) of the type shown in figure 16. The extrapolated I_{abs} values obtained from the growth curves also agree with those using the procedure in figure 13.

Except for data at the z = 30 mm location (see fig. 11), where the many line Boltzmann-type plots of figure 15 were used, temperatures were obtained using the corrected intensity ratios for the $R_2 4$ and $R_2 15$ lines (see fig. 5). As is shown in figure 13, these lines satisfy a condition of relatively low degree of optical thickness. For the U(4) and O(2) flames with one pass, optical thickness temperature corrections of ~0 and ~19 K are required, respectively. We estimate from eq. (4) that the error in the temperature measurement using these lines is 40 K for the U(4) and 60 K for the O(2) flame compositions.

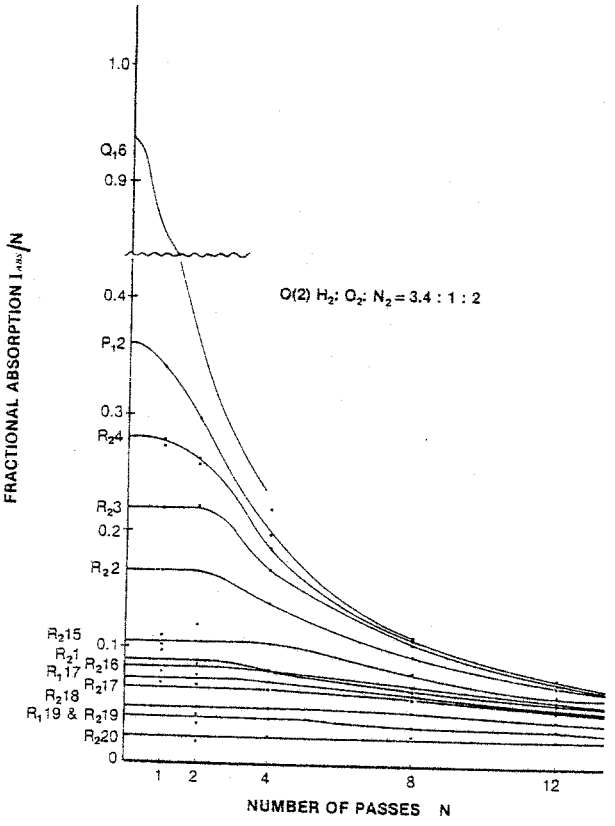

Figure 13. I_{abs}/n vs n, where $I_{abs} = [(I_\nu^\circ - I_\nu)/I_\nu^\circ]_{peak}$ and n is the number of traversals through the flame via the White multi-reflection system at 30 mm from face of rectangular burner. As $n \to 0$ the slope must approach zero. Lines are identified in figure 5.

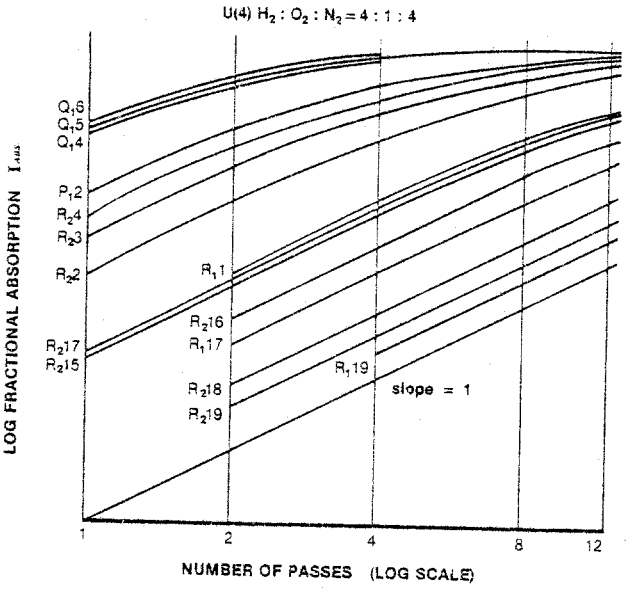

Figure 14. Experimental growth curves (van der Held plots) of absorption lines shown in figure 5 versus number of traversals through flame at 30 mm from the face of rectangular burner. When $\alpha_\nu \ell \ll 1$ (optically thin) the slope of each curve approaches the value 1. $I_{abs} = [(I_\nu^\circ - I_\nu)/I_\nu^\circ)]_{peak}$

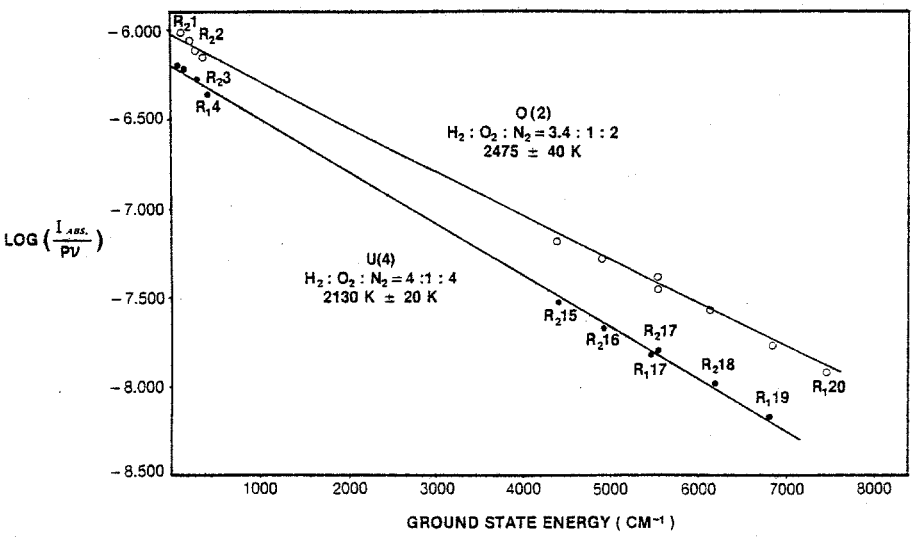

Figure 15. $\log[(I_{abs}/n)/P\nu]_{n\to 0}$ vs E_n is energy of initial state of a transition of wave number ν (cm^{-1}). $I_{abs} = [(I^{\circ}_{\nu}-I_{\nu})/I^{\circ}_{\nu}]_{peak}$. Lines are linear least squares fits to data points obtained at the z = 30 mm position. Data were calculated from extrapolated $(I_{abs}/n)_{n\to 0}$ taken from figure 13; $P \equiv g_n B_{nm}$ where B_{nm} is Einstein probability for absorption; and E_n for the labelled transitions are tabulated in reference [37]. The temperature is calculated from the slope $(-2.303\ kT)^{-1}$ of the lines where $k = 0.697\ cm^{-1}/K$. Rectangular burner data.

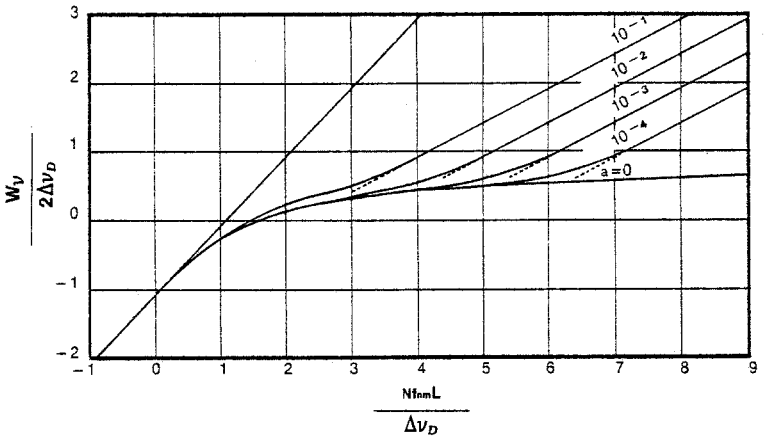

Figure 16. Growth curve (hypothetical) for exponential absorption [49]. $W = \int[(I^{\circ}_{\nu}-I_{\nu})/I^{\circ}_{\nu}]d\nu = [(I^{\circ}_{\nu}-I_{\nu})/I^{\circ}_{\nu}]_{peak}\cdot\Delta\nu_{slit}$ vs Nf_{nm}. N is the number of absorbing "centers" in the initial state E_n contained in a 1 cm^2 column of length ℓ. f_{nm} is the oscillator strength of the transition $n \to m$. a = damping constant γ/Doppler width $\Delta\nu_D$. Straight line of slope 1 is region in which $\alpha\ \ell \ll 1$ (optically thin). For OH at 2000 K, a $\sim 10^{-2}$ (collisional broadening neglected).

5. Discussion

5.1 Cylindrical burner

Except for the region close to the burner face, the agreement between the results of the various methods is strong evidence that the rotational, vibrational, and electronic temperatures measured, respectively, by the rotational Raman, vibrational Raman, and the Na-D line reversal methods, each represent a thermal equilibrium state (see fig. 10). Close to the burner face, chemiluminescent excitation of Na atoms by radical recombination [50] leads to an erroneously high temperature determination, particularly for the U(4) flame where the ratio of excess to equilibrium radical concentration is known to be greater. Disagreement between population temperatures for the Na-D line and OH ($X^2\Pi$) states are known and have been attributed to possible non-equilibrium state conditions in an atmospheric methane-oxygen flame, particularly under turbulant conditions [18]. The transverse temperature profile (fig. 10) indicates that the flame is non-isothermal along the transverse axis. This condition should not significantly affect the Raman data as they are essentially 'point' source results. The reversal method, on the other hand, measures some transverse line of sight temperature average of the region encountered by the passage of radiation from the reversing source through the flame [28]. Thus, the temperatures measured by the two methods may not be the same. The excellent agreement obtained here is probably due to the presence of a relatively large isothermal central flame region (~10 mm) as compared with the thinner, non-isothermal outer region.

5.2 Rectangular burner

The Raman temperature data (fig. 11) for the U(4) flame are identical (within experimental uncertainty) to those obtained with the cylindrical burner (fig. 10), when allowance is made for the different gas velocities in both cases. These data are also quite consistent with the calculated adiabatic temperature. However, the Na-D line reversal temperatures are appreciably different to the Raman results and the corresponding cylindrical burner data. As these data (at $z > 10$ mm) lie well above the adiabatic limit, either the system, with respect to the Na-D line transition, is not at local thermal equilibrium or the average composition across the flame (along y axis) is closer to a stoichiometric (hotter) mixture than the initial U(4) composition. Arguments in favor of the latter condition will be presented in Section 6.

Note (fig. 11) that the OH-absorption temperature data are similar to the Na-D line results at $z \geq 30$ mm but deviate at $z \leq 30$ mm. This difference can be attributed to the greater influence of the shield flame properties on the OH temperature relative to the Na-D line data. At $z < 30$ mm most of the Na is still in the inner flame, but at larger distances radial diffusion of Na to the hotter (Raman evidence) outer flame will cause an increase in the reversal temperature.

In contrast to the U(4) flame results, the O(2) flame data show good agreement between the three temperature measurement techniques and are consistent with the adiabatic limit. A

transverse Raman temperature profile (along the y-axis) was not obtained for the O(2) flame due to interference from the relatively high background luminosity.

5.3 Burner comparisons

It is well established [2,16,47] that the z = 30 mm position for flames supported by Padley-Sugden-type burners (and with similar flow velocities) is a convenient comparison point. This position is sufficiently far removed from the reaction zone to be free of chemiluminescence and other radical-controlled non-equilibrium effects, but is not far enough to be significantly influenced by air-entrainment. Table 2 shows a summary of our data and an inter-comparison with literature data at the z = 30 mm, or an equivalent (with respect to flow time), flame position. The Na-D line data of Miller [47] is typical of that obtained by other workers of the Sugden school. Note that our corresponding data are in excellent agreement. With the exceptions already noted, the intra-comparison for the various techniques and burners is also very good and indicative of the reliability of the experimental approach.

Table 2. Flame Temperature Comparisons[a]

Initial Mole Ratio $H_2/O_2/N_2$	Argon Shield	Na-D Line Reversal	OH Absorption	Vibrational Raman	Rotational Raman	Calculated Adiabatic[e]
4.0/1.0/4.0	no	2100 ± 20		2146 ± 40		
	yes	2060 ± 20	2160 ± 40	1980 ± 40	g	2019
	--	1990 ± 20[c]		2010 ± 40[c]		
	--	2020[d]				
3.4/1.0/2.0	yes	2470 ± 20	2425 ± 60	2500 ± 150[b]	f	2545
	--	2475[d]				

[a] Temperature in degrees K measured at a height of 30 mm (cylindrical burner) or 15 mm (rectangular burner) above the burner face. Rotational Raman uncertainties are given as two standard deviations.

[b] Data obtained at z = 30 mm, y = 0 mm but value should be similar at z = 15 mm (see fig. 11).

[c] Data underlined are for the cylindrical burner, all other data refer to the rectangular burner.

[d] Data obtained by W. Miller [47] using an almost identical burner and gas flow condition.

[e] These data should be accurate to within a degree.

[f] See figure 12 for data obtained at z = 30 mm, y = 0 mm.

[g] A comparison of rotational and vibrational Raman temperatures was made at z = 30 mm, y = 2 mm, where T = 2113 ± 22 and 2096 ± 40, respectively.

6. Conclusions and Summary

Temperatures of atmospheric pressure premixed $H_2/O_2/N_2$ flames have been measured by Na-D line reversal, OH absorption, and Raman scattering (vibrational and rotational) techniques. With a cylindrical burner of design very similar to the widely used Padley-Sugden burner [16], longitudinal temperature profiles (along the direction of gas flow) measured by the Na-D line and Raman scattering methods agreed well within experimental error ($\sim \pm 50$ K) and with previous Na-D line temperature measurements [47] for distances of 5-50 mm above the burner surface. For distances less than 5 mm the Na-D line temperatures are excessively high due to well known chemiluminescent effects.

Temperature measurements on U(4) and O(2) flame compositions, using a rectangular burner, were in serious disagreement for the former but not the latter flame. The discrepancies can be traced to the effects of air entrainment and subsequent combustion of H_2 in this flame. The rectangular burner produced a thin sheet of flame with a larger circumference-to-area ratio than for the cylindrical burner, making the rectangular burner more susceptible to air entrainment effects. That the O(2) flame apparently did not suffer from this difficulty may be explained by the lower excess H_2 present in this case. However, the extent of this entrainment difficulty for various flame compositions cannot be determined a priori. This indicates that caution must be exercised in the selection, and empirical validation, of new burner-flame composition combinations if the results are to be used for temperature and chemical diagnosis.

A summary of the experimental evidence for significant air entrainment with the rectangular burner is as follows:

- Raman temperature transverse profiles, measured at a constant height (30 mm) above the burner, indicate that the outer part of the flame is 150-200 K hotter than the flame center.
- In the center of the flame, and at a distance of 30 mm above the burner, temperatures measured by line-of-sight techniques (Na-D line reversal and OH absorption) are higher by ~150 K than Raman temperature measurements.
- Flame temperatures at 30 mm above the burner increased when the argon shield flow, which normally provides some protection against air entrainment, was removed. The Raman temperature increased by 125 K and the Na-D line value by 42 K.
- Measured temperatures using Na-D line reversal or OH absorption are above the calculated adiabatic flame temperature (2019 K). Similarly, temperatures determined from Raman scattering are above the calculated adiabatic temperatures near the outer parts of the flame or in the center of the flame without the argon shield flow.
- The temperature measured by the three techniques on the cylindrical burner are in agreement within experimental error. However, as is evident by the Raman temperature transverse profile at 30 mm above the burner, the temperatures are again non-uniform, the outer part of the flame being much hotter.

The major difference in burner performance is that the cylindrical burner provides a central region of essentially constant temperature over a lateral distance of ~10 mm. Thus

the presence of a narrow high temperature outer region has relatively little effect on the Na-D line or OH temperature measurements. The flame centers (along z axis) for both burner types had essentially identical temperature profiles (on a flow time basis) as determined by the Raman technique.

We should emphasize that the temperature measurement methods of (1) Raman, (2) Na-D line, and (3) OH absorption, with shielded flames, each refer to a different flame element. Method (1) gives essentially point source information, method (2) data on the whole lateral section of the seeded inner flame, and method (3) data on the combined lateral sections of the inner and shield flames. Thus, if these lateral sections are non-isothermal, each method will yield different temperature information.

Comparison of the various optical temperature methods indicates that the Na-D line reversal technique is the best method for measuring temperatures where the optical paths through the inner flame are isothermal. This method has the greatest precision (limited by the reproducibility of reading an optical pyrometer), is faster and easier, and requires less expensive equipment than Raman techniques. However, when "point" temperature measurements are required, as in flames with large amounts of air entrainment, Raman measurement are required since line of sight measurements give only an integrated average temperature.

We wish to acknowledge Dr. W. J. Miller for the loan of his Padley-Sugden-type burner, which we reproduced, and for useful discussions on the Na-D line reversal method. Dr. D. W. Bonnell assisted with the calculation of adiabatic flame temperatures and with the design of burners and gas feed systems. Mr. A. Sessoms assisted with data taking and maintenance of the apparatus. Suggestions by Dr. Gary Mallard for improving the manuscript are also appreciated.

References

[1] Reuther, J. J., Measures of effectiveness and mechanisms for chemical and physical inhibition of quenched adiabatic premixed flames, this volume.

[2] Miller, Jr., W. J., The use of flames as media for the study of ion-molecule thermochemistry, this volume.

[3] Jensen, D. E., Chemical processes in high Reynolds number turbulent diffusion flames, this volume.

[4] Gordon, S. and McBride, B. J., NASA SP-273, NTIS Document No. 71 37775 (1971).

[5] Creighton, J. R. and Lund, C. M., Modeling study of flame structure in low-pressure, laminar, premixed methane flames, this volume.

[6] JANAF, Joint Army Navy Air Force Thermochemical Tables, 2nd ed., NSRDS-NBS 37 (1971) U.S. Government Printing Office, Washington, D.C.

[7] Baulch, D. L., Drysdale, D. D., Horne, D. G., and Lloyd, A. C., Evaluated kinetic data for high temperature reactions, Vol. I., Homogeneous Gas Phase Reactions of the H_2/O_2 System (Butterworths, London, 1972).

[8] Ratajczak, E. and Trotman-Dickenson, A. F., Supplementary Tables of Bimolecular Gas Reactions (Publications Department, UWIST, Cardiff, Wales, 1970).
[9] Eckbreth, A. C. and Hall, R. J., CARS diagnostic investigations of flames, this volume.
[10] McDonald, J. R., Baronavski, A. P., Pasternack, L., Lamont, S., and Harvey, A. B., New optical diagnostic techniques for temperature and species concentration measurements in flames, this volume.
[11] Roquemore, W. M. and Yaney, P. P., Comparison of thermocouple, gas sampling and Raman measured temperatures in an afterburning turbojet engine plane, this volume.
[12] Drake, M. C. and Rosenblatt, G. M., Raman spectroscopy in high temperature chemistry, this volume.
[13] Anderson, W. R., Allen, Jr., J. E., Fansler, T. D., and Crosley, D. R., Laser generated opto-acoustic pulses in an atmospheric pressure flame, this volume.
[14] Bradshaw, J., Bower, J., Weeks, S., Fujiwara, K., Omenetto, N., Haraguchi, H., and Winefordner, J. D., Application of the two line atomic fluorescence technique to the temporal measurement of small volume flame temperatures, this volume.
[15] Self, S. A., Diagnostic techniques in combustion MHD flows, this volume.
[16] Padley, P. J. and Sugden, T. M., Proc. Roy. Soc. A248, 235 (1958).
[17] Hastie, J. W., High Temperature Vapors: Science and Technology (Academic Press, New York, 1975).
[18] Fissan, H. J., Combust. Flame, 17, 355 (1971); ibid, 19, 11 (1972).
[19] Klingenberg, G. and Mach, H., Combust. Flame, 27, 163 (1976).
[20] Daily, J. W. and Kruger, C. H., J. Quant. Spectrosc. Radiat. Transfer, 17, 327 (1977).
[21] Snelleman, W., Combust. Flame, 11, 453 (1967).
[22] Lapp, M., Goldman, L. M., and Penney, C. M., Science, 175, 112 (1972).
[23] Striker, W., Combust. Flame, 27, 113 (1976).
[24] Ahrich, R., Vovelle, C., and Delbourgo, R., Combust. Flame, 32, 171 (1978).
[25] Bennett, J. G., and Pirani, M., J. Inst. Fuel, 12, No 64, SI (1939).
[26] Fery, C., Compt. Rend. 137, 909 (1903).
[27] Gaydon, A. G. and Wolfhard, H. G., Flames. Their Structure, Radiation and Temperature, 3rd ed., p. 239. (Chapman and Hall, Ltd., London, 1970).
[28] Sasaki, Y., Jap. J. Appl. Phys. 5, 439 (1966).
[29] Definitions, Terminology and Symbols of Radiation Quantities are as in Max Planck, Theory of Heat Radiation, 2nd ed. (1913); (Dover Publications, New York, 1959).
[30] Czerny, M. and Walther, A., Tables of the Fractional Functions for the Planck Radiation Law (Springer-Verlag, Berlin, 1961).
[31] Nielsen, J., Thornton, V., and Dale, E. B., Rev. Mod. Phys. 16, 307 (1944).
[32] De Prima, C. R. and Penner, S. S., J. Chem. Phys. 23, 757 (1955).
[33] Kohn, H., Phys. Z. 29, 49 (1928).
[34] Bass, A. M. and Broida, H. P., NBS Circ. 41 (1953).
[35] Fuchtbauer, C., Phys. Z. 21, 322 (1920).
[36] Ladenburg, R., Z. Phys. 4, 451 (1921).
[37] Learner, R. C. M., Proc. Roy. Soc. A269, 311 (1962).

[38] Broida, H. P., Temperature. Its Measurement and Control in Science and Industry, Vol. II, p. 269 (Reinhold Publ. Co., New York, 1955).

[39] White, J. U., J. Opt. Soc. Amer. 32, 285 (1942).

[40] Lapp, M. and Penney, C. M., in Adv. in Infrared and Raman Spectrosc. R. J. H. Clark and R. E. Hester, eds., Vol. 3, chap. 6 (Heyden and Sons, Ltd., London, 1977).

[41] Drake, M. C. and Rosenblatt, G. M., Combust. Flame, 33, 179 (1978).

[42] Schoenung, S. M. and Mitchell, R. E., Sandia Report SAND 77-8722 (Oct. 1977).

[43] Setchell, R. E., AIAA Paper 76-28 (1976).

[44] Hastie, J. W. and Bonnell, D., Species Concentration Profiles for Premixed $H_2/O_2/N_2$ Flames, determined by Molecular Beam Mass Spectrometry, to be published (1979).

[45] Hastie, J. W. and McBee, C., Mechanistic Studies of Triphenylphosphine Oxide-Poly (Ethyleneterephthalate) and Related Flame Retardant Systems, NBSIR 75-741 (1975).

[46] Adams, K. M., Browner, R. F., Dagnall, R. M., and West, T. S., Anal. Chem. 42, 939 (1970).

[47] Miller, W. J., J. Chem. Phys. 57, 2354 (1972).

[48] Hayhurst, A. N. and Kittelson, D. B., Combust. Flame, 28, 301 (1977).

[49] Unsold, A., Physik der Sternatomospharen (Springer-Verlag, Berlin, 1938).

[50] Carabetta, R. and Kaskan, W., Eleventh Symp. (Intl.) Combust. (The Combustion Inst.), p. 331 (1967).

Discussion

Comment (Bradshaw): It is extremely important when doing comparisons between seeded and non-seeded techniques that great care be taken in ensuring that the seed species remain in a radially homogeneous volume such as that in a shielded flame where an isotropic environment is maintained around the inner seeded flame over the entire height measurement regime.

This will enable comparisons between seeded and non-seeded techniques without the problems associated with edge effects on line of sight seeded techniques.

Response (Hastie): This point is covered in the written version of this presentation. In actual fact no disparity was found between seeded and non-seeded data, e.g. compare the line reversal and OH-absorption data. Where disparate data did occur, this was between the integrated path length methods (reversal and OH) and the point source Raman technique.

Appendix B

Temperature Profiles of Inhibited Flames Using Raman Spectroscopy

M. C. Drake* and J. W. Hastie

National Bureau of Standards

Washington, D.C. 20234

Submitted to Combustion and Flame

*National Research Council Postdoctoral Fellow 1977-1978.

Present Address: General Electric Research & Development Center, Schenectady, New York 12301

Abstract

Laser Raman scattering from vibrational and rotational states of N_2 and H_2 has been used to determine temperature profiles for several $H_2/O_2/N_2$ flames with and without HBr present. The inhibiting effect of HBr is clearly demonstrated and the derived properties of burning velocity and inhibition index are in good agreement with previous experimental measurements and theoretical calculations.

1. Introduction

Combustion research is undergoing a period of rapid expansion as a result of current technological needs. These include efficient utilization of low grade fuels, minimization of air pollution sources, and chemical flame inhibition for fire prevention or control. Many such problem areas could benefit from a fundamental understanding of the chemical mechanisms, thermodynamics, and kinetics of the combustion process.[1,2] Considerable progress in developing this fundamental understanding has resulted in recent years from detailed microstructure investigations on laboratory scale premixed laminar flames[3]. Such flame structure studies rest on spatially resolved measurements of temperature and major species concentrations in all areas of the flame and, more critically, the concentrations of free radicals and other reaction intermediates in, or near, the primary reaction zone. These profile measurements provide a quantitative base for flame modeling calculations, from which reaction mechanisms and reaction rates may be deduced.

Detailed flame structure studies are particularly needed for development of mechanisms for gas phase flame inhibition*. The addition of small amounts (often less than 100 ppm) of inorganic compounds containing metals, halogens, or both, has a pronounced effect on flame microstructure, burning velocities, and flammability limits[1]. If the additives cause a decrease in burning velocity, for example, they are considered inhibitors. These changes can be related to changes in the spatial and temporal distribution of reactive free radicals[1,2]. As a result of many studies on flame inhibitors a consensus opinion on the detailed mechanisms involved has been

---

*E.g., see Brown, N. J., and Schefer, R. W., A Computational Study of Physical and Chemical Flame Inhibition, Western States Section, The Combustion Institute Paper No. 78-43, Boulder, Colorado, April 17-18, 1978.

established. This understanding has provided the theoretical basis for the development of an inhibitor index parameter which correlates the inhibition effects of a wide range of additives in a variety of flames[1].

We report here the first use of vibrational and rotational Raman spectroscopy in flame inhibition studies. Measured temperature profiles in premixed, atmospheric pressure flames of $H_2/O_2/N_2$, with and without the inhibitor HBr, are used to infer burning velocity changes and an HBr inhibition index. The results are in reasonable agreement with literature values and with current understanding of HBr gas phase flame inhibition mechanisms.

2. Experimental

2.1 Background

Most experimental combustion measurements, to date, have been made by physical probe techniques such as thermo-couples and microprobe or supersonic molecular beam sampling for mass spectrometry[1,3-5]. However, use of nonperturbing spectroscopic methods, and particularly those with lasers, is increasing[6-12]. One such method, laser Raman spectroscopy, was first applied to flames in 1972[6,7]. Since that time, vibrational Raman spectroscopy has become widely used as a diagnostic tool for measuring temperatures and molecular densities in combustion systems[3,8-12]. More recent work has emphasized the spatial resolution capability of the laser Raman technique to obtain, for instance, temperature profiles in $H_2/O_2/N_2$ flames[12], CH_4-air and propane-air flames[8]. Such data are particularly valuable since the spatial, and sometimes temporal, distribution of temperature are perhaps the most important quantities for characterizing a flame.

Some specific advantages of Raman spectroscopy for flame temperature profile studies include:

1) high spatial resolution (sample volumes ≤ 0.01 mm^3 are possible);

2) minimal flame perturbations because no physical probes are required; and

3) the ability to measure temperatures throughout the flame and particularly near the primary reaction zone.

Item (3) is particularly important since most other techniques for measuring flame temperatures are not applicable in, or near, the primary reaction zone. For example, chemiluminescent excitation of sodium in Na-D line reversal, radical recombination reactions on thermocouples, and non-Boltzman distributions in OH and other free radicals in emission spectroscopy can result in anomalous temperature values near the reaction zone of flames[12].

The principal disadvantages of Raman spectroscopy in combustion research stem from the relative weakness of the Raman effect. Because ordinary Raman scattering is a nonresonant process, it has a very low cross section and thus gives relatively weak signals even with high powered lasers. This makes the technique generally unsuitable for minor species concentration measurements in high temperature gases. For example, no unambiguous Raman signals have been reported from any free radicals in flames. Also, weak signal intensities make Raman spectroscopy susceptible to interferences from other sources of visible radiation, such as background flame luminosity and laser induced particulate scattering, incandescence, and fluorescence. However, these interferences are usually not severe for clean particulate-free laboratory-scale flames.

2.2 Apparatus and Flames

The Raman apparatus used in this study has been described elsewhere[12]. A high-powered cw argon ion laser (6W at 514.5 nm) is focused by a 60 mm focal length lens into the sample area of the flame. An 80 mm focal length mirror reflects the laser beam back into the sample area creating an external resonating cavity with the output mirror of the laser. A two-lens system collects light scattered at right angles to the incident laser beam and focusses it into a double monochromator. Another mirror directs the light scattered opposite to the collection lenses back along the collection optical axis to effectively double the observed signal. This total optical system produces a cylindrical sample volume element with dimensions of $\sim$ 0.1 mm diameter and 1.5 mm length.

The vertically burning flames emanate from a welding torch burner (2.97 mm i.d., 6.25 mm o.d.). A surrounding shield flow of N_2 gas prevents any significant air entrainment and secondary combustion. All gas flows are controlled by pressure regulators and measured by calibrated flow rotameters. The burner is mounted on x y z micrometer translators for accurate positioning. Flames of initial $H_2/O_2/N_2$ mole ratios of 4/1/4 and 3.4/1/2 were used and these are conventionally designated as U(4) and O(2), respectively[6,12]. All flames had the same combustion gas flow velocities (4.275 litre/min), torch head, and flow rate of nitrogen shield gas surrounding the central flame.

2.3 Spectra and Temperature Determination

The theory and application of relative Raman intensities for determining temperatures and molecular concentrations has been extensively discussed previously and will not be repeated in detail here[9-11]. Examples of spectra and the method of analysis used in the present study are given as follows.

2.3.1 N_2 Rotational Spectra

Figure 1 shows a typical Stokes rotational Raman spectrum, for the burnt gas region of a fuel-rich premixed $H_2/O_2/N_2$ flame at a temperature of 1988 K. A similar rotational Raman spectrum but from a much hotter flame (T = 2450 K), is shown in figure 2. The scattering in both of these spectra (figs. 1 and 2) is essentially entirely from N_2 molecules since the concentration of O_2 is very low above the primary reaction zone of these fuel-rich flames; H_2 is known to have a very small rotational Raman cross section relative to N_2[13,14]; and H_2 has rotational Raman peaks which generally occur at larger $\Delta\nu$ values than those shown in figures 1 and 2.

Note in the spectra of figures 1 and 2 that the 2:1 intensity alternation results from nuclear spin effects which occur in homonuclear diatomic molecules. Also of note in figure 2 is the appearance of additional low intensity peaks at the low $\Delta\nu$ side of the major peaks at $\Delta\nu > 200$ cm^{-1}. These side peaks are due to pure rotational transitions from vibrationally excited (primarily v = 1) levels of N_2[9,11].

All aspects of the spectra in figures 1 and 2 are in quantitative agreement with theoretical calculations based upon the accurately known energy levels of N_2. The separation δ of the $\nu = 0$ compared to the v = 1 peak for $J \rightarrow J + 2$ transitions
is given by:

$$\delta = 4(J_{lower} + 3/2)\ \alpha_e \qquad (1)$$

where J and v are the rotational and vibrational quantum numbers, respectively. For N_2, $\alpha_e = 0.01709$ cm^{-1}. Thus for $J < 30$, the δ separations are too small to be observed in the spectrum of figure 2. For $J < 30$, the observed separations increase with J, in agreement with eq. (1). The side peaks are not as visible in the spectrum of figure 1 because of the lower temperature and the lower spectrometer resolution used.

Rotational temperatures are calculated from the relative intensities of spectral peaks, such as those given in figures 1 and 2, according to established methods outlined in detail elsewhere[9] using the relationship:

$$\frac{-F_0 C_2}{T} = \ln \frac{I_s}{fs^1\nu^3 g} \qquad (2)$$

Here, F_o is the energy of the initial energy level; $c_2 = hc/k$; I_s is the measured Raman intensity, corrected for contributions from vibrationally excited molecules; fS' is the Raman line strength; ν is the scattered light frequency; and g is the nuclear degeneracy factor.

The measured intensities of all peaks, typically numbering at least 50, are used simultaneously for temperature determination by application of an iterative computer program, as described in detail elsewhere[9,11]. For example, analysis of the spectrum in figure 1 gives a calculated temperature of 1988 ± 28 K. The error is taken as ± 2 standard deviation statistical uncertainties, as calculated by a computerized linear least squares technique. This probably underestimates the true error limit ($\sim$ ± 50 K) because of the uncertainty associated with correcting for vibrationally excited rotational transitions[9,11].

2.3.2 H_2 Vibrational Spectra

Vibrational Raman spectra from H_2 and N_2 were also observed in this study at much larger Raman shift values. Typical H_2 Stokes vibrational Raman spectra, one obtained in the pre-flame region (z = 3.4 mm) and the other in the burnt gas region (z = 6.9 mm), of a U(4) flame are shown in figure 3. The spectral peaks are due to Q branch transitions (v = 0, J → v = 1, J) and the profiles are in accord with theoretical

prediction[10]. Note that with increasing temperature the intensities of the high J transitions are enhanced relative to those for the low J transitions.

Hydrogen rotational temperatures were calculated using eq. (2) in a similar manner to that used for N_2, with the following exceptions. Different line strength and degeneracy factors were applied and no corrections were necessary for transitions from vibrationally excited molecules. Fewer transitions were analyzed in the H_2 spectra (6 instead of $\sim$ 50 for N_2) and this accounts for the higher statistical uncertainties in the calculated temperatures.

2.3.3 N_2 Vibrational Spectra

Figure 4 gives an example of a N_2 vibrational Raman spectrum. Note that the Q branch lines are much more closely spaced than for H_2 owing to the smaller molecular constants (B_e and α_e) for N_2. Individual rotational lines are not resolved in the Stokes vibrational Raman spectra (see fig. 4). Temperatures were obtained from the N_2 vibrational Raman spectral profiles by comparing the measured peak intensity ratios with those determined by computer calculations of N_2 spectral profiles as a function of temperature, as discussed in detail elsewhere[9,10].

3. Results and Discussion

3.1 Temperature Profiles

Temperature profiles, measured along the center line (z-axis) of vertically burning torch flames, with three different initial mole ratios, are shown in figures 5 and 6. Temperatures in the preflame region were

measured from Stokes H_2 vibrational spectra (e.g., fig. 3) with statistical errors of ± 5 K (statistical deviation ±1 σ). For the reaction zone and burnt gas regions, temperatures were measured using both N_2 and H_2 vibrational Raman spectra. The N_2 vibrational spectra for the U(4) flame gave more accurate temperatures (estimated ± 1σ errors of ± 50 K) than the H_2 vibrational spectra (± 75K). Temperature errors using the H_2 vibrational spectra were much larger for the O(2) flame (± 200 K) due to the presence of interfering H_2O flame emission lines which were much stronger in the hotter O(2) flame than the U(4) flame.

Temperatures measured near the flame reaction zones were susceptible to relatively large errors. Because of the characteristic triangular shape of the reaction zone for torch flames, the sample volume includes regions of very different temperature. However, temperature gradients in the preflame and burnt gas regions are much smaller and the temperatures more accurate. Temperatures based upon vibrational Raman scattering from N_2 and H_2 in these regions are in agreement, within experimental error. The vibrational temperatures were checked at a few locations in the burnt gas region by use of the more accurate N_2 rotational Raman spectra and the agreement was within experimental error. For example, in the U(4) flame, two independent rotational Raman spectra (one shown in fig. 1) gave calculated temperatures of 1988 ± 14 K and 1987 ± 14 K, while N_2 vibrational spectra yielded a temperature of 1960 ± 40 K at the same position in the U(4) flame.

The O(2) flame temperature profile shown in figure 5, reached a maximum value of 2420 K at a height of 10 mm. The U(4) flame has a markedly different profile -- reaching its maximum value of 2005 K over a broad height range of 33-40 mm and then slowly decreasing again (not shown in fig. 5).

Figure 6 shows the effect of added HBr on the temperature profile for the U(4) flame. The effect of adding HBr to the U(4) flame was to shift the position of initial temperature rise downstream from the burner face. However, the position of maximum temperature, which occurs in the region of z = 10 mm (not shown in fig. 6), is closer to the burner face.

The importance of the N_2 shield flow in reducing air entrainment is demonstrated as follows. For the U(4) flame at z = 39 mm the temperature derived from N_2 vibrational Raman spectra (see fig. 4), was 2160 K without the N_2 shield as compared with 2005 K for the shielded flame. This former value is well above the calculated adiabatic flame temperature of 2019 K and is indicative of serious air entrainment and secondary combustion effects in the burnt gas region for an unshielded fuel-rich flame.

Adiabatic flame temperatures were calculated for these gas mixtures using a free energy minimization computer program implemented by Gordon and McBride[15]. The calculated adiabatic temperatures were 2019, 2016, and 2525 K for the U(4) flame, U(4) flame with 0.005 mole fraction HBr added, and for the O(2) flames, respectively. For the $H_2/O_2/N_2$/HBr systems the thermodynamic data for reactants, products, and intermediate species are sufficiently accurate that the uncertainty in calculated temperature should not exceed one Kelvin. The small differences between measured maximum flame temperatures and calculated adiabatic temperatures of 14 K, 6 K, and 105 K, respectively, for the different flames, indicate that heat losses to the burner are small.

3.2 Inhibition Effect of HBr

Comparison of the measured temperature profiles for the U(4) flame with and without HBr, is consistent with two important aspects of kinetically-based gas phase flame inhibition. First, flame inhibitors added

in small amount have virtually no effect on the flame thermodynamics or chemical equilibria. This is evidenced by the agreement, within experimental error, between the observed and calculated maximum temperatures for the U(4) flame with and without HBr. Second, chemical flame inhibitors strongly influence kinetically-controlled flame properties, including temperature profiles (see fig. 6), by altering the free radical concentration profiles[1,17]. Halogen containing flame inhibitors are believed to affect free radical profiles in two ways[1,17]. In the preflame region, flame inhibitors reduce the concentration of reactive free radicals such as H atoms, replacing them with less reactive free radicals through reactions such as:

$$H + HBr \rightarrow H_2 + Br.$$

This loss of flame propagating radicals tends to delay or shift the reaction zone downstream, as may be seen in figure 6. The reaction zone is approximately located about the position of maximum temperature gradient. A more definitive location of the reaction zone can be obtained from the relationship of Van Tiggelen[16,17] which yields a mean value for the flame front temperature:

$$T_r = T_i + 0.74\ (T_m - T_i) \qquad (3)$$

where T_i = initial gas temperature (320 K), and T_m = maximum observed flame temperature. In the reaction zone and the immediate downstream region HBr, and other halogen containing flame inhibitors, increase three body radical recombination rates through reactions such as:

$$H + Br + M \rightarrow HBr + M.$$

Such highly exothermic processes can result in a faster temperature rise in inhibited flames and this may be responsible for the position of maximum temperature being closer to the burner in the inhibited flame, that is at $z = 10$ mm as compared with $z = 33$-40 mm in the uninhibited U(4) flame.

Using the reaction zone location, we can estimate the burning velocity S_u from the relation[18]:

$$S_u = U \sin(\beta/2), \tag{4}$$

where U is the unburnt gas flow velocity (1027 cm/sec), β is the apex angle of the cone shaped reaction zone -- calculated from the burner width and the distance from burner to reaction zone z_r. The flame width at the burner is taken to be equal to the inner diameter of the burner tube (0.297), plus a small amount of flame overhang, estimated as 0.008 cm from the data of Smith and Pickering[29] (see their fig. 11). For the U(4), U(4) with HBr, and O(2) flames, z_r = 6.0, 7.4, and 2.5 mm, respectively, as determined from eq. (3) and figures 5 and 6. The calculated burning velocities are listed in Table 1. The small difference between the data in Table 1 and the literature values can be attributed to the approximate nature of expressions (3) and (4), experimental temperature error near the reaction zone due to non-isothermal Raman sample volumes, and uncertainties in the literature values (estimated 20 percent). These differences are not significant for the present study where the changes that occur on HBr addition are the primary concern.

The effectiveness of chemical inhibitors in premixed flames can be evaluated by means of a dimensionless index ϕ[17] defined by:

$$\phi = ([O_2]/[I])\Delta S_u/S_u \tag{5}$$

where $[O_2]$ and [I] are the concentrations of oxygen and chemical inhibitor, respectively; S_u is the burning velocity of the uninhibited flame; and ΔS_u is the change in burning velocity as a result of inhibitor addition. Although absolute burning velocities are difficult to measure[17,19], determination of inhibitor indices are easier because they involve ratios of burning velocities (see eq. 5) which tends to cancel many of the possible sources of error.

From the present data, $\phi = 3.8$. For a flame of similar composition, but with much larger amounts of HBr present, Miller et al.[21] measured a burning velocity change equivalent to $\phi = 2.2$. Considering the possible nonlinearity of equation (5) over large inhibitor concentration differences, and thedifferent stoichiometric ratios of 1.90 and 1.75 between the present data and that of Miller, et al.[21], respectively, the two sets of data are in good agreement. A further independent test of the present data is given by the very recent kinetic modeling calculations of Dixon-Lewis for HBr inhibited $H_2/O_2/N_2$ flames[22]. These calculations yield (see figs. 1 and 3 of ref. 22) the same type of temperature profile behavior as that indicated in figure 6.

4. Summary

Raman scattering (both rotational and vibrational) is shown to be capable of measuring temperature profiles for flame structure studies of low luminosity flames, with or without the presence of a chemical inhibitor. The technique, because of its high spatial resolution and ability to measure temperatures in all areas of the flame, offers some important advantages for flame structure and inhibition studies. The temperature profiles lead to derived flame properties, i.e., burning velocity and HBr inhibition index that are in good agreement with literature data.

Acknowledgments

The authors wish to acknowledge the assistance of Dr. D. W. Bonnell for computer calculations of adiabatic flame temperatures and the design of the burner modification for the N_2 shield flow. Support from the Army Research Office, Durham, N.C., is also acknowledged.

References

1. Hastie, J. W., High Temperature Vapors: Science and Technology, Academic Press New York (1975).

2. Gann, R. G., (Ed.), Halogenated Fire Suppressants, ACS Symposium 16, Am. Chem. Soc., Washington, D.C. (1975).

3. Hastie, J. W. (Ed.), Characterization of High Temperature Vapors and Gases, NBS SP-561, U. S. Govt. Printing Office, 1979.

4. Zinn, B. T. (Ed.), Experimental Diagnostics in Gas Phase Combustion Systems, Amer. Inst. Aero. and Astro., New York (1977).

5. Goulard, R., Combustion Measurements -- Modern Techniques and Instrumentation, Academic Press, New York, 1976.

6. Lapp, M., Goldman, L. M., and Penney, C. M., Science, 175, 1112 (1972).

7. Vear, C. J., Hendra, P. J., and McFarlane, J. J., J. Chem. Soc., Chem. Commun., 381 (1972).

8. Stephenson, D. A., Proc. of 17th Int. Comb. Symp., Leeds, England, August 1978.

9. Drake, M. C., and Rosenblatt, in ref. 3.

10. Lapp, M., and Penney, C. M., in Adv. in Infrared and Raman Spectrosc., R. J. H. Clark and R. E. Hester, eds. (Heyden and Sons, Ltd., London, 1977), vol. 3, Chapter 6.

11. Drake, M. C., and Rosenblatt, G. M., Comb. Flame, 33, 179 (1978).

12. Drake, M. C., Grabner, L., and Hastie, J. W., in ref. 3.

13. Penney, C. M., and Lapp, M., J. Opt. Soc. Am., 66, 422 (1976).

14. Murphy, W. F., J. Chem. Phys., 67, 5877 (1977).

15. Gordon, S., and McBride, B. J., NASA SP-273, NTIS Document No. 71 37775 (1971).

16. Burke, R., and Van Tiggelen, A., Bull. Soc. Chim. Belges, 74, 426 (1965).

17. Fristrom, R. M., and Van Tiggelen, P. J., 17th Int. Comb. Symp., Leeds, England, August 1978, to be published, Combustion Institute.

18. Gaydon, A. G., and Wolfhard, H. G., Flames--Their Structure, Radiation, and Temperature, 3rd Ed., Chapman and Hall, Ltd., London (1970) pp. 60.

19. Smith, F. A., and Pickering, S. F., J. Res. Natl. Bur. Strds. 17, 7 (1936).

20. Lewis, B., and von Elbe, G., Combustion, Flames, and Explosions of Gases (Academic Press, New York, 1951) p. 460.

21. Miller, D. R., Evers, R. L., and Skinner, G. B., Combust. Flame, 7, 137 (1963).

22. Dixon-Lewis, G., Combustion Flame 36, 1 (1979).

Table 1. Comparison of Measured Flame Properties With Literature Values

	U(4)	U(4) + 0.005 HBr	O(2)
T_{max}	2005 K	2010 K	2420 K
$T_{adiab.}$	2019 K	2016 K	2525 K
$z(T_{max.})$	33-40 mm	10 mm	10 mm
z(reaction zone)	6.0 mm	7.4 mm	2.5 mm
S_u(measured)	261 cm/sec	216 cm/sec	520 cm/sec
S_u(ref. 20)	267 cm/sec	------	425 cm/sec

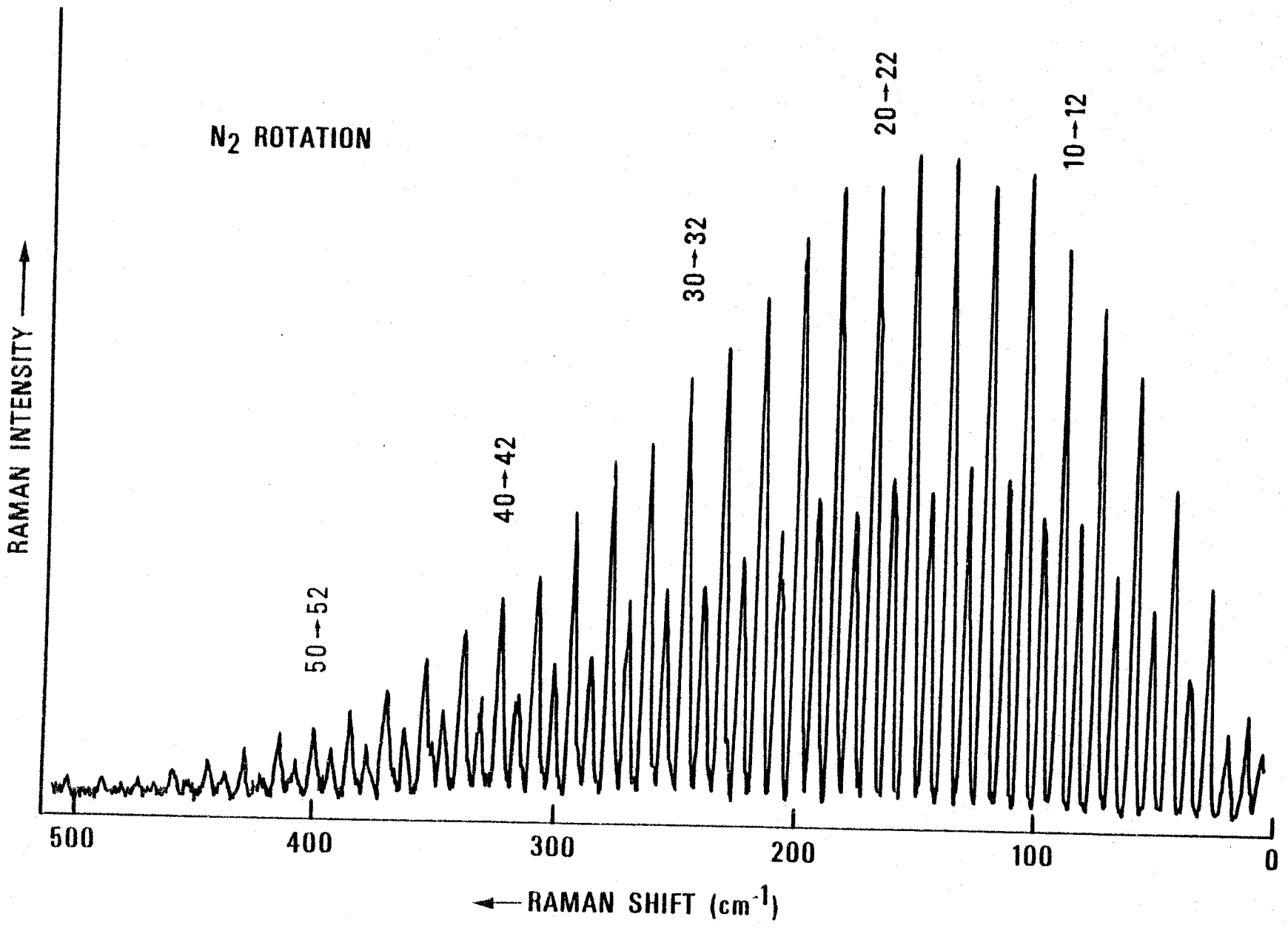
N2 ROTATION
RAMAN INTENSITY
50→52
40→42
30→32
20→22
10→12
500
400
300
200
100
0
RAMAN SHIFT (cm-1)

Figure B.1.

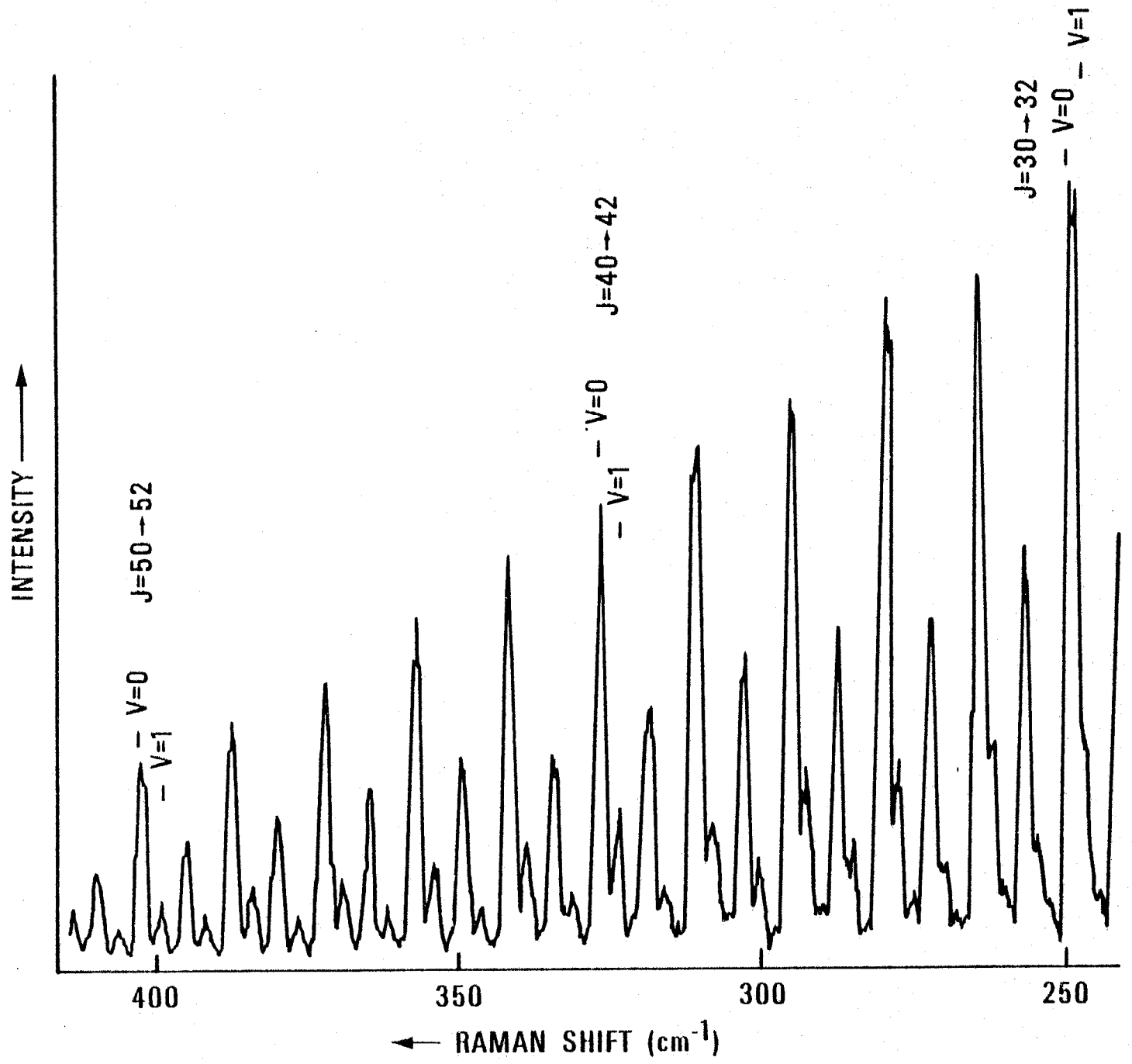
INTENSITY
J=50→52
V=0
V=1
J=40→42
V=0
V=1
J=30→32
V=0
V=1
400
350
300
250
RAMAN SHIFT (cm⁻¹)

Figure B.2.

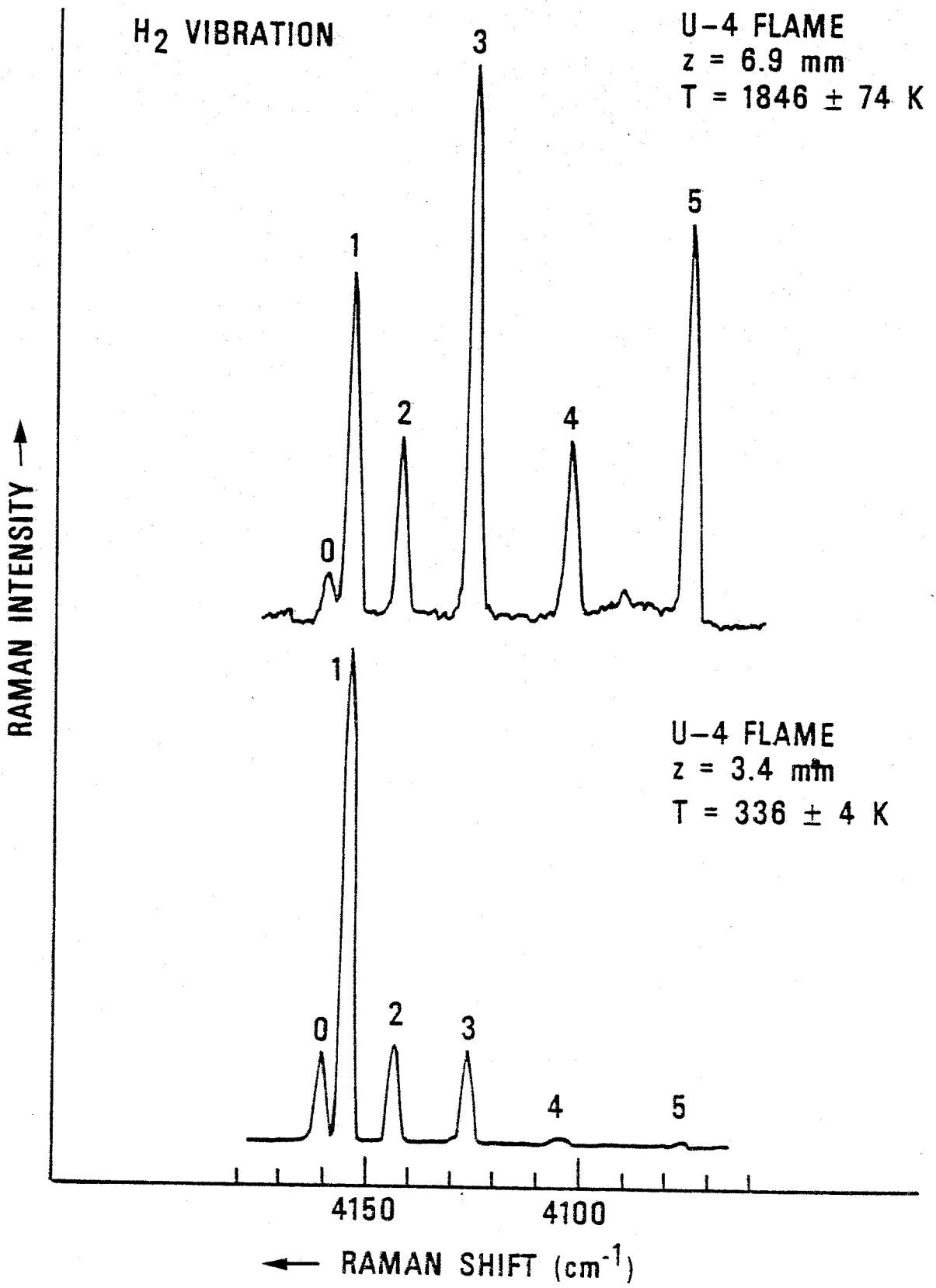
H_2 VIBRATION
U–4 FLAME
z = 6.9 mm
T = 1846 ± 74 K
U–4 FLAME
z = 3.4 mm
T = 336 ± 4 K
RAMAN INTENSITY
4150
4100
RAMAN SHIFT (cm^{-1})

Figure B.3.

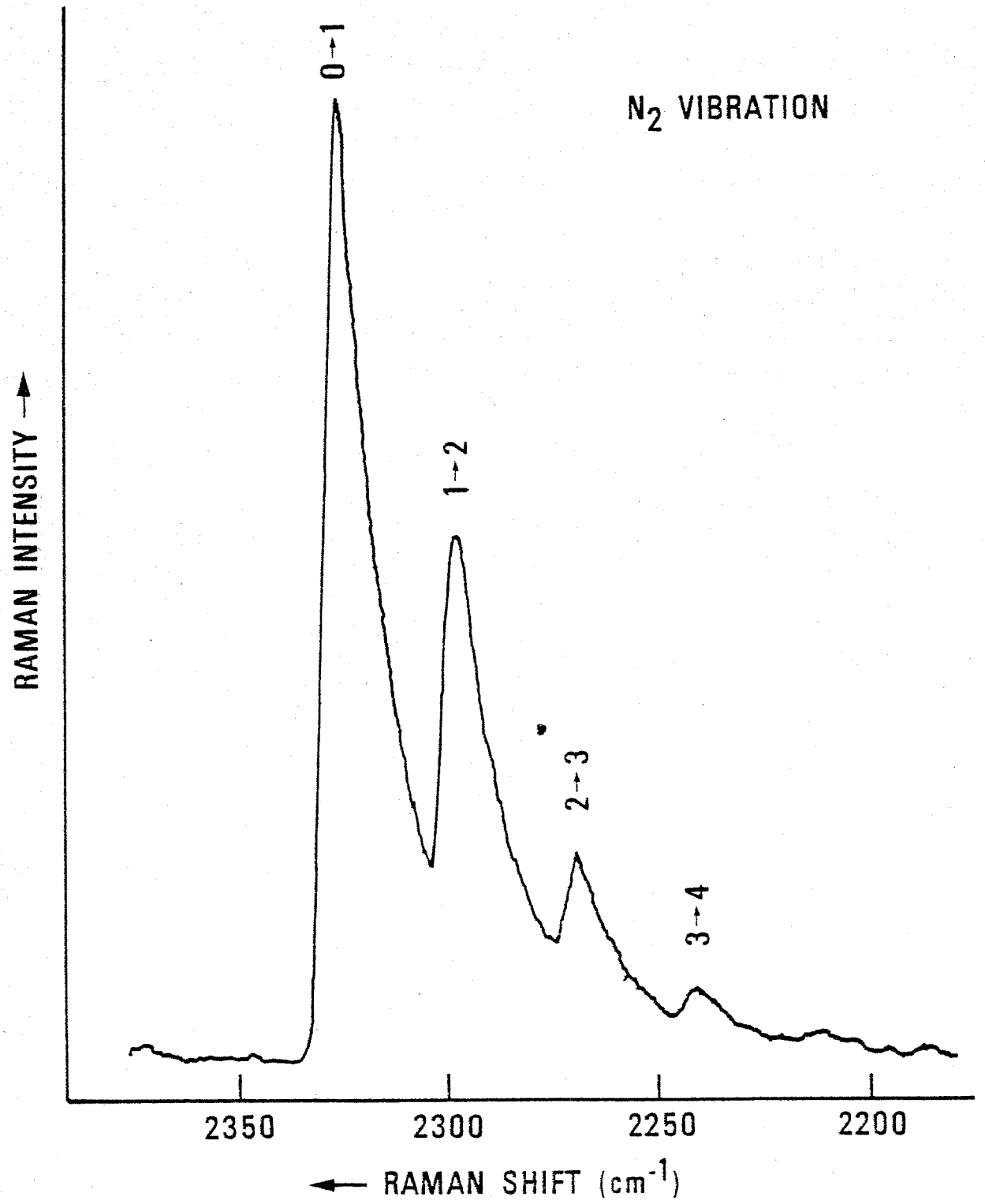
0→1
1→2
2→3
3→4
N2 VIBRATION
RAMAN INTENSITY →
2350
2300
2250
2200
← RAMAN SHIFT (cm-1)

Figure B.4.

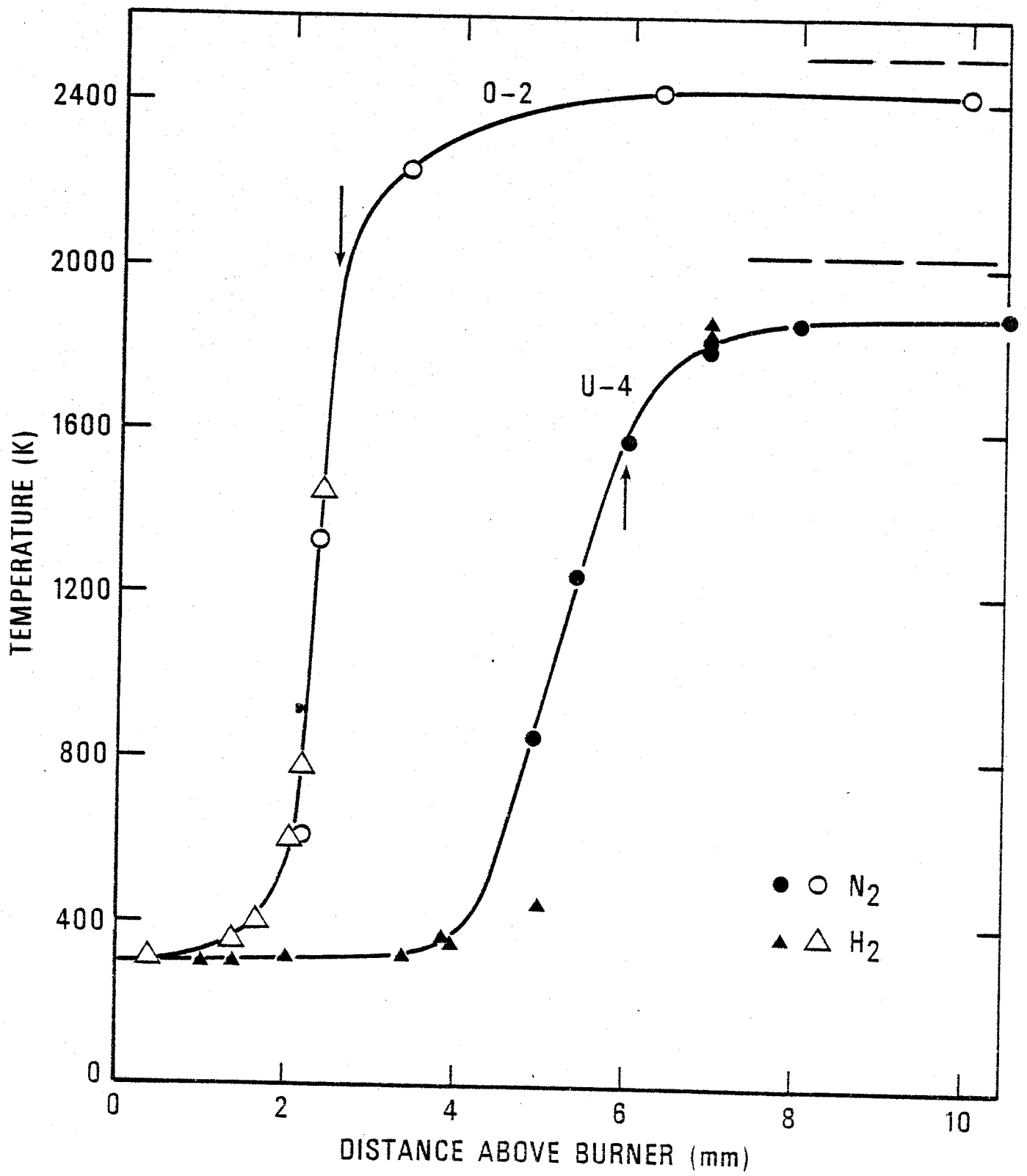
2400
2000
1600
1200
800
400
0
TEMPERATURE (K)
0-2
U-4
N_2
H_2
0
2
4
6
8
10
DISTANCE ABOVE BURNER (mm)

Figure B.5.

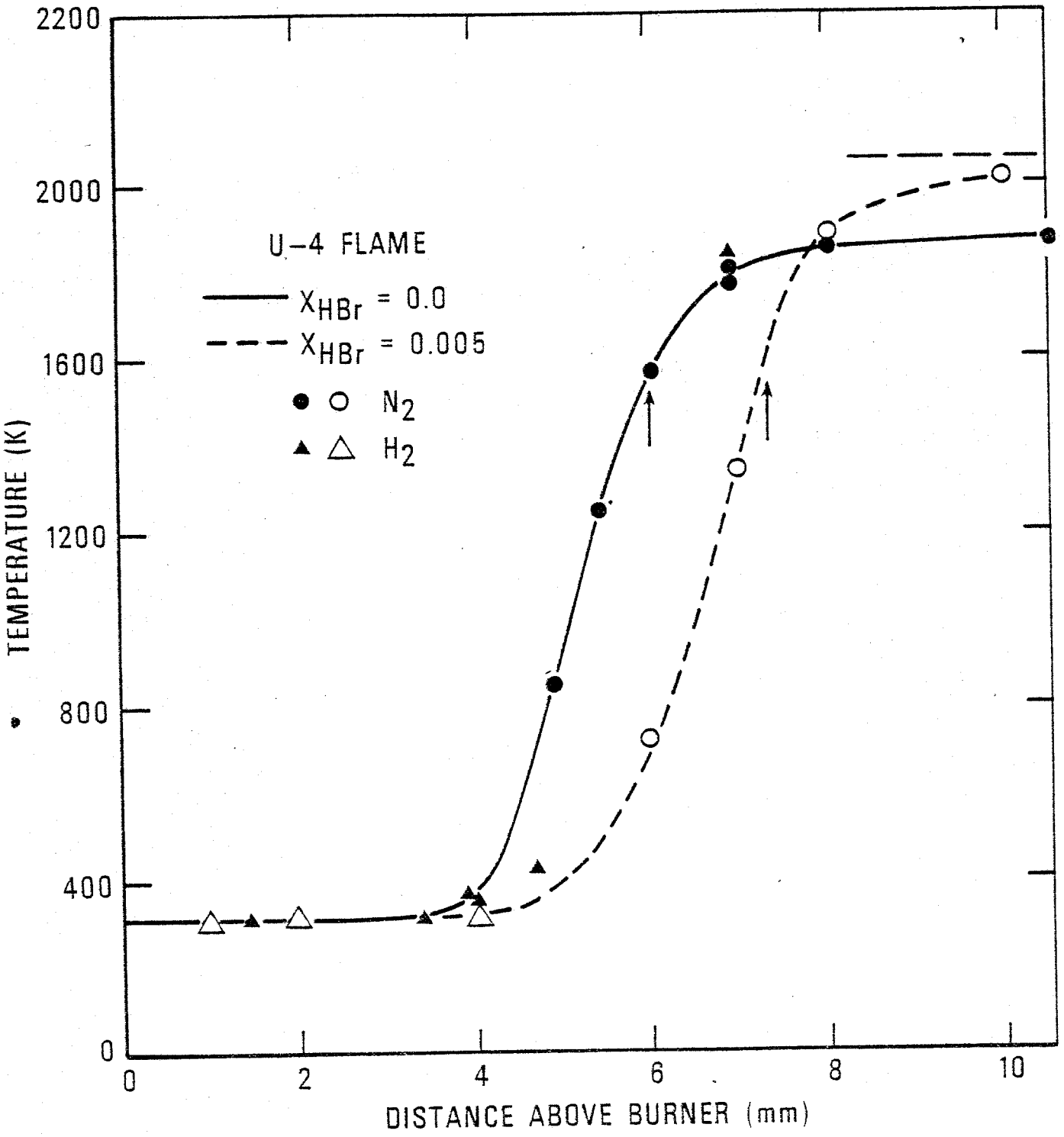
2200
2000
1600
1200
800
400
0
TEMPERATURE (K)
U-4 FLAME
X_{HBr} = 0.0
X_{HBr} = 0.005
N_2
H_2
0
2
4
6
8
10
DISTANCE ABOVE BURNER (mm)

Figure B.6.

Figure Captions

Figure 1 Stokes rotational Raman spectrum from a U(4) flame ($H_2/O_2/N_2$ = 4/1/4) with a N_2 flame shield. Height above burner is z = 29 mm. T = 1988 ± 14 K. The peak labeling refers to the initial and final rotational quantum numbers for the rotational transitions of N_2.

Figure 2 Segment of Stokes rotational Raman scattering from an O(2) flame ($H_2/O_2/N_2$ = 3.4/1/2). Peaks due to pure rotational transitions from ground state and the first excited vibrational state of N_2 are observed. T = 2450 K.

Figure 3 Stokes vibrational Raman scattering from N_2 in a U(4) flame with a N_2 shield. Lower spectrum obtained from preflame region at z = 3.4 mm yielding T = 336 ± 4 K; upper spectrum obtained from burnt gas region at z = 6.9 mm, yielding T = 1846 ± 74 K. Labels refer to rotational quantum number of transition.

Figure 4 Stokes N_2 vibrational Raman spectrum obtained from the burnt gas region at z = 39 mm, of an unshielded U(4) flame and yielding and T = 2160 ± 50 K. Labels indicate the vibrational quantum numbers of the transitions.

Figure 5 Temperature profiles for U(4) and O(2) flames measured along the central z axis of gas flow. The horizontal dashed lines represent the calculated adiabatic flame temperatures. Arrows indicate the calculated median location of the reaction zone.

Figure 6 Flame temperature profiles for the U(4) flame, obtained along the central z axis, showing the effect of 0.005 mole fraction added HBr. The horizontal dashed line represents the calculated adiabatic flame temperature. Arrows indicate the calculated median location of the reaction zone.

Appendix C

Vertical High Pressure Sampling Mass Spectrometric System

D. W. Bonnell and J. W. Hastie

A second High Pressure Sampling Mass Spectrometer System (HPMS) was designed and constructed with the ultimate goal of permitting molecular level analysis of gaseous and liquid fueled diffusion flames, and to generally upgrade the HPMS technique, according to the design goals listed below. These flames would closely simulate the conditions existing in the fuel-fire problem. Their characterization would permit one to validate and extend the flame inhibition models developed from premixed flame studies, such as those contained in the body of this report.

The following discussion summarizes, briefly, the main features of this apparatus and a more detailed description will appear elsewhere when the operating parameters have been fully characterized.

Design Goals Pertinent to Current Research Objectives

1. To provide a vertical sampling orientation, thus allowing investigation of dynamically weak diffusion flame systems.
2. To permit the use of a substantially larger sampling orifice, (e.g., 20 mil versus current 3 mil diameter) thus reducing the orifice plugging problem characteristic of smokey flames.
3. To allow the use of independently pumped free jet expansion and beam extraction regions, leading to improved beam intensity.
4. To provide independent pumping of the beam modulation region and provide variable distance and frequency modulation to allow for improved sensitivity and phase spectroscopic analysis (i.e., time-of-flight analysis for molecular beam).

5. To improve the high vacuum cleanliness over that for the existing HPMS system through use of an all stainless steel bakeable system.

6. To provide for both cross beam and axial mass analyzer positioning.

Implementation

To meet these design goals, a four stage, multiply differentially pumped vacuum system was designed, as shown in figure C.1. The numbered stages in the figure indicate the regions of free jet expansion and beam formation (I), beam collimation (II), beam modulation (III) and beam ionization-mass analysis (IV).

To meet the design goal of more than an order of magnitude increase in gas handling capability, it was necessary to maximize the stage I conductance through a novel design combining rectangular geometry, an integral infinite conductance valve and extreme close coupling between stages. The calculated conductance for this geometry is 1400 l/s, allowing effective use of pumps with speeds of $4\text{-}100 \times 10^3$ l/s, or more. A stage I vacuum equivalent to a pressure of about 10^{-6} atm is required for an optimum mean free path length of 5 cm. To meet this requirement, an ejector-type vapor booster pump was selected (Edwards model 18B4, 400 l/s, 600 sccm at 10^{-6} atm). The potential gas throughput was increased to 5000 sccm by placing a Roots blower in series with the booster and mechanical backing pump.

The second stage (II) pumping capacity was designed to complement the stage I performance, providing up to a hundred-fold pressure reduction with a 10 in. diffusion pump (currently using a 6 in. pump).

Stage III was designed to use oil-free pumps, and a combined turbo and cryopump system was installed for this purpose. The chopping system was designed to allow for a factor of two variation in modulated beam path length with an operating frequency range of 40:1, thereby permitting true phase spectroscopy of the neutral beam.

Stage IV contains an Extra Nuclear quadrupole mass analyzer[1], shown in the cross beam orientation. Axial mounting is also possible. In both orientations, full tri-axis alignment positioning allows for optimum beam alignment with the ionizer. An ion pump, providing permanent gas pumping capacity is augmented by a 1000 l/s cryopump.

Each interstage valve provides vacuum tight closure and rapid operation in the case of sampler failure. The shutters are stainless steel worm gear driven plates. Each shutter has provision for up to ten operating positions, which can be adjusted to better than 0.04° of arc, or 1 μm. This allows effective use of orifice collimation as small as 0.33 mm. Provision is also made for mounting a skimming device on the Stage I-II wall with manual adjustment of the skimmer-orifice distance.

Performance Tests

Vacuum and beam formation tests were performed using a standard flame sampling rig. At room temperature, orifices as large as 0.020" (0.05 cm) with a gas load of 3000 sccm could be used with the following pressures, for 0.47 cm interstage orifice diameters:

P_I--1×10^{-5} atm (foreline pressure 400 torr)

P_{II}--7×10^{-8} atm

P_{III}--6×10^{-9} atm

P_{IV}--1.5×10^{-9} atm

Preliminary sensitivity limit tests indicated a factor of 50 improvement over the two stage HPMS system. As the beam formation process is the same for both systems, this improvement is due primarily to better collimation and a cleaner vacuum system. We expect a sensitivity of better than 5 ppm in the VHPMS when the final pumping stages and a new multiplier are installed.

[1]Designation of commercial instrumentation does not imply endorsement by NBS, nor that it is the best available.

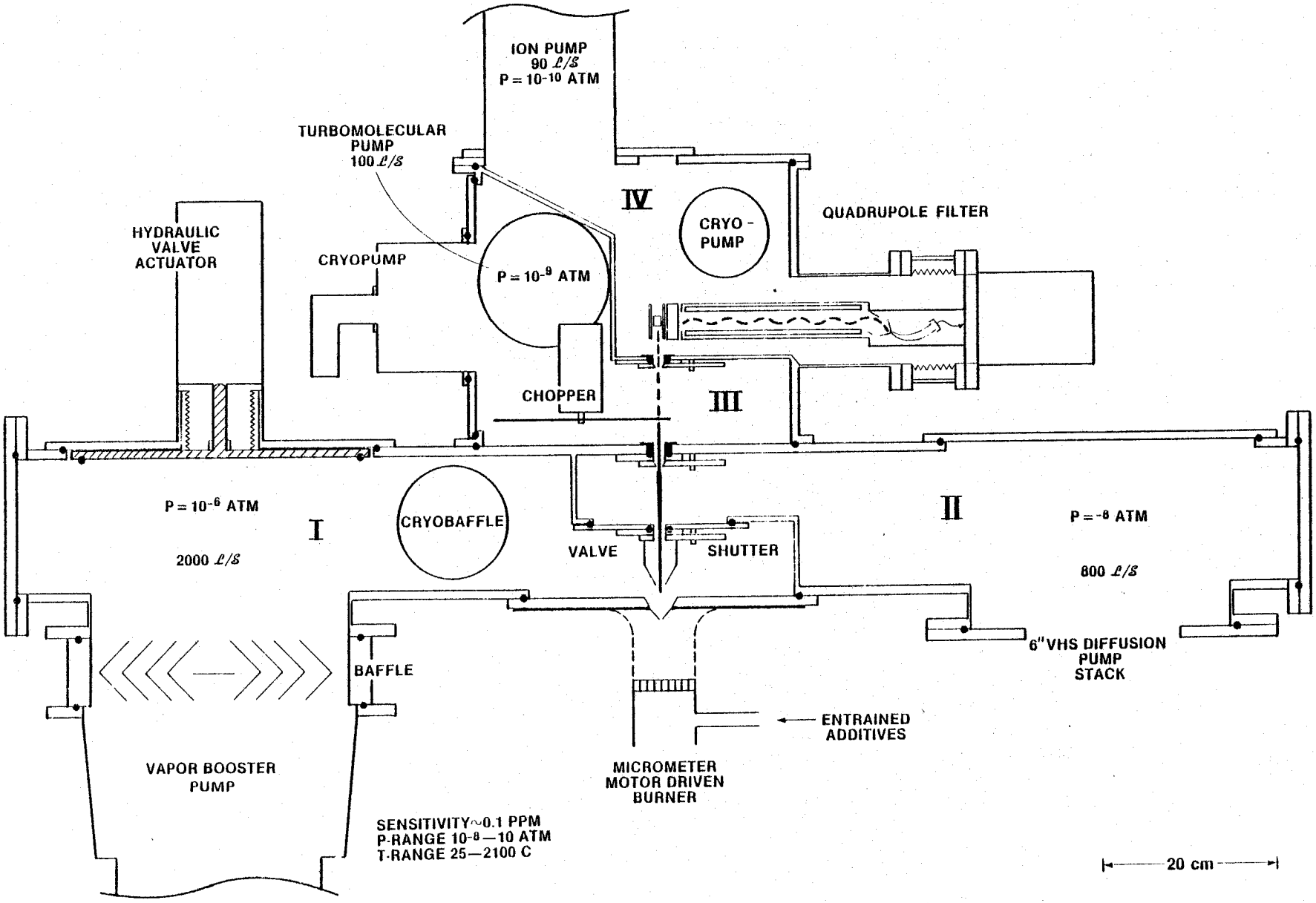

Figure C.1.

Vertical High Pressure Sampling Mass
Spectrometer System

Appendix D

Evidence for Formation and Thermochemistry of HPO_2, $NaPO_x$, and $LiPO_x$ (x = 2 and/or 3) Flame Species

J. W. Hastie and D. W. Bonnell

1. HPO_2 Thermochemistry

Mass spectrometric evidence for the presence of HPO_2 as a major flame species has been given in the body of this report (see fig. 5 and table 2). In order to determine the role of HPO_2 in the inhibition/promotion process, accurate thermodynamic enthalpy and entropy functions are needed. From analogy with HBO_2, HNO_2 and other oxy-hydroxide species, we can estimate, with reasonable accuracy, the structural and spectroscopic (mainly vibrational frequencies) parameters needed to calculate, statistically, the entropy and related functions. These data are summarized in Appendix E. (table E.3).

The standard heat of formation is a more critical, and difficult to estimate, function; thus three independent procedures (two experimental) were used for its determination.

a. Bond Additivity Approximation: For high temperature species, one can reliably correlate M-OH bond energies with the corresponding M-F values (Hastie, 1975, p. 291). From this correlation, and with HPO_2 bonding of HO-P = O), we have:

$$D(P - OH) = 0.83\ D(P - F)$$

$$= 99.9 \pm 3 \text{ kcal/mol} .$$

Hence,

$$\Delta H_{f,298}HPO_2 = \Delta H_{f,298}\ OH + \Delta H_{f,298}PO - D(P - OH)$$

$$= -96.0 \pm 6 \text{ kcal/mol} ,$$

relative to $\Delta H_{f,298}PO = -5.5 \pm 3$ kcal/mol (see Appendix E).

b. Knudsen Effusion Mass Spectrometry: Details of this work will appear elsewhere[1]. Basically, $V_3P(s)$ was used as a source of P_2 for reaction with H_2O vapor, giving the equilibrium:

$$1/2P_2 + 2HPO_2 = H_2O + 3PO \quad .$$

From mass spectrometric observation of these species, the equilibrium constant was determined as,

$$K_p(1300\ K) = 10^{-4.5 \pm 1} \quad .$$

The third law method (with entropy functions given in Appendix E) then yields

$$\Delta H_{f,298}(HPO_2) = -96.7 \pm 6 \text{ kcal/mol , relative to,}$$

$$\Delta H_{f,298}PO = -5.5 \pm 3 \text{ kcal/mol} \quad .$$

c. Mass Spectrometric Flame Data: For the hotter flames, and at post-flame reaction flow times of greater than one millisecond, HPO_2 and PO are likely to be at equilibrium, as can be seen, for example, in figure 6 (see main text). The HPO_2/PO relative partial pressure data obtained under these conditions are summarized in table D.1. These data, when combined with calculated H and H_2O partial pressures, yield equilibrium constants for the reaction:

$$PO + H_2O = HPO_2 + H \quad .$$

The third law method then yields reaction enthalpies (see table D.1) from which the HPO_2 heat of formation can be derived,

$$\Delta H_{f,298}HPO_2 = -94 \pm 4 \text{ kcal/mol} \quad .$$

Values obtained by these three methods are in agreement, within experimental error, and the value selected for the thermodynamic data bank is

$$\Delta H_{f,298}HPO_2 = -96 \pm 4 \text{ kcal/mol} \quad .$$

[1]Hastie, J. W., and Bonnell, D. W., Mass Spectrometric Determination of HPO_2 Heat of Formation, to be published (1981).

If one uses the $\Delta H_{f,298}PO$ values of Drowart et al. (1972), this heat would be less negative by 4 kcal/mol. The selected value is also in good agreement with the indirect spectroscopic evidence of Davies and Thrush (1966), which indicates a lower limit value of -97 kcal/mol. However, Vanzee and Khan (1976) have questioned the spectroscopic assignment as being HPO_2.

Table D.1

HPO_2 Reaction Enthalpy From Flame Data

$H_2/O_2/N_2$	T (K)	HPO_2/PO[a]	H/H_2O[b]	K_p[c]	ΔH_{298}[d]
6.5/1/4.2	1600	0.1	1.87(-4)	1.87(-5)	23.7
3.1/1/4	2120	2.0 (-2)	5.3 (-3)	1.06(-4)	23.7
3.1/1/2.7	2340	5.26(-2)	1.64(-2)	8.62(-4)	17.3
				Average	21.4
				± 3.5 kcal/mol[e]	

[a]Mass spectrometric data given in table 2.

[b]Calculated by multicomponent equilibrium method using upgraded JANAF (1971) data base (see Appendix E). Note, optical measurements of H-partial pressures made on similar flames showed agreement with the calculated values.

[c]Equilibrium constant for reaction: $PO + H_2O = HPO_2 + H$.

[d]Third law reaction enthalpy (in kcal/mol) based on thermodynamic functions given in Appendix E.

[e]Statistical uncertainty.

2. Evidence of $NaPO_2$ Formation in Flames

In a number of instances, anomalous H-atom concentration data were obtained using the Li/Na method in the presence of phosphorus, e.g., see the B-curves of figures 7 through 11 in the body of this report. This was particularly noticeable for the stoichiometric $H_2/O_2/N_2$ = 2/1/2 flame, containing a relatively high concentration of phosphorus (see fig. 11). Here, the apparent promotion effect extended into the burnt gas region at locations, or flow times, where thermodynamic equilibrium should be reached and where only small additive effects should occur. This, and similar instances of apparently anomalous H-atom behaviour, were found to correlate with unusually large P-induced changes (factor of 2 to 3 reduction) in the Na emission intensity and, to a much lesser extent, the corresponding Li data.

Figure D.1 shows a correlation between loss-of-Na-emission and increased concentration of TMP. Under normal flame conditions, addition of TMP can lead to changes in the Na thermal emission intensity of about 30 percent for each 100 K change in temperature. Smaller variations could occur due to differences in burner input gas-flow conditions between experiments with and without phosphorus. Thus, these factors alone cannot explain the observed changes of up to 300 percent (shown in later figures). For the case of an inhibited flame, where the post flame temperature increases due to exothermic catalysed radical recombination processes and changes in thermal losses to the burner, Na thermal emission should increase. This is shown in figure D.1, where addition of 1.8×10^{-3} mole fraction of TMP to the $H_2/O_2/N_2$ = 3.7/1/2.1 flame increases the Na emission intensity, as expected for this inhibited flame. However, further TMP additions lead to progressive decreases in the Na emission intensities (see fig. D.1). This monotonic relationship between lost Na and added phosphorus is clear evidence of compound formation of the type NaPX,

where X may be O, H, N, separately or in combination. The species NaP can be shown to be thermodynamically unstable under these flame conditions. Also, P-H and P-N (other than P ≡ N) bond energies are too weak to allow NaPX formation, where X = H or N, under these conditions. Therefore, X most likely contains O-atoms, and one or more of the species NaPO, $NaPO_2$, or $NaPO_3$ are present in these flames.

There are insufficient thermodynamic data available for the species $NaPO_x$ (x=1-3) to make a priori predictions about their relative contributions in our flame systems. However, from the high stability of HPO_2, together with the known thermodynamic data for the analogous species HBO_2 and $NaBO_2$ (JANAF, 1971)[2], the pertinent thermodynamic functions for $NaPO_2$ can be estimated, as discussed in Appendix E. From these data we can calculate the likely equilibrium concentration of $NaPO_2$ in our flames. Typical data are given in figure D.2, where, for typical TMP concentration levels, $NaPO_2$ is predicted to be the predominant Na-containing species. Hence, we can account for the observed Na-losses entirely in terms of $NaPO_2$ formation. While this interpretation allows for a self-consistent analysis of our flame data, we cannot eliminate the alternative case involving $NaPO_3$, or a combination of $NaPO_3$ and $NaPO_2$ (and similarly for the Li case).

For the flame conditions represented in figure D.1, the predicted P-induced loss-of-Na-emission, by $NaPO_2$ formation, is in excellent agreement with experimental observations. Also, the one-to-one correspondence of this effect on TMP concentration supports the assumption of $NaPO_x$ (x=1-3) as the complex Na-P-containing species.

[2]For reference citations, see Section 6 in the body of this report.

Similar theoretical calculations have been made for representative Na emission intensity-versus-distance profiles used in the H-atom partial pressure determinations presented in the body of this report. These results, summarized in figures D.3 to D.8, show satisfactory agreement with the observed P-induced losses of Na-emission intensity. This agreement, obtained over a wide range of oxidizing conditions (fuel rich to lean flames), temperatures (1850 to 2650 K) and TMP concentrations, lends support to the theoretical interpretation and related thermodynamic data.

With this degree of confidence in species assignment, the experimental data can be used to refine, if necessary, the basic thermodynamic data estimated for $NaPO_2$. From the experimental data of figures D.3 through D.8, values of $R = NaPO_2/Na$ partial pressure ratio have been derived and summarized in table D.2. These data were obtained at flame locations where the H-atom partial pressure determinations indicated a thermodynamic equilibrium condition. Equilibrium constants can, therefore, be determined for the reaction:

$$Na + PO + 1/2O_2 = NaPO_2 \quad ,$$

using the experimental R-values together with calculated O_2 and PO partial pressure data. These data, listed in table D.2, are plotted in second-law form in figure D.9. Note the excellent agreement between the experimental and predicted data. Also, the lack of curvature in the log K_p vs T^{-1} relationship is further evidence that the most significant species have been accounted for.

Table D.2

Third Law Analysis of $NaPO_2$ and $LiPO_2$ Reaction[a] Enthalpy

Flame $H_2/O_2/N_2$	T[e] (K)	PO (atm)	O_2 (atm)	R_{Na}[c,e]	K_{Na}	$-\Delta H_{Na,298}$ kcal/mol	R_{Li}[c,e]	K_{Li}	$-\Delta H_{Li,298}$ kcal/mol
5/1/4.1	1850	1.83(-3)[d]	2.8 (-9)	2.1	2.1(7)	137.3	3.0	3.0(7)	146.3
1.8/1/4.3	2050	3.31(-5)	1.26(-2)	10.0	2.7(6)	143.8	5.2	1.4(6)	149.7
3.7/1/3	2200	4.0 (-3)	1.46(-6)	0.9	1.9(5)	142.9	1.0	2.1(5)	152.5
2/1/2	2370	1.88(-4)	5.0 (-3)	0.45	3.4(4)	146.3	---	---	---
2/1/2	2450	2.63(-4)	6.74(-3)	0.14	6.5(3)	140.1	---	---	---
2/1/2	2450	2.6 (-3)	2.46(-3)	1.1	8.5(3)	141.4	0.06	5.0(2)	138.9
0.53/1/0.8[b]	2650	1.98(-3)	1.48(-2)	1.1	4.5(3)	154.5	~0.1	~4.0(2)	153.0
					Average = 143.8 ± 5.5[f]			Average = 148.1 ± 5.8[f]	

[a] Reaction: $Na + PO + 1/2O_2 = NaPO_2$, and similarly for Li.

[b] $CH_4/O_2/N_2$ flame

[c] $R_{Na} = NaPO_2/Na$ partial pressure ratio in P-containing flame, and similarly for Li. $NaPO_2$ partial pressure is proportional to the emission intensity term:

$$Na_c - Na_p(\pm \Delta Na_T \pm \Delta Na_{NaOH}) \quad ,$$

where Na_c and Na_p are for the clean and P-containing flames, respectively; ΔNa_T represents the thermal emission change due to temperature changes on TMP addition; ΔNa_{NaOH} represents the change in free Na due to the NaOH partial pressure difference between the clean and P-containing flame.

[d] Computer terminology, e.g., $1.83(-3) = 1.83 \times 10^{-3}$.

[e] Experimental error bounds are given in figure D.9.

[f] From these data, $\Delta H_{f,298}NaPO_2 = -123.5 \pm 5.5$ kcal/mol and $\Delta H_{f,298}LiPO_2 = -115.2 \pm 5.8$ kcal/mol.

3. Evidence of $LiPO_2$ Formation in Flames

For inhibited flames, at temperatures of about 2000 K or more, the H-atom partial pressures reach their equilibrium values at burner distances of 1.5 cm or more, e.g., see figures 8 and 9 in the body of this report. Thus, for these conditions, the Li thermal emission-intensity-change on TMP addition should be small and primarily due to temperature changes. Also, for inhibited flames, it is usual for the temperature to increase with TMP addition and, hence, a corresponding increase in Li emission intensity should occur. However, the converse is observed as may be seen, for example, in figures D.6 and D.8.

From analogy with the corresponding Na data, it is reasonable to expect that this loss of Li is due to the formation of $LiPO_2$ and/or $LiPO_3$. Some conflicting literature evidence exists concerning the likely formation of these species. The species $LiPO_2$ is believed to form in the vapor phase over Li_3PO_4 at 1400 K, together with P_2 and Li_2O as dissociation products (Buchler and Stauffer, 1966). However, an independent and more extensive study assigns $LiPO_3$ as the major vapor species (Steblevskii and Alikhanyan, 1978). Under these conditions of chemical neutrality, gas saturation with respect to the condensed phase, and relatively low temperature, this is a reasonable species assignment. However, under our highly reducing flame conditions, the pentavalent species may be less prevalent. By analogy with the known stability trend for the species $NaBO_2$, $LiBO_2$, and HBO_2 (JANAF, 1971), a reasonable estimate can be made for the thermodynamic stabiltiy of $LiPO_2$ using the HPO_2 and $NaPO_2$ species for comparison, as described in Appendix E.

With these estimates, $LiPO_2$ is predicted to be a significant flame species, as may be seen, for example, in figure D.2. Note, however, that the more stable LiOH species dominates the distribution of Li in these flames. For this reason, it is experimentally more difficult to utilize the Li emission

data for verification of $LiPO_2$ formation. However, the Li emission intensity data-points, calculated on the basis of $LiPO_2$ formation, are within the experimental errors, as shown in figures D.3-D.8. Similarly, the reaction equilibrium constant data of figure D.9 are in good agreement with the predicted values. These data also yield reasonable reaction enthalpies, as shown in table D.2.

It is reasonable to expect production of $LiPO_3$ and, likewise, $NaPO_3$ under stoichiometric or lean flame conditions, but this seems to be precluded by the good agreement between the experimental and calculated data of figure D.9. The largest difference between experiment and calculation occurs for the $H_2/O_2/N_2$ = 2/1/2 flame at relatively high concentrations of TMP. Conceivably, part of this discrepency could indicate $LiPO_3$ formation. Further evidence supporting the thermodynamic prediction of $LiPO_2$ and $NaPO_2$ partial pressures is given by the good agreement between the corrected experimental and calculated equilibrium H-atom partial pressure data, which, for some flames, depends critically on the magnitude of $LiPO_2$ and $NaPO_2$ partial pressures. For example, see figures 7 through 10 in the body of this report.

We should stress that these indirect arguments concerning species identity are not indisputable, as numerous literature retractions have shown. Unequivocal mass spectrometric analyses are needed on these flames to establish the relative significance of $NaPO_x$ (x=1-3), and likewise for the Li case. However, the evidence of compound formation is clear even though it contradicts the analytical viewpoint that "no interference from compound formation occurs in a normal premixed flame" (see Dagnall et al., 1968). It is perhaps pertinent that compound formation is a known analytical problem in low temperature diffusion flames and the stability of the compounds formed (as condensed species) follows the trend,

$$Ca > Na > Li.$$

Appendix D

Figure Captions

D.1 Effect of TMP-addition on the Na resonance D-line emission (589.0 nm) intensity-versus-distance profiles for an inhibited $H_2/O_2/N_2$ flame. Curves 2-4 represent P-containing flames at the indicated TMP partial pressures. Beyond ~ 0.2 cm, each cm distance corresponds to a post flame gas flow time of about 1 ms and the post flame species should reach equilibrium at distances of 2 cm and greater. The large inverted triangles (on curves 3 and 4) represent the predicted loss of Na emission intensity due to $NaPO_2$ formation at thermodynamic equilibrium. These predicted values were obtained from the emission intensity-partial pressure relationship:

$$I^P_{Na} = I^C_{Na} (1 - X) \quad ,$$

where I^P_{Na} refers to the predicted emission intensity in the P-containing flame and I^C_{Na} is the corresponding observed value in the clean flame. X is a calculated partial pressure term defined by:

$$X = (P^C_{Na} - P^P_{Na})/P^C_{Na} \quad .$$

The parenthetical term is equivalent to:

$$P^P_{NaOH} - P^C_{NaOH} + P^P_{NaPO_2} \quad .$$

X is obtained by multicomponent equilibrium calculation of clean and P-containing flames. These calculations were made using the upgraded JANAF (1971) data base described in Appendix E. Also, from curve 2, a 25 K temperature increase is indicated on P-addition and this factor was included in the calculations for curves 3 and 4.

D.2 Calculated equilibrium partial pressures for alkali-containing species, as a function of total pressure of added TMP, for a typical experimental flame system. The upgraded JANAF (1971) data base was used for these calculations (see Appendix E). A similar plot for the major P-containing species has been given in the body of this report (fig. 24).

D.3 Na (589.0 nm) and Li (669 nm) emission intensity-versus-distance profiles with (closed symbols) and without (open symbols) TMP present for a relatively hot stoichiometric $H_2/O_2/N_2$ flame. These data were used to calculate the H-atom partial pressure-versus-distance profiles given in the body of this report (fig. 10), from which we can establish that the post flame species are equilibrated at distances greater than 2 cm. The large triangular points were calculated, assuming thermodynamic equilibrium and the formation of $NaPO_2$ and $LiPO_2$. For these calculations, the clean flame Na thermal emission intensity profile was used to define a more precise temperature profile than that obtained by the Na D-line reversal method, though this latter method was used to obtain an absolute reference temperature, at 1 cm, of 2550 K. The emission intensity-temperature relationship is given by,

$$I_{Na} \propto \exp(-24600/T) \quad .$$

Thus at 2 cm, T = 2520 K, 3 cm, T = 2350 K, and 4 cm, T = 2370 K. The upgraded JANAF (1971) data base was used for the thermodynamic calculations, including the new species and or thermodynamic functions for PO, PO_2, HPO, HPO_2, $NaPO_2$, and $LiPO_2$. (see Appendix E).

D.4 Na and Li emission intensity-versus-distance profiles for the same flame system (and notation) as for figure D.3, but with an order of magnitude increase in TMP concentration. These data were used to calculate the H-atom partial pressure-versus-distance profiles given in the body of this report (fig. 11). The large triangular symbols represent theoretical points, as discussed in the figure D.3 caption. The vertical bar on the theoretical Na(P) point represents the lower limit uncertainty resulting from a ± 50 K temperature error. In this flame, the following thermodynamic factors contribute to the Na (and Li) emission intensity profile changes on P-addition: a predicted 22 K temperature increase, an increase in H-atom partial pressure, a decrease in NaOH (and LiOH) partial pressure, and a loss of Na (or Li) due to $NaPO_2$ (or $LiPO_2$) formation.

D.5 Na and Li emission intensity-versus-distance profiles for a hot promoted $CH_4/O_2/N_2$ flame with (closed symbols) and without (open symbols) TMP present. For symbols terminology, see the figure D.3 caption. The post-flame temperature was estimated (±70 K error) from the calculated adiabatic flame temperature and an empirical heat-loss correction based on other temperature measurements with the same burner.

D.6 Na and Li emission intensity-versus-distance profiles for an inhibited fuel-rich $H_2/O_2/N_2$ flame with (closed symbols) and without (open symbols) TMP present. For symbols terminology, see the figure D.3 caption. From the corresponding H-atom partial pressure versus distance profiles given in the body of this report (fig. 8), the 3 cm post flame data should closely approach thermodynamic equilibrium.

D.7 Na and Li emission intensity-versus-distance profiles for an inhibited fuel-rich, relatively cool, $H_2/O_2/N_2$ flame with (closed symbols) and without (open symbols) TMP present. For symbols terminology, see the figure D.3 caption. These data were used to calculate the H-atom partial pressure-versus-distance profiles given in the body of this report (fig. 7), where it was established that the TMP-containing flame at 3 cm was at equilibrium.

D.8 Na and Li emission intensity-versus-distance profiles for an inhibited, lean, relatively cool, $H_2/O_2/N_2$ flame with (closed symbols) and without (open symbols) TMP present. For symbols terminology, see the figure D.3 caption. The error limit corrsponds to the following uncertainties: [P] ± 25 percent, T ± 50 K, $T_p - T_c$ ± 20 K, which correspond, respectively, to errors of ± 7 percent, ± 9 percent and ± 16 percent in the calculated value of $I^P_{Na} - I^C_{Na}$. These data were used to calculate the H-atom partial pressure-versus-distance profiles given in the body of this report (fig. 9), where it was established that the TMP-containing flame at 1.5 cm (∿ 1 ms) was at equilibrium.

D.9 Comparison of experimental and calculated partial pressure data for $NaPO_2$ and $LiPO_2$ expressed in equilibrium constant form, for the reaction:

$$Na + PO + 1/2\ O_2 = NaPO_2 \quad ,$$

and similarly for Li. The partial pressure ratios $NaPO_2/Na$, or $LiPO_2/Li$, were obtained from the observed reduction in alkali emission intensity on adding TMP to each flame, e.g., see figures D.3--D.8. These data were taken at a post flame location where the H-atom (and, hence, other flame species) partial pressure was known to have reached thermodynamic equilibrium. The error bounds, indicated for the experimental data points, represent the emission intensity and temperature uncertainties. In calculating the

experimental points, thermodynamic claculations of PO and O_2 partial pressures were used. The upgraded JANAF (1971) data base was used for all thermodynamic calculations (see Appendix E). The dashed curve indicates the effect of a reduction (i.e., less stable) in the value of $\Delta H_{f,298}{}^{NaPO_2}$ by 6 kcal/mol (i.e., to -117.6 kcal/mol).

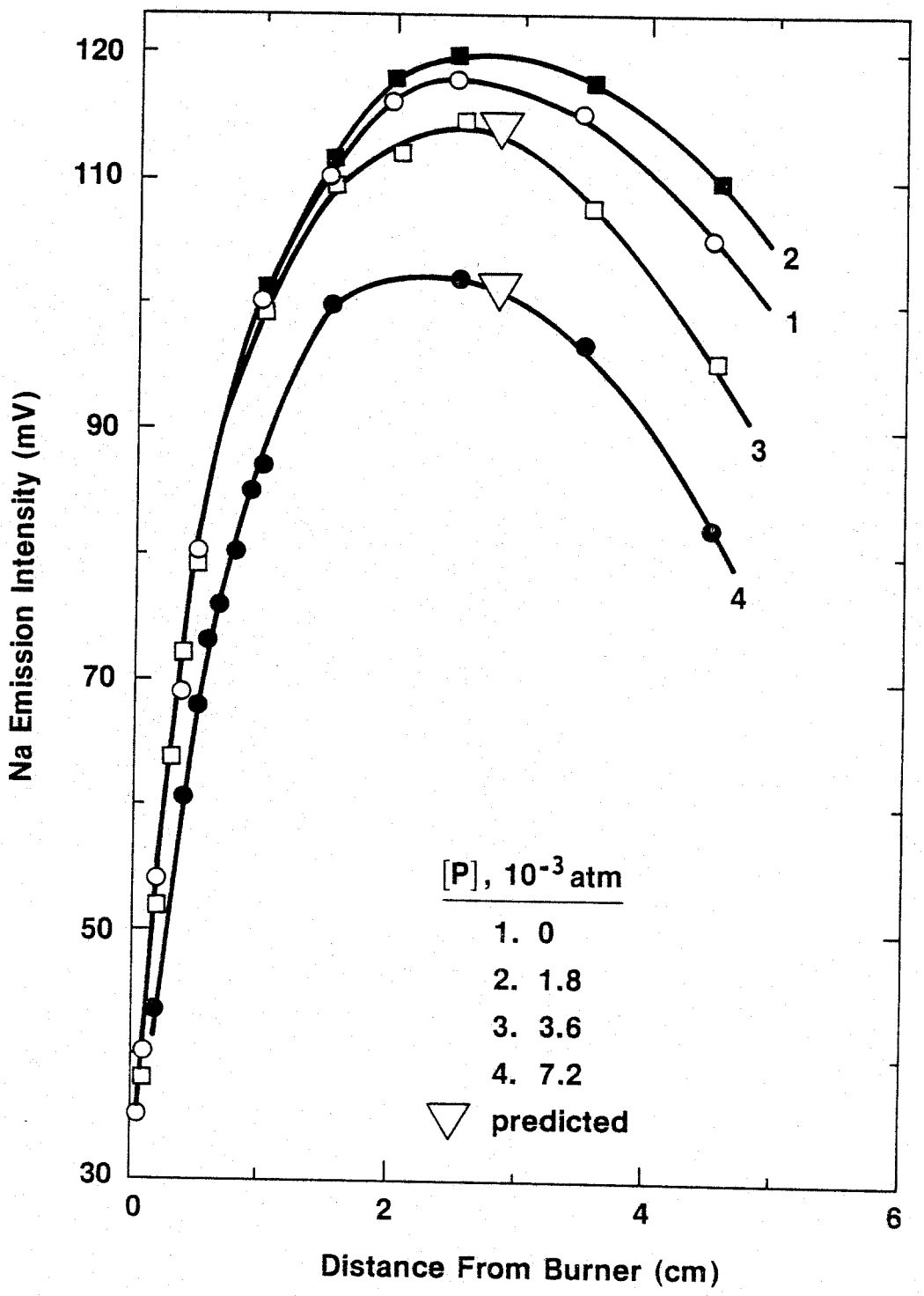
$H_2/O_2/N_2 = 3.7/1/2.1$
T(2 cm) ~ 2400 K
[Na] = 3.3×10^{-6} atm
Na Emission Intensity (mV)
120
110
90
70
50
30
0
2
4
6
Distance From Burner (cm)
1
2
3
4
[P], 10^{-3} atm
1. 0
2. 1.8
3. 3.6
4. 7.2
predicted

Figure D.1.

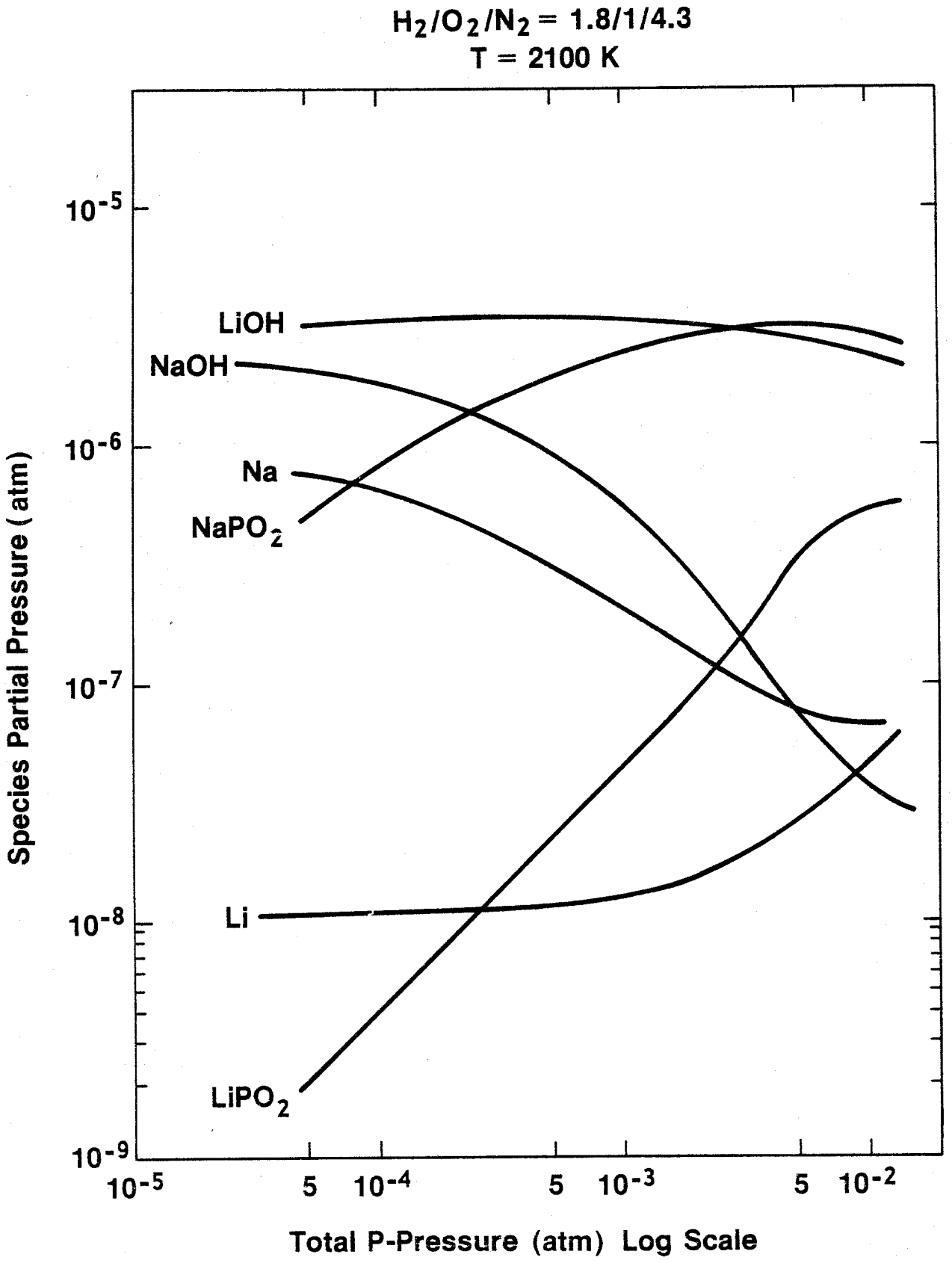
$H_2/O_2/N_2 = 1.8/1/4.3$
T = 2100 K
Species Partial Pressure (atm)
10^{-5}
10^{-6}
10^{-7}
10^{-8}
10^{-9}
LiOH
NaOH
Na
$NaPO_2$
Li
$LiPO_2$
10^{-5}
5 10^{-4}
5 10^{-3}
5 10^{-2}
Total P-Pressure (atm) Log Scale

Figure D.2.

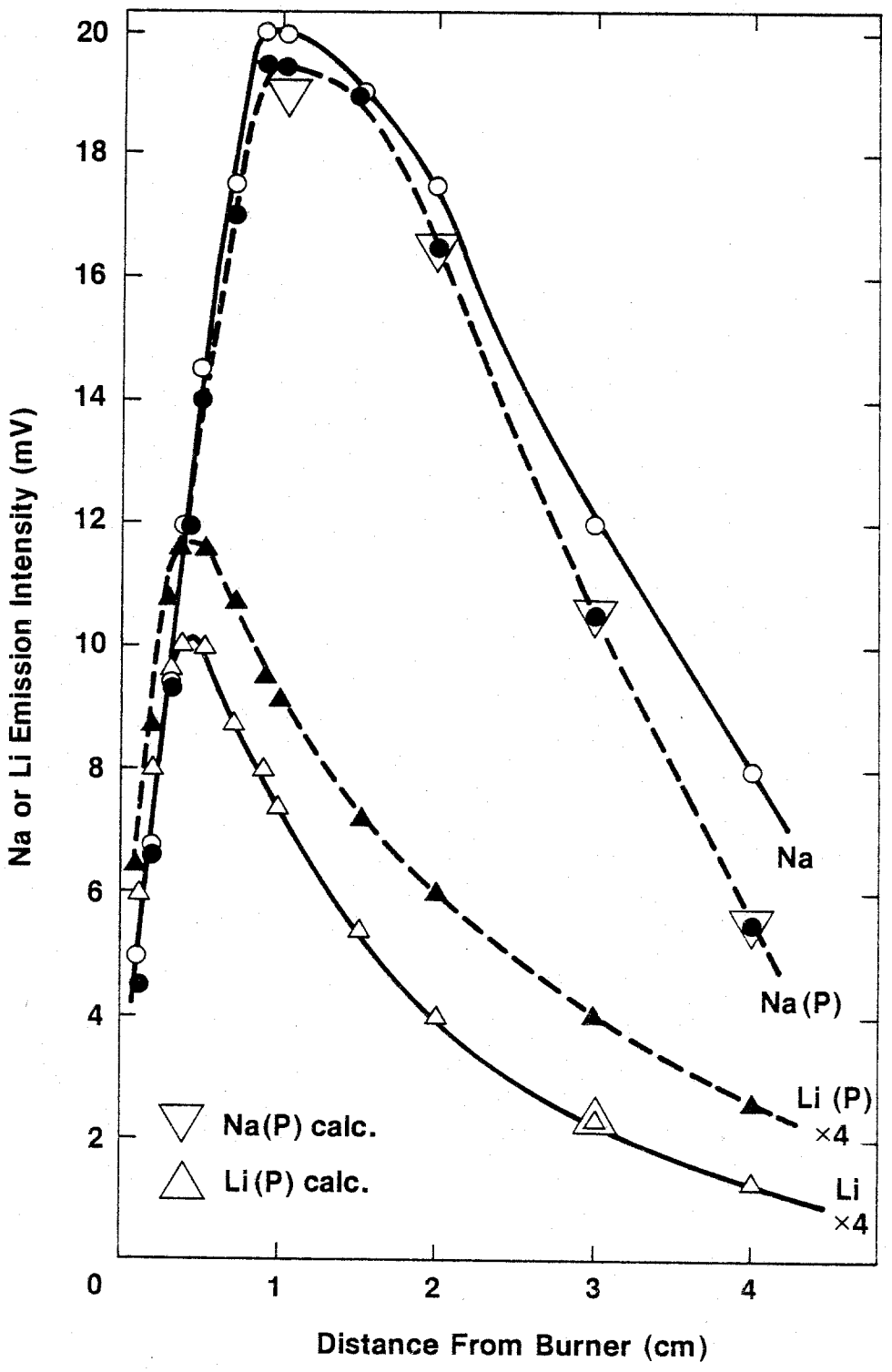
$H_2/O_2/N_2$ = 2/1/2
T(3 cm)~2450 K
[P] = 6×10-4 atm
[Na], [Li] = 4.8×10-6 atm
Na or Li Emission Intensity (mV)
Distance From Burner (cm)
Na
Na(P)
Li (P)
×4
Li
×4
Na(P) calc.
Li(P) calc.

Figure D.3.

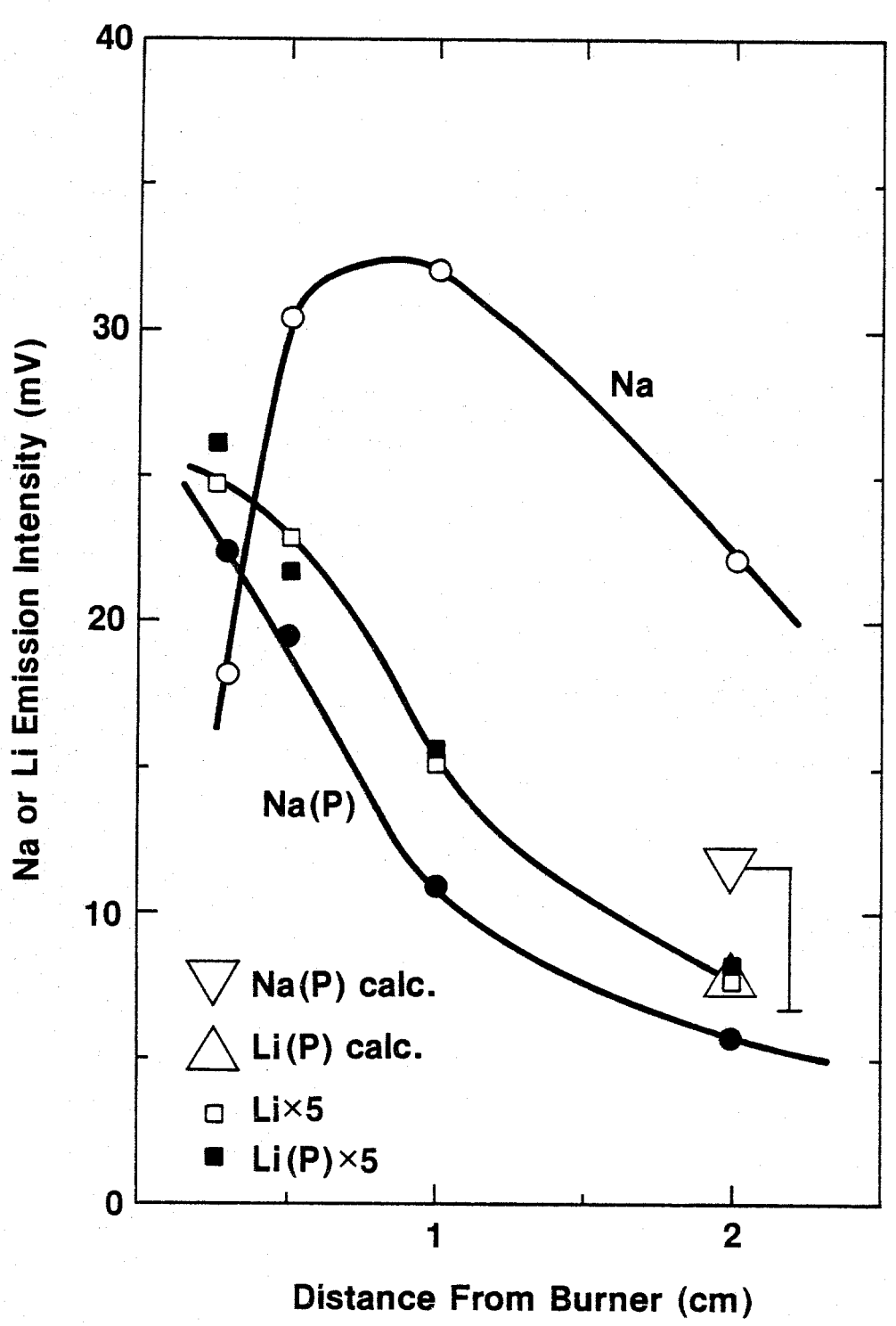
$H_2/O_2/N_2 = 2/1/2$
T(2 cm)~2450 K
[P]= 4.6×10⁻³ atm
[Na], [Li] = 4.8×10⁻⁶ atm
Na or Li Emission Intensity (mV)
Distance From Burner (cm)
Na
Na(P)
Na(P) calc.
Li(P) calc.
Li×5
Li(P)×5
0
10
20
30
40
1
2

Figure D.4.

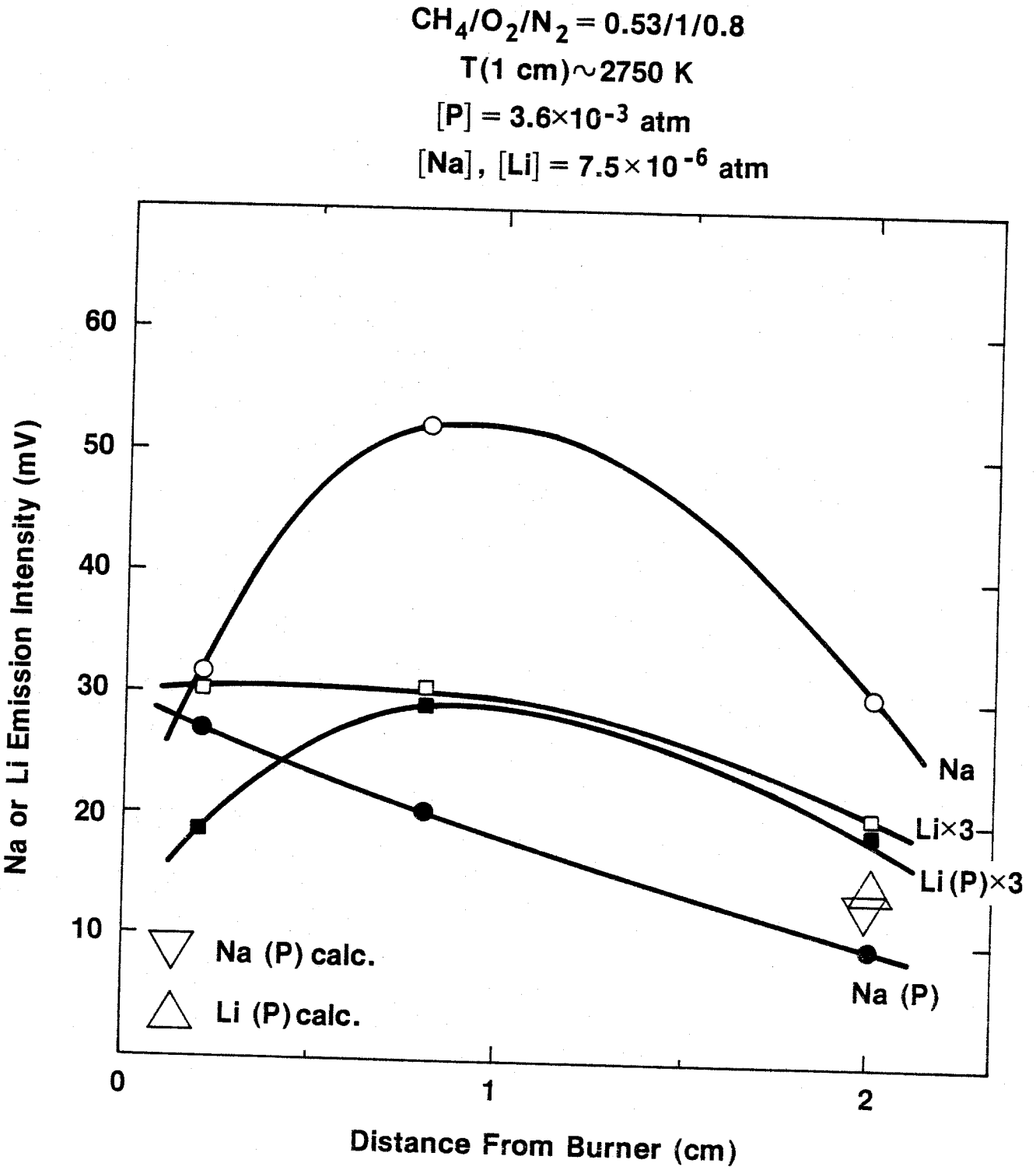
$CH_4/O_2/N_2 = 0.53/1/0.8$
T(1 cm)~2750 K
[P] = 3.6×10⁻³ atm
[Na], [Li] = 7.5×10⁻⁶ atm
Na or Li Emission Intensity (mV)
60
50
40
30
20
10
0
1
2
Distance From Burner (cm)
Na
Li×3
Li (P)×3
Na (P)
Na (P) calc.
Li (P) calc.

Figure D.5.

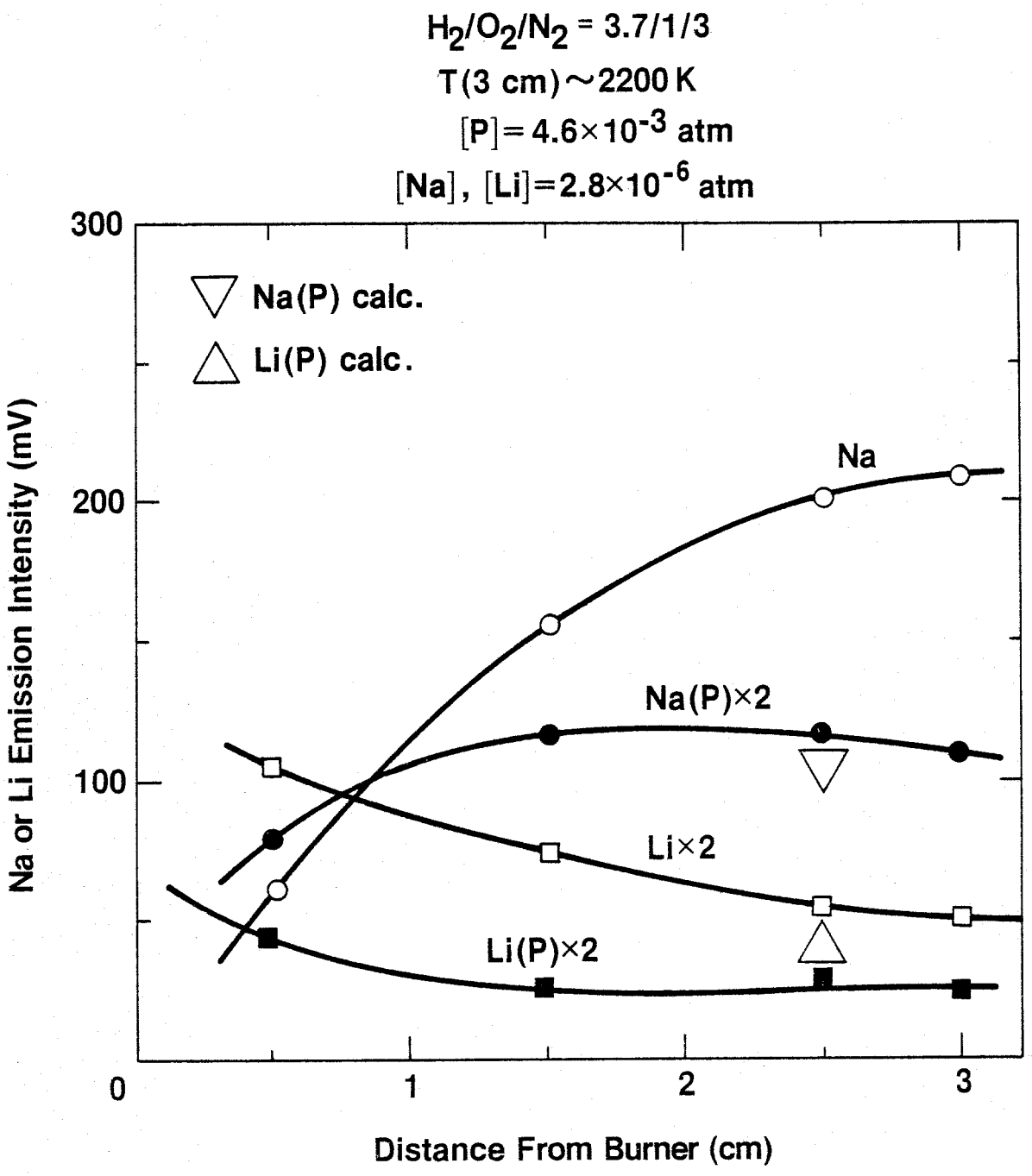
$H_2/O_2/N_2$ = 3.7/1/3
T(3 cm)~2200 K
[P]= 4.6×10^{-3} atm
[Na], [Li]=2.8×10^{-6} atm
Na(P) calc.
Li(P) calc.
Na
Na(P)×2
Li×2
Li(P)×2
Na or Li Emission Intensity (mV)
Distance From Burner (cm)
300
200
100
0
1
2
3

Figure D.6.

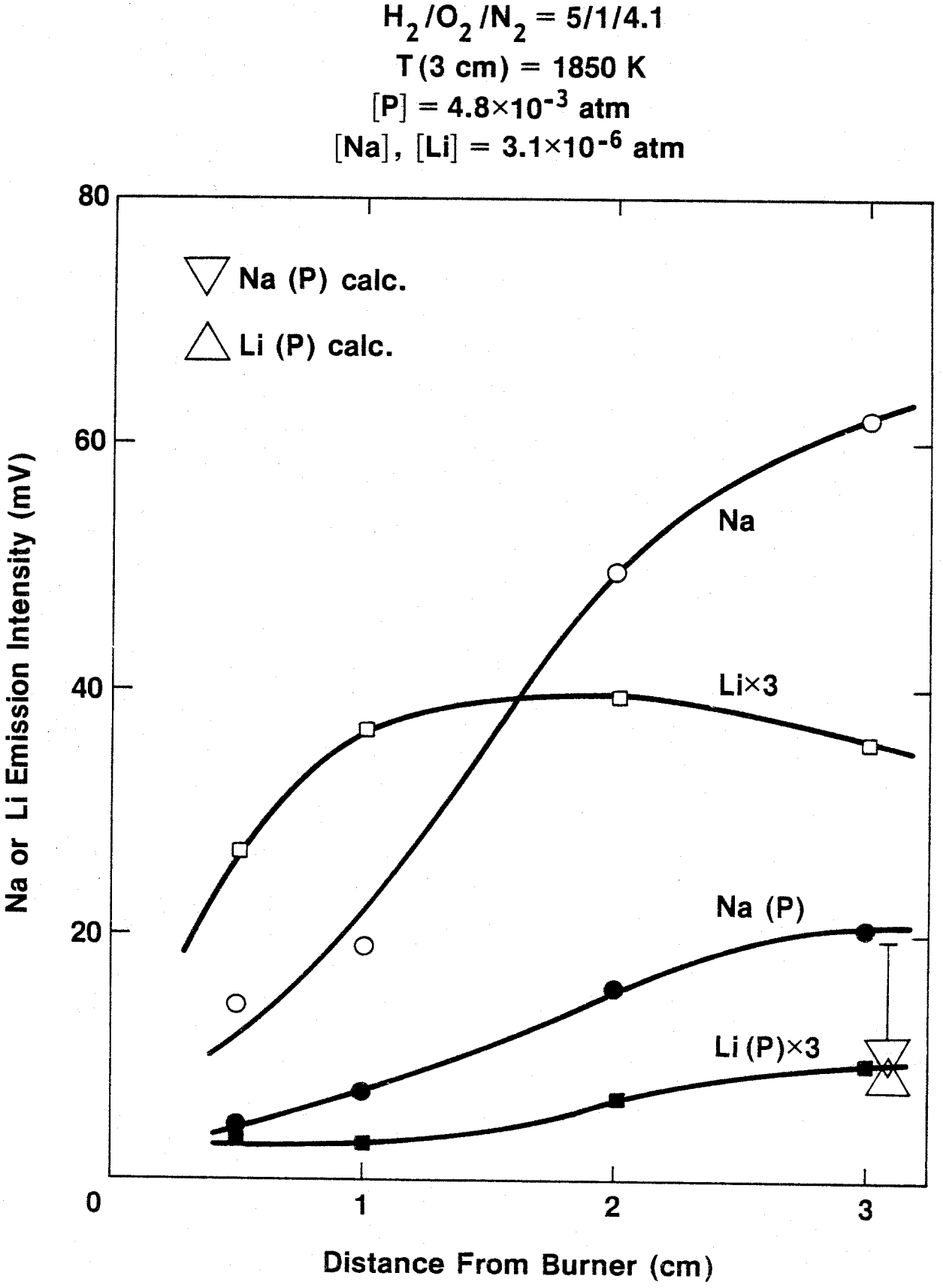
$H_2/O_2/N_2 = 5/1/4.1$
T (3 cm) = 1850 K
[P] = 4.8×10^{-3} atm
[Na], [Li] = 3.1×10^{-6} atm
Na (P) calc.
Li (P) calc.
Na
Li×3
Na (P)
Li (P)×3
Na or Li Emission Intensity (mV)
Distance From Burner (cm)
0
20
40
60
80
1
2
3

Figure D.7.

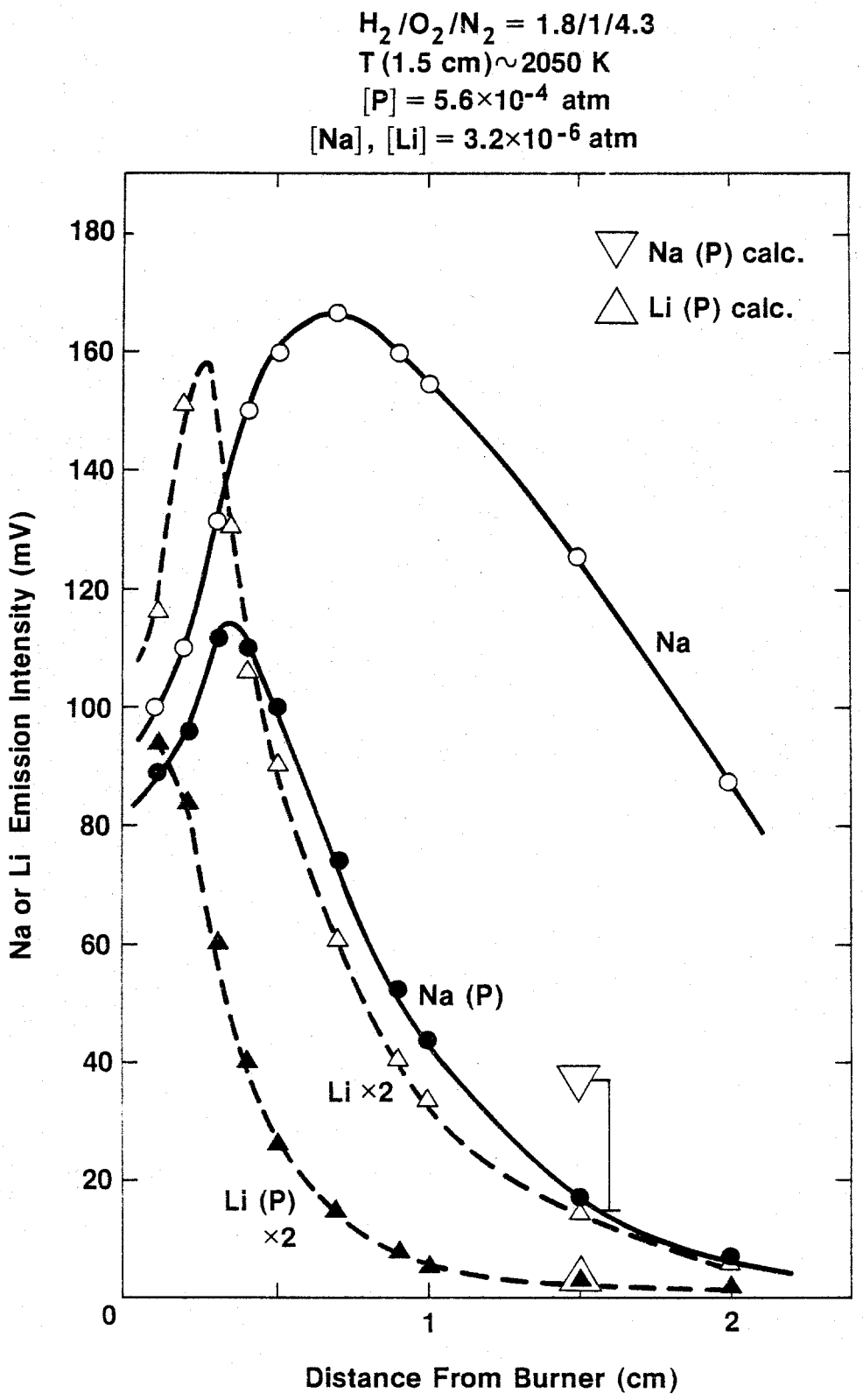
$H_2/O_2/N_2$ = 1.8/1/4.3
T (1.5 cm)~2050 K
[P] = 5.6×10^{-4} atm
[Na], [Li] = 3.2×10^{-6} atm
Na (P) calc.
Li (P) calc.
Na
Na (P)
Li ×2
Li (P)
×2
Na or Li Emission Intensity (mV)
Distance From Burner (cm)
0
20
40
60
80
100
120
140
160
180
1
2

Figure D.8.

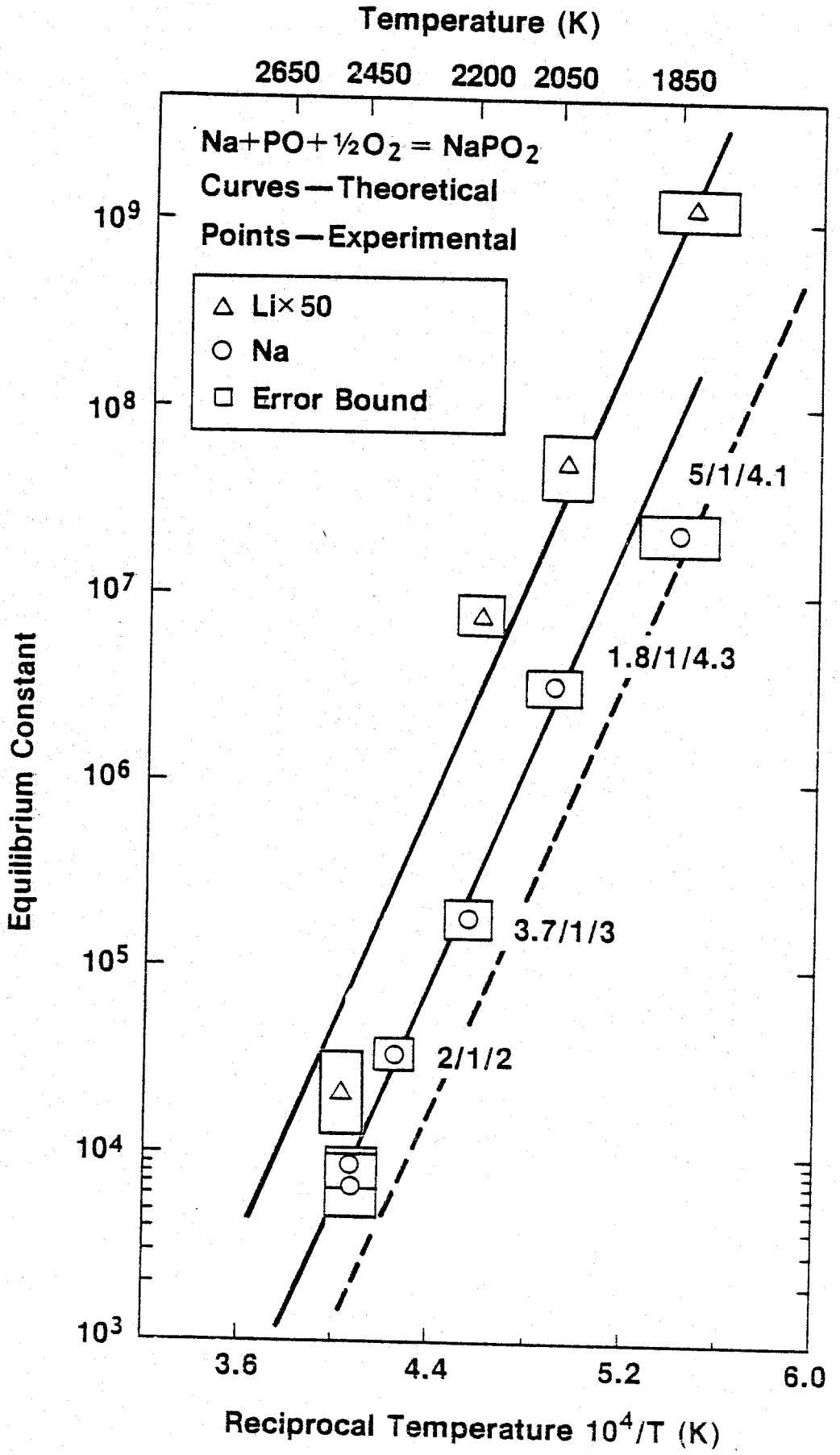
Temperature (K)
2650 2450 2200 2050 1850
Na+PO+½O2 = NaPO2
Curves—Theoretical
Points—Experimental
△ Li×50
○ Na
□ Error Bound
5/1/4.1
1.8/1/4.3
3.7/1/3
2/1/2
Equilibrium Constant
10^9
10^8
10^7
10^6
10^5
10^4
10^3
3.6
4.4
5.2
6.0
Reciprocal Temperature 10^4/T (K)

Figure D.9.

Appendix E

Selection of Thermodynamic Data Base for Multicomponent Equilibrium and Kinetic Calculations

J. W. Hastie and D. W. Bonnell

1. The Multicomponent Equilibrium Problem

The flame systems described in the body of this report contain more than 40 known significant species. Many equilibria, acting simultaneously, control the equilibrium concentration of an individual species and its contribution to the system enthalpy. Thus, the thermodynamic prediction of equilibrium composition and temperature requires computer solution of multicomponent equilibria. For these calculations, we have used the established Gordon and McBride (1971)[1] program (CEC-76), which is based on free energy minimization. The thermodynamic data base for this program closely follows the JANAF (1971) Thermochemical Tables. We have modified this data base for the present study, including new species and/or thermodynamic functions. To generate an appropriate species data base, we need enthalpies and entropies of formation, or related thermodynamic functions, at the temperatures of interest.

The parametrization of thermodynamic data used by the program CEC-76 is made as follows. Species are coded into the data base with sets of seven coefficients, A_1 to A_7 representing heat capacity, heat of formation at 298.15, and entropy at 298.15. The constant pressure heat capacity function, in dimensionless form Cp/R,[2] is represented by a five term polynomial:

---

[1]For reference citations, see Section 6 in the body of this report.

[2]For convenience, the superscript 0 has been omitted from all thermodynamic functions as all functions discussed are referenced to JANAF (1971) standard state conditions.

$$\frac{Cp}{R} = A_1 + A_2T + A_3T^2 + A_4T^3 + A_5T^4.$$

This polynomial is fit in a least square sense to a tabulation of Cp. The data base structure provides for two such five-term representations covering contiguous temperature intervals of a single phase, most commonly 300 to 1000 K and 1000 to 5000 K for gases. For condensed phases, only one set of coefficients is normally specified for each phase, and this is for the temperature range where the phase is stable. Application of the two-range coefficient scheme is useful in achieving, with a polynomial, the smooth behavior more normally associated with Shomate-type equations (containing a Cp term in T^{-2} and an H_T-H_{ref} term in T^{-1}).

With a multi-range coefficient scheme, it is necessary to constrain the fit to produce a common value at each juncture. For the data added in this study, (HPO, HPO_2, $NaPO_2$, and $LiPO_2$), assumptions in the estimation process made it unnecessary to adopt the two-range approach. A single set of coefficients, valid to function-accuracy over the temperature range 298.15 to 5000 K, was used.

In order to calculate a complete set of thermodynamic properties from heat capacity data, two other pieces of information must be known. These are, the entropy and enthalpy of formation at the reference temperature (298.15 K, abbreviated as 298) along with applicable transition heats.

The dimensionless entropy function can be expressed as:

$$\frac{S_T}{R} = \int_{298}^{T} \frac{Cp}{RT}\, dT + \frac{S_{298}}{R}\ .$$

From the polynomial form of Cp/R, one obtains:

$$\frac{S_T}{R} = A_1 \ln T + \sum_{i=2}^{5} \frac{A_i}{i-1} T^{i-1} + \left[-A_1 \ln(298.15) - \sum_{i=2}^{5} \frac{A_i}{i-1} (298.15)^{i-1} + \frac{S_{298}}{R} \right] .$$

The bracketted term is supplied as an "integration constant" (A_7). The value of A_7 for each range is adjusted to provide a common entropy at the crossover point between ranges. This means that, for the range encompassing the temperature 298.15 K (298)

$$A_7 = -A_1 \ln(298.15) - \sum_{i=1}^{5} \frac{A_i}{i-1} (298.15)^{i-1} + \frac{S_{298}}{R}$$

and for other ranges, at the adjoining temperature T*, the higher range coefficient is given by

$$A_7 = -A_1 \ln T^* - \sum_{i=1}^{5} \frac{A_i}{i-1} T^{*i-1} + \frac{S_{T^*}}{R} + \frac{\Delta S_{T^*}}{R} .$$

The term S_{T^*}/R, is calculated from the entropy expression for the lower adjoining range. The last term, $\Delta S_{T^*}/R$ is the phase transition entropy at T*, if the change in ranges is due to a phase change. For each range, the entropy function is

$$\frac{S_T}{R} = A_1 \ln T + A_2 T + \frac{A_3}{2} T^2 + \frac{A_4}{3} T^3 + \frac{A_5}{4} T^4 + A_7 .$$

In general, then, $S_{298.15}/R$ may not be back-calculated from a set of coefficients not encompassing the temperature 298.15 K in its valid range.

The enthalpy increment function is given by:

$$\frac{H_T - H_{298}}{R} = \int_{298}^{T} \frac{Cp}{R} \, dT$$

which, evaluated in terms of the Cp/R polynomial function yields,

$$\frac{H_T - H_{298.15}}{R} = \sum_{i=1}^{5} \frac{A_i}{i} T^i - \sum_{i=1}^{5} \frac{A_i}{i} (298)^i$$

The data base design includes the heat of formation at this point by arbitrarily assuming for convenience that

$$H_{298.15} \equiv \Delta H_{f,298} \ .$$

The coefficient A_6 for the range containing 298.15 K then becomes

$$A_6 = - \sum_{i=1}^{5} \frac{A_i}{i} (298.15)^i + \frac{\Delta H_{f,298}}{R}$$

This definition allows the data base to represent directly a characteristic "assigned enthalpy" by

$$\frac{H_T}{RT} = A_1 + \frac{A_2}{2}T + \frac{A_3}{3}T^2 + \frac{A_4}{4}T^3 + \frac{A_5}{5}T^4 + \frac{A_6}{T}$$

For temperature ranges above and not including 298.15, the "enthalpy coefficient", A_6, can be written

$$A_6 = \sum_{i=1}^{5} \frac{A_i}{i} (298.15)^i + \frac{H_{T*}}{R} + \frac{\Delta H_{T*}}{R} \ .$$

The term H_{T*}/R is evaluated from the lower contiguous range coefficients at the crossover temperature T*. The last term is the heat of transition at T*, in the case of a phase transition being the reason for a change in ranges and is zero where no transition occurs.

Gas phase additions to the data base are prepared from a statistical mechanical calculation of the thermodynamic properties of the ideal gas state. The pertinent equations, as given by JANAF (1971) have been implemented as both BASIC and FORTRAN programs in transportable form. The functions added for this report were calculated by the BASIC version, run on the CDC Cybernet computer system in 14-digit precision arithmetic.

The equilibrium calculations were made using the program CEC-76 supplied to us by B. McBride of NASA Lewis from a tape created December 11, 1979. This program was used without modification other than transportability corrections. All runs were made in a demand environment on the NBS 1108I system Univac 1108, using the Ver 33R3A EXEC 8 system with the program compiled and run under the FORTRAN system.

Table E.1 lists the coefficients used to develop the present data base. The corresponding formation enthalpy and entropy functions, from which these coefficients were derived, are summarized in the following sections.

Table E.1

Coefficients for Thermodynamic Function Representation[a]

Molecule	A_1	A_2	A_3	A_4	A_5	A_6	A_7
HPO	2.87129590 E+00	5.74074470 E-03[b]	-3.44113690 E-06	9.71911380 E-10	-1.05193950 E-13	-5.86337172 E+03	1.04228407 E+01
HPO_2	2.52212083 E+00	8.91362860 E-03	-4.66432070 E-06	1.15362175 E-09	-1.08937615 E-13	-4.94190805 E+04	1.49576310 E+01
$NaPO_2$	5.71069827 E+00	7.66608854 E-03	-5.06885111 E-06	1.42209111 E-09	-1.42316725 E-13	-6.42003450 E+04	2.3386362 E+00
$LiPO_2$	4.87775884 E+00	8.97034507 E-03	-5.85790189 E-06	1.63025247 E-09	-1.62250410 E-13	-5.96756424 E+04	3.14581376 E+00

[a]Valid for temperature range 298.15 - 5000 K.

[b]Exponent computer terminology, e.g., E-03 = 10^{-3}.

2. Thermodynamic Functions for LiOH and NaOH

JANAF (1971) lists LiOH thermodynamic functions dated 1966. A more recent set of data (June, 1971) have been included in the present data base. The difference between the two data sets is significant. When the earlier functions were used, considerable discrepancy between measured and calculated H-atom equilibrium partial pressures was found. Likewise, the original JANAF (1971) listing for NaOH (dated March 31, 1966) has been updated by JANAF (dated December 1970) and this latest data set was used in the present study.

3. Thermodynamic Functions for PO

PO is usually a prevalent species in high temperature P-containing systems. Consequently, thermodynamic measurements of other P-containing species are frequently referenced to PO. In the present study, the formation-enthalpies ($\Delta H_{f,298}$) for HPO_2, $NaPO_2$, and $LiPO_2$ were measured relative to PO. It was found that the best fit to numerous sets of experimental data, involving PO, HPO_2, $NaPO_2$ and $LiPO_2$, was obtained when the PO formation-enthalpy was decreased (in the direction of greater stability) by several kcal/mol relative to the literature data. Therefore, in order to maintain internal thermodynamic consistency, we have selected this lower (more negative) formation-enthalpy for use in the multicomponent equilibrium data base. This value is still within experimental error of the several alternative literature values, summarized as follows:

$\Delta H_{f,298}$PO kcal/mol	Reference
-5.5 ± 2	Present study
-2.3 ± 2	Drowart, et al., (1972)
-1.5 ± 2	JANAF (1971), Interim Table

The relatively accurate statistical thermodynamic functions of entropy, and heat capacity were used as given by JANAF (1971).

4. Thermodynamic Functions for PO_2

JANAF (1971) lists an interim table (dated 1962) of estimated thermodynamic functions for PO_2. With these functions, the PO_2 partial pressure in our flames is calculated to be one to two orders of magnitude greater than the possible upper limit value indicated from mass spectrometric analysis (e.g., see table 2 in the body of this report). Since the JANAF (1971) estimates were made, Drowart et al., (1972) and Smoes and Drowart (1974) have obtained an apparently reliable value for the formation-enthalpy using the established Knudsen effusion mass spectrometric technique. We have adopted their value for the present data base, namely:

$$\Delta H_{f,298}(PO_2) = -61.0 \pm 2.6 \text{ kcal/mol} \quad .$$

No significant errors are expected in the statistical calculation of the other thermodynamic functions using estimated structural and spectroscopic parameters and the JANAF (1971) values have been retained in the data base.

5. Thermodynamic Functions for PN

PN is a relatively stable molecule and, under some flame conditions, based on JANAF (1971) thermodynamic functions, can act as a significant phosphorous sink. For the hottest flame where PN mass spectrometric observations were made, (see table 2 in the body of this report), the observed PN partial pressure approached the predicted equilibrium value within the combined experimental and thermodynamic uncertainty. Therefore, we have used the JANAF (1971) functions, as given, even though several more recent (but disparate) experimental values for $\Delta H_{f,298}$PN have appeared in the literature.

6. Thermodynamic Functions for HPO (POH)

From its intense emission in the green, HPO is a well known spectroscopic flame species. Thermodynamically, however, the geometrical isomer P-OH will be much more stable. We have estimated the formation-enthalpy for this new species using the M-OH versus M-F bond energy correlation method (Hastie, 1975 p. 291), which yields,

$$\Delta H_{f,298}(HPO) = -9.5 \pm 5 \text{ kcal/mol} \quad .$$

Entropy and related functions have been calculated statistically using estimated structural and spectroscopic parameters, as summarized in table E.3.

7. Thermodynamic Functions for HPO_2 (HOPO)

Formation-enthalpy data for HPO_2 have been summarized in Appendix D where,

$$\Delta H_{f,298}HPO_2 = -96 \pm 4 \text{ kcal/mol} \quad ,$$

was selected as the best value.

Entropy and related functions were calculated, statistically, using structural and spectroscopic estimates based on those used by JANAF (1971) for the analogous species HBO_2, as summarized in table E.3.

8. Thermodynamic Functions for $NaPO_2$ and $LiPO_2$

Indirect evidence was presented in Appendix D for the probable formation of $NaPO_2$ and $LiPO_2$ in the experimental flame systems. From these data, the following formation enthalpies were indicated:

$$\Delta H_{f,298}NaPO_2 = -123.6 \pm 3.5 \text{ kcal/mol}$$

$$\Delta H_{f,298}LiPO_2 = -115.0 \pm 5.8 \text{ kcal/mol} \quad .$$

These results were used for the multicomponent equilibrium data base.

Entropy and related functions were calculated statistically using the parameters given in table E.3.

9. Comparison Between Phosphorus and Boron-Based Systems

The species BO_2, HBO_2, $NaBO_2$, and $LiBO_2$ are known to form in flames, and their thermodynamic functions are relatively well established (JANAF, 1971). These species should be reasonably analogous to the corresponding P-containing species, and we can expect the relative bond dissociation energies and entropies to be similar for both series. Hence,

$$\frac{D_{O\text{-}PO}}{D_{O\text{-}BO}} \simeq \frac{D_{HO\text{-}PO}}{D_{HO\text{-}BO}} \simeq \frac{D_{Na\text{-}PO_2}}{D_{Na\text{-}BO_2}} \simeq \frac{D_{Li\text{-}PO_2}}{D_{Li\text{-}BO_2}}$$

where, for example, $D_{O\text{-}PO}$ corresponds to the energy for the process,

$$PO_2 = O + PO.$$

In the majority of cases, analogies of this kind usually yield predicted bond dissociation energies to within 10 percent uncertainty for high temperature species. Similar analogies can be made for entropies. A comparison of our experimental and derived data with values predicted by analogy with the boron system is given in table E.2. The thermodynamic data for PO_2 and BO_2 were used as reference points. As shown in the table, there is an excellent agreement between the experimental/calculated data and that predicted by the boron analogy.

Table E.2

Comparison of Experimental and Calculated Thermodynamic Data With Boron Analogy Predictions[a]

	Present Study	Boron Analogy	% Difference
D_{HO-PO}[b]	99.9 ± 4	103.1	-3.6
D_{Na-PO_2}	88.3 ± 5.5[g]	82.9 ± 3.0[e] or 85.0 ± 5.0[d]	6.5 or 3.3
D_{Li-PO_2}	92.4 ± 5.8	92.7	-0.3
S_{HPO_2}[c]	63.2 ± 2.0	63.2	0
S_{NaPO_2}	73.4 ± 2.0[f]	71.6	2.5
S_{LiPO_2}	66.3 ± 2.0[f]	68.0	-2.5

[a]Data at reference temperature of 298.15 K.

[b]Represents energy (kcal/mol) for process, $HPO_2 = OH + PO$, and similarly for the other species.

[c]Units of cal/deg mol.

[d]Based on data of Jensen for $LiBO_2$ and $NaBO_2$; Jensen, D. E., (1969), Trans. Faraday Soc., 65, 2123.

[e]JANAF (1971) data based on a single indirect measurement.

[f]Data consistent with Second Law experimental data for, $Na + PO + 1/2O_2 = NaPO_2$, and similarly for Li.

[g]Two disparate literature values, based on Knudsen effusion mass spectrometry, are available; namely, 82.3 and 72.9 kcal/mol as obtained by Gingerich and Miller (1975) and Smoes and Drowart (1974), respectively.

10. Data Summary for New P-Containing Species

The statistical mechanical and formation-enthalpy data used in developing the thermodynamic data base are summarized in table E.3.

Table E.3

Summary of Statistical Mechanical and Thermodynamic Data[a]

Molecule	Structure (units ° and Å)	$I_A \cdot I_B \cdot I_C$ 10^{-115} gm^3 cm^3	ω cm^{-1}	$S_{298.15}$ cal/deg mol	$\Delta H_{f,298.15}$ kcal/mol
POH	∢HOP = 118.0 γHO = 1.0 γPO = 1.6	0.0284	2400(ν_3) 950(ν_1) 500(ν_2)	56.3	-9.5[c]
HOPO	∢HOP = 118.0 ∢OPO = 116.0 γPO = 1.40 γOH = 1.00	1.516	3680(ν_1) 2030(ν_2) 1420(ν_3) 1195(ν_4) 530(ν_5) 1400(ν_6)	63.2	-96.0
Li-OPO[e]	∢Li-OP = 100.0 ∢OPO = 116.0 γOP = 1.6 γLi-O = 1.62	6.7	850(ν_2) 1250(ν_1) 550(ν_4) 925(ν_3) 250(ν_6) 325(ν_5)	66.3	-115.0
Na-OPO[e]	∢NaOP = 100.0 ∢OPO = 116.0 γOP = 1.60 γO-Na = 2.00	30.50	800(ν_1) 1200(ν_2) 500(ν_3) 200(ν_4) 100(ν_5) 150(ν_6)	73.4	-123.5

[a] Harmonic oscillator approximation and σ = 1, ε = 0, g = 1 for each species.

[b] Entropy for HPO isomer similar to POH.

[c] Refers to P-OH isomer.

[d] ∢ -angle; γ bond distance.

[e] Structure assumed analogous to HOPO but a M-O-P-O ring structure is also reasonable. This structural uncertainty should not affect entropies by more than several cal/deg mol.

11. Summary of Thermodynamic Functions Used in Kinetic Analysis

When considering reversible kinetic processes, the ratios of forward to reverse preexponential and exponential terms of an Arrhenius rate constant expression are constrained to equal the reaction entropy (ΔS_T) and enthalpy (ΔH_T) terms respectively. This arises from the equality,

$$K = k_f/k_r \quad ,$$

where K is the equilibrium constant and k_f, k_r are the forward and reverse rate constants, respectively. It is, therefore, useful, in deriving rate constant expressions, to have available expressions for K in a similar form, i.e.:

$$K = \exp \frac{\Delta S_T}{R} \exp \frac{-\Delta H_T}{RT} \quad ,$$

with ΔS_T and ΔH_T defined at thr median temperature of interest ($\sim$ 2000 K for the present study). Values of S_{2000} and $\Delta H_{f,2000}$ for the kinetically significant species in P-based flame inhibition/promotion are summarized in table E.4.

Table E.4

Summary of Thermodynamic Functions Used in Kinetic Analysis[a]

Species	$\Delta H_{f,2000}$ kcal/mol	S_{2000} cal/deg mol
PO	-26.8	69.0
PO_2	-81.9	84.2
HPO	-10.2	77.5
HPO_2	-97.9	90.0
H	54.2	36.8
OH	8.9	57.9
H_2	0.	45.0
H_2O	-60.1	63.2

[a]Data from JANAF (1971), unless indicated otherwise in the main text.

NBS-114A (REV. 2-8C)

U.S. DEPT. OF COMM. BIBLIOGRAPHIC DATA SHEET (See instructions)	1. PUBLICATION OR REPORT NO. NBSIR 80-2169	2. Performing Organ. Report No.	3. Publication Date December 1980

4. TITLE AND SUBTITLE

MOLECULAR CHEMISTRY OF INHIBITED COMBUSTION SYSTEMS

5. AUTHOR(S)

J. W. Hastie and D. W. Bonnell

6. PERFORMING ORGANIZATION (If joint or other than NBS, see instructions)

NATIONAL BUREAU OF STANDARDS
DEPARTMENT OF COMMERCE
WASHINGTON, D.C. 20234

7. Contract/Grant No.

IL 161102 BH 57-08

8. Type of Report & Period Covered

Final 5/77-5/79

9. SPONSORING ORGANIZATION NAME AND COMPLETE ADDRESS (Street, City, State, ZIP)

U.S. Army Research Office
Research Triangle Park, NC 27709

10. SUPPLEMENTARY NOTES

☐ Document describes a computer program; SF-185, FIPS Software Summary, is attached.

11. ABSTRACT (A 200-word or less factual summary of most significant information. If document includes a significant bibliography or literature survey, mention it here)

Virtually nothing is known about the high temperature chemistry of phosphorus in a flame environment. Phosphorus compounds are known flame retardants though the mechanistic evidence is empirically based. In the present study, high pressure sampling mass spectrometry and optical spectroscopic methods have been applied to the molecular characterization of P-containing flames. The key process controlling flame inhibition and enhancement is identified as:

$$HPO_2 + H \rightleftarrows H_2O + PO$$

New thermodynamic data are presented for $NaPO_2$ and $LiPO_2$ which are present in Li/Na-containing flames.

12. KEY WORDS (Six to twelve entries; alphabetical order; capitalize only proper names; and separate key words by semicolons)

Flame inhibition; H-atoms; kinetics; mass spectrometry; phosphorus; radicals; Raman spectroscopy; temperature

13. AVAILABILITY

☒ Unlimited

☐ For Official Distribution. Do Not Release to NTIS

☐ Order From Superintendent of Documents, U.S. Government Printing Office, Washington, D.C. 20402.

☒ Order From National Technical Information Service (NTIS), Springfield, VA. 22161

14. NO. OF PRINTED PAGES

173

15. Price

$11.00

USCOMM-DC 6043-P80